Atomic Scale Study of Thermal Properties using STEM/EELS and First-Principles Calculations

by

Xuan Hu
B.A. (Wuhan University) 2010
M.S. (Wuhan University) 2012

Thesis submitted in partial fulfillment of the requirements
for the degree of Doctor of Philosophy in Physics
in the Graduate College of the
University of Illinois at Chicago, 2019

Chicago, Illinois

Defense Committee:
Robert F. Klie, Chair and Advisor
Serdar Öğüt, Advisor
Hyowon Park
Alan W. Nicolls, RRC
Amin Salehi-Khojin, Mechanical Engineering Department

This thesis is dedicated to my parents and my wife for their constant support and love.

ACKNOWLEDGMENTS

I would like to thank my advisors Dr. Robert Klie and Dr. Serdar Öğüt from University of Illinois at Chicago. I would like to thank Dr. Robert Klie for his supervision and patience on my experimental studies. His insight and expertise in science have presented me how beautiful the microscopic world looks like and how far the current cutting-edge technology could reach. I would like to thank Dr. Serdar Öğüt for his supervision and support of my theoretical studies. His solid knowledge and strict discipline in research have taught me how a scientist could be and should be. I feel fortunate and greatly honored to have this journey in physics with these two great scientists. Also, I would like to thank my committee members for their expertise and suggestions: Dr. Hyowon Park, Dr. Alan W. Nicolls, Dr. Amin Salehi-Khojin.

I would like to thank the RRC group, including Dr. Alan W. Nicolls and Dr. Fengyuan Shi, for teaching me how to use the instruments of RRC and for their patient support to my experiments. Also, I would like to thank everyone in the experimental and theoretical groups: Liang Hong and Bin Shi, thank you for all the discussions on both experiments and simulations, and inspiring ideas on understanding physics; Arijita Mukherjee and Jacob R. Jokisaari, thank you for the great efforts on our collaborations for the development of new techniques; Xue Rui, Jinglong Guo, Canhui Wang, Patrick J. Phillips, Ahmet Gulec, and Tadas Paulauskas, thank you for your valuable suggestions and help on my research.

ACKNOWLEDGMENTS (Continued)

On a personal note, I would like to thank my family for their support and love. Especially I would like to thank my wife, Bowen Wei, for her understanding, patience and caring, which make my life joyful and hopeful in this journey. I would also like to thank my daughter, Grace Hu, for being in our life.

CONTRIBUTIONS OF AUTHORS

Chapter 1 reviews the current nanoscale thermal characterization methods and highlights the importance of nanoscale thermal characterization in materials research. Chapter 2 describes the background of the experimental techniques, while Chapter 3 describes the theoretical background of the simulation techniques. Chapter 4 includes a published paper (1) in which I was the primary author. Robert F. Klie and Patrick J. Phillips assisted me in the experiments shown in Figures 16, 19, 21, and 24. Serdar Öğüt assisted me in the calculations shown in Figures 17, 18, 20, 22, and 23. My advisor, Robert F. Klie and Serdar Öğüt contributed to the manuscript before submission. Chapter 5 includes a published paper (2) in which I was the primary author. Amin Salehi-Khojin and Poya Yasaei synthesized materials and prepared samples. Robert F. Klie and Jacob Jokisaari assisted in the experiments and data analyses shown in Figures 25, 26, 27, 30, and 31. Serdar Öğüt assisted in the calculations shown in Figures 28, 29, 30 and 31. All of the authors contributed to the manuscript before submission. Chapter 6 represents my own unpublished experiments to further explore alloy effects on the thermal expansion coefficients of two dimensional materials. After graduation, I anticipate that this part of research will be continued and published as part of a coauthored manuscript. Chapter 7 represents the conclusions of this thesis and future outlook in this field.

TABLE OF CONTENTS

TABLE OF CONTENTS (Continued)

LIST OF TABLES

LIST OF FIGURES

LIST OF FIGURES (Continued)

LIST OF FIGURES (Continued)

FIGURE **PAGE**

LIST OF FIGURES (Continued)

LIST OF ABBREVIATIONS

2D	Two-Dimensional
ABF	Annular Bright Field
CCO	$Ca_3Co_4O_9$
DFT	Density Functional Theory
DOS	Density of States
EDS	Energy-Dispersive X-ray Spectroscopy
EEGS	Electron Energy-Gain Spectroscopy
EELS	Electron Energy-Loss Spectroscopy
ELNES	Electron Loss Near Edge Structure
EXELFS	Extended Electron Energy Loss Fine Structure
FEG	Field Emission Gun
FET	Field-Effect Transistor
FWHM	Full-Width at Half Maximum
GGA	Generalized Gradient Approximation
HAADF	High Angle Annular Dark Field
HEG	Homogeneous Electron Gas
HWHM	Half-Width at Half Maximum

LIST OF ABBREVIATIONS (Continued)

IPA	Isopropyl Alcohol
LAADF	Low Angle Annular Dark Field
NMP	N-Methyl-2-Pyrrolidone
PAW	Projector Augmented Wave Potential
PBE	Perdew-Burke-Ernzerhof Functional
PLD	Pulsed-Laser Deposition
PW91	Perdew-Wang Functional
RPA	Random-Phase Approximation
RRC	Research Resources Center
RS	Rock Salt
SCF	Self-Consistent Field
SEM	Scanning Electron Microscopy
SQS	Special Quasirandom Structure
STEM	Scanning Transmission Electron Microscopy
TE	Thermoelectric
TEC	Thermal Expansion Coefficient
TEM	Transmission Electron Microscopy
TMD	Transition Metal Dichalcogenide

LIST OF ABBREVIATIONS (Continued)

ZLP	Zero Loss Peak
UIC	University of Illinois at Chicago
VASP	Vienna Ab Initio Simulation Package (VASP)

SUMMARY

As predicted by Moores Law, the density of transistors has doubled every two years which has contributed to the miniaturization of electronic devices. While the miniaturization offers remarkable improvements in electrical performance, heat dissipation and thermal expansion mismatch can be the problems in designing electronic devices. Therefore, the nanoscale thermal properties are an important subject of current research in electronic devices, and, correspondingly, thermal characterization methods are needed at nanometer scale. In this thesis, I have developed two types of nanoscale thermal characterization methods using the scanning transmission electron microscopy (STEM), electron energy loss spectroscopy (EELS) and first-principles calculations, and studied the thermal properties of different innovative materials to explore the superiorities and limitations of both methods.

In Chapter 4, I utilized an indirect characterization method to explore the Ti dopant effects on the thermoelectric properties of the layered structural materials, $Ca_3Co_4O_9$. Specifically, I examined the Seebeck coefficients of Ti-doped CCO and found limited influence from dopants on the thermoelectric properties. Then, I explored the Ti dopant effects on the crystal structure and electronic structure of CCO using atomic resolution imaging and spectroscopy (STEM/EELS) techniques. I found that the Ti dopants were mainly located in the RS subsystem, which performed a charge-carrier reservoir but did not contribute to the enhancement of the Seebeck coefficients. I found that Co ions remained the same valence state and spin state after Ti doping which would not influence the Seebeck coefficients. This study also suggests a

higher doping concentration may influence the Seebeck coefficients. Using this indirect method, one can study the relation between thermal properties and electronic properties and explain the macroscale thermal phenomenon. However, a direct observation of this relation is missing and needed for fundamental researches.

In Chapter 5, I demonstrated a direct approach to observe the nanoscale temperature and thermal expansion properties of 2D materials (graphene and transition metal dichalcogenides (TMD)). Specifically, I explored the temperature dependent plasmon energy shift phenomenon which could be monitored by the low-loss EELS signals and utilized to predict the local temperature with the atomic resolution STEM images. Combining these experimental results with the EELS simulation performed by the first-principles calculations, the thermal expansion coefficients of different two-dimensional materials (graphene, MoS_2, $MoSe_2$, WS_2, WSe_2) in different thickness were determined. The thermal expansion coefficients of monolayer two-dimensional materials are almost one order of magnitude larger than the ones from bulk. This may cause a severe thermal expansion mismatch problem in the design of electronic devices.

In Chapter 6, I utilized the nanoscale thermal expansion measurement technique on the TMD alloys ($Mo_{1-x}W_xS_2$) to explore the defects effects on the monolayer materials and the potential possibility to control the thermal expansion behavior of materials. With the same thermal expansion measurement methods performed for pure TMDs, the thermal expansion coefficients of the TMD alloys in different alloying concentrations were determined. When the materials gradually change from the pure materials (MoS_2 or WS_2) to the equally alloyed materials ($Mo_{0.5}W_{0.5}S_2$), the thermal expansion coefficients are reduced due to the interference from

the additional substitutional atoms on the lattice expansion. This control of thermal expansion coefficients presents a great potential to ease the thermal expansion mismatch problem in the electronic devices. It also suggests that the thermal expansion of the interface between two different materials may be not a linear transition from one to another one which is of great interest in both fundamental research and future applications.

CHAPTER 1

INTRODUCTION

At the absolute zero temperature, particles, such as atoms or ions in a crystal lattice of materials will remain static at their equilibrium positions. At a nonzero temperature, the atoms or ions will randomly vibrate around their equilibrium positions. Thermal properties of materials describe the statistical behavior of atoms or ions due to these thermal-induced vibrations.

The thermal properties of a material determine how it responds to temperature changes. When a solid is exposed to a system with an elevated temperature, the atomic vibrations between two systems will tend to reach a thermal equilibrium through energy transfer (called heat). The ability of the heat to be absorbed is called the heat capacity, while the mobility of the heat to flow is called the thermal conductivity. After absorbing the heat, the increased internal energy (microscopic kinetic energy from the random atomic vibrations) will increase the maximum amplitude of the atomic vibrations. Due to the asymmetry of the potential energy curve around the equilibrium state, the average inter-atomic distance will be changed (usually increased). This phenomenon is called the thermal expansion and is described by the thermal expansion coefficient of materials. In addition to these properties, the thermoelectric effect governs the response of a material to a temperature gradient. The gradient will result in the redistribution of the charge carriers from the high-temperature area to the low-temperature

area, and to the creation of a potential difference between two sides. The Seebeck coefficient, S, is given by $\frac{\Delta V}{\Delta T}$.

As discussed above, the thermal properties of materials influence structural and electronic properties, thus affecting the functional performance of materials and the design of devices. Some thermal properties, such as the Seebeck coefficient, can directly determine the performance of the devices by converting the temperature gradient into electric voltage. Understanding the thermal properties of materials is an important area of material science. Especially at the nanoscale, thermal properties play a critical role in research studies and technology applications. For instance, the nanoscale study of thermal boundary conductivity across the interfaces can reveal the heat transfer mechanism and guide the selection of materials for different devices. In particular, heat transfer becomes important in low-dimensional materials. When the spatial dimension approaches the nanometer scale, comparable to size of Bohr radius, materials will exhibit properties different than those in bulk. This is called the quantum confinement effect. Low-dimensional materials, such as the quantum dots and 2-dim materials, attract a lot of attention due to their outstanding electronic and thermal properties. The nanoscale study of thermal properties becomes particularly critical in understanding the quantum confinement effects and the behavior of low-dimensional materials. A nanoscale study of 2-dim materials focusing on the thermal expansion behavior can guide the design of next-generation nano-devices (2). However, for the studies in nanoscale characterization techniques of temperature and thermal properties are needed.

Nanoscale characterizations of thermal properties can be divided into two approaches: 1), indirect characterization of structural or electronic responses due to the variation of thermal properties, or 2), direct characterizations of thermal properties at corresponding temperatures.

Using the first approach, the relation between thermal and electronic properties can be studied. Nanoscale characterization of certain thermal properties is challenged. Instead, one can utilize the nanoscale techniques (such as the electron microscope) to explore the structural and electronic properties of materials to reveal the thermal properties. The thermal phenomena can then be analyzed from the view of microscopic particles, such as atoms and electrons. The indirect approach combines the traditional thermal characterizations with the nanoscale techniques, which is universal for all the thermal properties.

Using the second approach, including in-situ thermal experiments, one can measure and explore the thermal properties directly. This enables research of interfaces, defects, edge and size effects on low-dimensional materials and response of the material to the applied temperature, called thermometry. Nowadays, there are three types of thermometry that can be used for the in-situ nanoscale thermal characterization.

The first type is the scanning probe-based method which is widely used (3; 4; 5; 6; 7). Here, the temperature is usually measured via a calibrated sensor in contact and in thermal equilibrium with the system, such as a thermistor where the electronic resistance is related to the temperature. Although a spatial resolution of a few nanometers has been reported by performing the measurements in high vacuum (7), the resolution of these methods is limited by the size of the cantilever tip and the tip-surface contact characteristics. The relatively slow

scanning rate and the assumption of thermal equilibrium also limit the time resolution of this type of measurement, restricting its applicability in dynamic systems.

The second type is the non-contact optical techniques, such as Raman (8), fluorescence (9), and luminescence thermometry (10), which utilize the temperature-dependent phenomena, then convert the measured signal into a temperature value. Although these techniques provide an accurate prediction of temperature after careful calibration, the spatial resolution is restricted by the optical diffraction limit. Moreover, in the first two type of methods, particularly SPM, it is difficult to prepare free-standing specimens, and the measured material is often supported by a substrate. The substrate effects are difficult to be excluded and will always impact the measurement.

The third type is based on electron microscopy techniques. The earliest method is electron diffraction which utilizes the electron diffraction of particles at different temperatures to monitor the lattice expansion and then measure the temperature (11). These techniques will give a precise measurement of temperature based on the statistical average of a large number of particles, but the artifact from additional particles cannot be avoided and the spatial resolution is limited. A more recent study by Idrobo *et al.* (12) measures the temperature of BN nanoflakes using the ratio between the probabilities of the same energy transfer in electron energy gain and loss spectrum. Combining with the calculations of phonon energy, this method is independent of the type of materials. Since the approach is based on vibrational spectroscopy in the aloof-beam configuration, it will result in limited beam damage effect, but also have a very limited spatial resolution.

The aim of this Ph.D. thesis is to systematically develop indirect and direct thermal characterization techniques to investigate the defect and size effects on the thermal properties at the nanometer scale. These techniques I have developed will utilize the scanning transmission electron microscopy (STEM), electron energy-loss spectroscopy (EELS) and first-principles calculations. These techniques are universal across a wide range of different materials, from thermoelectric materials to atomically thin metallic and semiconducting materials.

In the first two chapters, the background and theory behind these techniques will be described. It will include the STEM probe formation, the background of STEM imaging and EELS, and the background of density functional theory for material modeling. In Chapter 4, an indirect approach is introduced and utilized to explore the physical origin of Ti dopants effects on the Seebeck coefficients in the thermoelectric material, $Ca_3Co_4O_9$, by the atomic-resolution characterization and first-principles modeling. A complete study of the structural and electronic properties of Ti dopants in $Ca_3Co_4O_9$ and the subsequent influence on the Seebeck coefficients will be discussed. Chapter 5 will introduce a novel and universal technique of the direct nanoscale thermal characterization on the thermal expansion. It will be used to explore the thermal expansion behavior of 2D materials, including transition metal dichalcogenide (TMD) and graphene. The negative thermal expansion of graphene will be demonstrated and thickness effects on the thermal expansion of 2D materials will be studied. In Chapter 6, a study of the thermal expansion of alloyed TMD will be reported. The substitutional defect effects in alloys on the thermal expansion will be investigated and the origin of these effects will be discussed. In the last chapter, the current results from the nanoscale thermal character-

ization techniques and the exploration of the nanoscale thermal properties will be summarized and future research will be discussed.

CHAPTER 2

SCANNING TRANSMISSION ELECTRON MICROSCOPY

Any discussion of transmission electron microscope (TEM) has to begin by mentioning the well-known physicist, Louis de Broglie. In 1924, he proposed the matter wave theory in his Ph.D. thesis, which postulated that not only light, but all matter exhibits wave-like properties (13). This theory built the foundation of wave-particle duality and was confirmed experimentally three years later. In 1927, Clinton Joseph Davisson and Lester Halbert Germer from Bell labs, observed the first diffraction pattern of electrons using the low energy electrons hitting a nickel crystal (14). In the same year, George Paget Thomson (son of Joseph John Thomson, who discovered the electrons) observed the interference phenomena of electrons using an electron beam transmitting through a metal film (15). After these discoveries, in 1929, De Broglie won the Nobel Prize for his hypothesis of matter wave theory. In the same year, a Ph.D. candidate from Technische Universität Berlin, Ernst Ruska, proposed to utilize high-energy electrons with extremely short wavelengths for microscopy to exceed the spatial resolution limit of optical devices. In 1931, Ernst Ruska and Max Knoll built the first transmission electron microscope (16). And two years later, Ruska's electron microscope had already exhibited a higher spatial resolution than any traditional optical microscope. In 1937, Baron Manfred von Ardenne at Siemens built the first scanning transmission electron microscope (STEM) (17). However, this technique was not fully developed. In 1969, Albert Crewe from University of Chicago developed the field emission gun in STEM which largely improved the spatial resolution (18). Since then,

the electron microscopy has been largely developed and are now widely used in research and industry.

In this chapter, I will introduce the STEM, including the formation of a small electron beam using the probe aberration correction, how electrons interact with the sample, and how we detect them for different applications.

2.1 Probe Formation

In the transmission electron microscope, the coils replace the optical lenses to focus the electron beam. They can operate magnetically or electrostatically. The configuration behind the transmission electron microscope can be divided into four parts: 1) the electron source formation, 2) a lens system for magnification, 3) interactions between incident electrons and samples, and 4) detection of scattered electrons. Unlike the conventional TEM in which the incident electrons are parallel and produce a coherent image after scattering, in the STEM, the electron beam is designed to converge to form a small probe at the sample which is scanned in a raster pattern over the area of interest. This model allows the detection of incoherent elastically scattered electrons at a high angle, which can form the incoherent image and provide a high spatial resolution.

The electron source largely influences the size of the probe which determines the resolution of STEM images. Usually, the electron source in TEM is the thermionic emission gun, such as lanthanum hexaboride (LaB_6) filaments. The thermionic emitter will give electrons enough thermal energy to overcome the energy barriers from work functions. Due to necessary high temperatures, the devices cannot provide a sharp enough electron source and exhibit poor

reliability and lifetime. In 1969, the field emission gun was developed and the prototype of the modern STEM was created (18). A sketch of the field emission gun is shown in Figure 1. In the field emission gun, a sharp tip will be exposed to a negative potential compared using a very close electrode. With enough potential difference, the electrons will be emitted from the tip. Compared with the thermionic emitter, the field emission gun can provide a more coherent and sharp source with a much larger brightness, hence largely improve the spatial resolution of images.

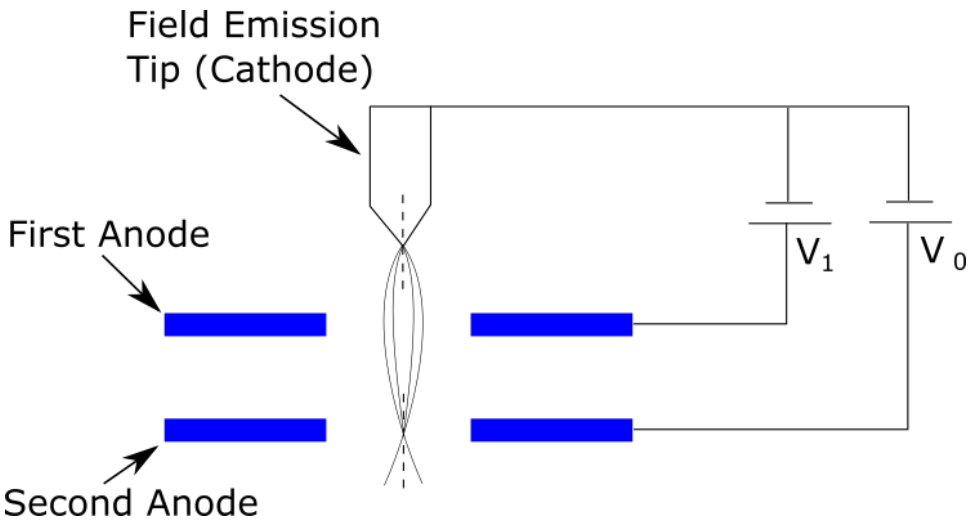

Figure 1: A sketch of the field emission gun.

After the beam of electrons extracted from the tip, it is focused to a cross-over by the gun lens. Then the beam is converged by the systems of condenser lenses, called C1 and C2. This initial convergence provides the main demagnification of the microscope and can occur at different heights. The closer the cross-over is to the lens, the smaller spot size at the convergence point. This spot size can be controlled by the current of condense lenses system (since the

strength of magnetic field can be tuned by the current flowing through the coils) and affects the final probe size. After the beam is converged by the condenser lenses system, it is then deflected by the scanning coils which enable the raster scan through the electromagnetic shifts. The gun lens, the condenser lenses and the object lens guarantee that sufficient demagnification can be achieved. However, large source demagnification will limit the number of electrons in the incident beam and influence the signal-noise ratio of images and spectra. A tradeoff between the spatial resolution and the signal-noise ratio of images needs to be considered when choosing the appropriate spot size.

2.2 Aberration Correction

The final probe size on the sample determines the resolution in STEM images. In particular, the aberrations of the probe are the main limitations of the spatial resolution in STEM images. The aberrations of the lenses system are mainly two types: chromatic aberration, and spherical aberration. The first type, the chromatic aberration, means that electrons of different energies (i.e. with different wavelengths) are focused to different focal points on the optical axis. The second type, the spherical aberration, comes from the different behavior of off-axis beams, which is the most significant aberration in STEM lens system. Specifically, the rays which are far away from the optical axis are bent more strongly to a closer focus point, compared with the rays close to the optical axis. A schematic of both aberrations is presented in Figure 2.

The spherical aberration transfers a point image to a halo with the highest intensity in the center. This effect largely influences the probe size and limits the spatial resolution of a STEM.

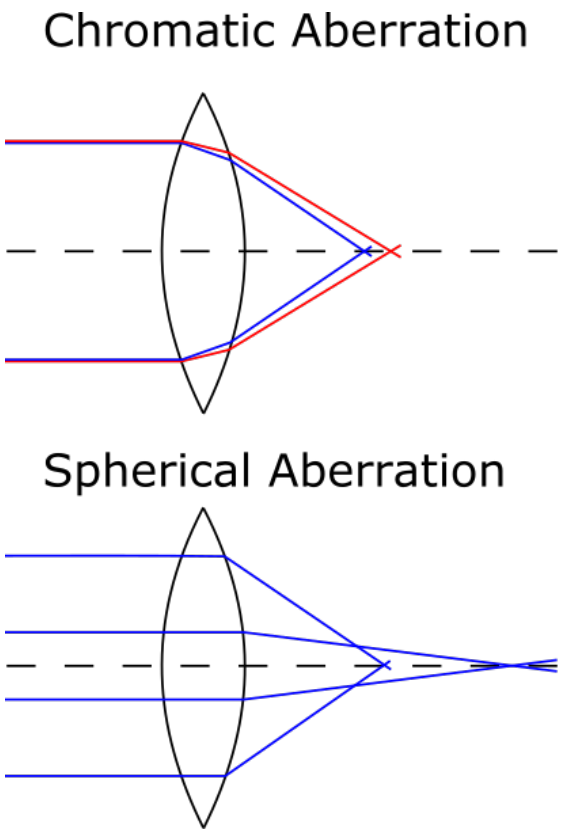

Figure 2: A schematic of chromatic aberration (upper panel) and spherical aberration (lower panel). Adapted from (19).

If the non-rotationally symmetric aberrations are ignored, the wavefront distortion from the perfect sphere, i.e. the spherical aberration function, can be expanded in a power series:

$$\chi(\theta) = \frac{1}{2}\Delta f\theta^2 + \frac{1}{4}C_3\theta^4 + \frac{1}{6}C_5\theta^6 + \frac{1}{8}C_7\theta^8 + \cdots \tag{2.1}$$

where Δf is the first-order distortion (defocus), C_3, C_5, C_7 are the coefficients of the third-, fifth- and seventh-order spherical aberrations, respectively. In an uncorrected electron microscope, the main contribution of aberrations comes from C_3.

The lateral spread effect from the spherical aberration can be measured by the lateral displacement in the Gaussian focus plane, which is the gradient of the aberration function:

$$\delta(\theta) = \Delta f\theta + C_3\theta^3 + C_5\theta^5 + C_7\theta^7 + \cdots \tag{2.2}$$

The individual contribution from each order of aberrations to the lateral spread of the probe is shown in Figure 3. As the semi-angle θ increases, the effect from diffraction decrease while the contribution from the spherical aberration increases. The smallest probe size can be selected at an angle that introduces minimum lateral displacement considering all the diffraction and aberrations. In Figure 3, the smallest probe size is chosen at point A for the uncorrected system and at point B for C_3-corrected system (which excludes the lateral displacement from C_3). It can be shown that the probe size at point B is almost half of the size from point A, which presents the importance of C_3 corrections.

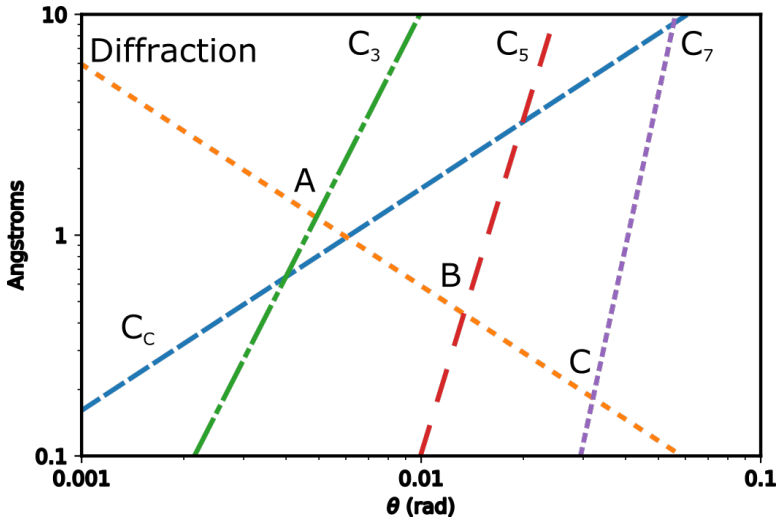

Figure 3: The lateral spread of probe from the contributions of the diffraction and different aberrations. Adapted from (20).

The aberration correction has been a long-standing challenge for electron microscopy. In 1949, Otto Scherzer suggested that the aberration correction cannot be realized by the traditional lenses with rotational symmetry, but can be achieved by the multipole lenses instead (21). In the late 1990s, the first aberration correctors were built for TEM by Haider (22) and for STEM by Krivanek (23). With the development of the aberration correctors, the first sub-angstrom experiment was performed by Batson from IBM in 2002 (24). The spherical aberration corrector in the ARM 200CF I used is a hexapole corrector. With this kind of probe spherical aberration corrector, the spatial resolution of 0.78 Å at the 200 kV accelerating voltage, can be achieved.

2.3 Electron interactions with matter

As I described in the former sections, it took more than 60 years to realize aberration correction and achieve a sub-angstrom scale electron probe before hitting the sample. What happens then when the probe finally hits the sample?

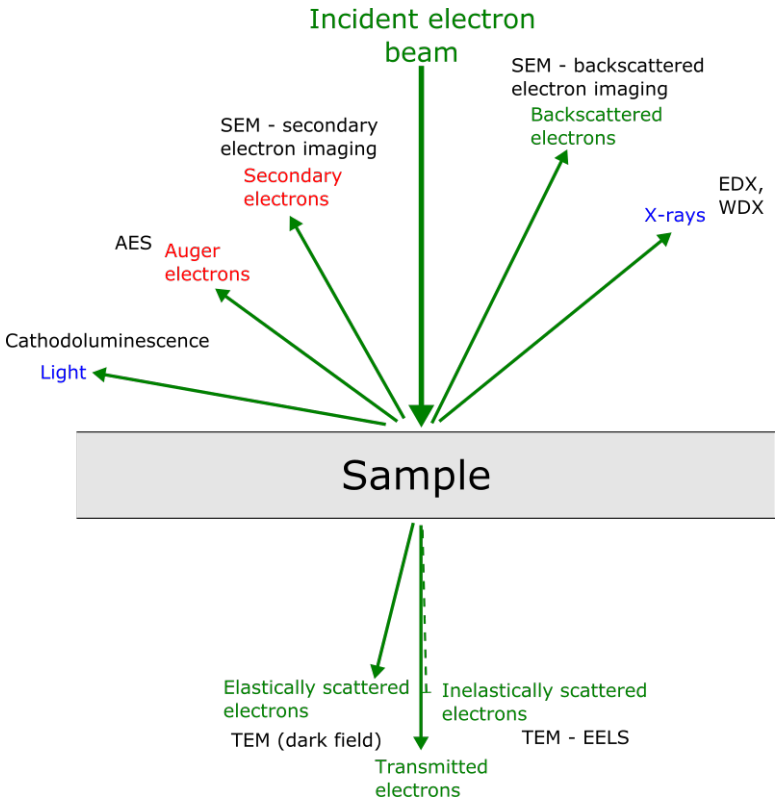

Figure 4: The schematic of possible phenomena resulted from the electron interactions with the sample. Adapted from (25).

When high energy electrons interact with the sample, a variety of phenomena occur and can be observed by different techniques (Figure 4), which shows the great potential of a comprehensive analysis based on the electron microscope. For a high energy electron, these phenomena are resulted from the electron interactions with the sample at different penetration depths:

From secondary electrons for surface structural information by scanning electron microscope (SEM), to the transmitted electrons for TEM. The electrons transmitting through the sample can be divided into different types due to the different interactions: transmitted electrons (no scattered), elastically scattered electrons for structural information, and inelastically scattered electrons for chemical information of materials.

Usually, the inelastic scattering occurs in a small angle ($< 0.1\,\text{deg}$) and the incoherent elastic scattering occurs over a large angle ($> 3\,\text{deg}$). Due to a small probe size of the beam and different collection angles, these two signals can be obtained simultaneously for both images and spectra. In fact, the atom-by-atom structural and chemical analysis can be achieved using STEM. In the next two subsections, I will introduce the techniques of displaying elastically and inelastically scattered electrons for STEM analysis.

2.4 Z-contrast Image

The main imaging techniques of STEM utilize the elastically scattered electrons for structural analysis. The detectors below the sample stage could include an annular bright field detector (ABF), a low angle annular dark field detector (LAADF), and a high angle annular dark field detector (HAADF). A schematic of the setup for these three detectors and corresponding accepted scattering angles are presented in Figure 5. The ABF detector collects the directly transmitted electron beam at a small scattering angle (< 10 mrads) with the central area being blocked, which can be used to detect the light elements (Li, O, etc.). The ADF detectors are the ring-shaped detectors collecting the elastically scattered electrons at a high angle ($10 - 50$ mrads for LAADF, > 50 mrads for HAADF). The LAADF images can be used

for the low-dimensional materials since the elastic scattering at the high angle is weak after transmitting the low-dimensional materials, while the HAADF images can provide a better atomic number (Z) contrast for the heavy elements. In this subsection, I will discuss the elastic scattering of electrons with atoms and the HAADF imaging, or also called Z-contrast imaging.

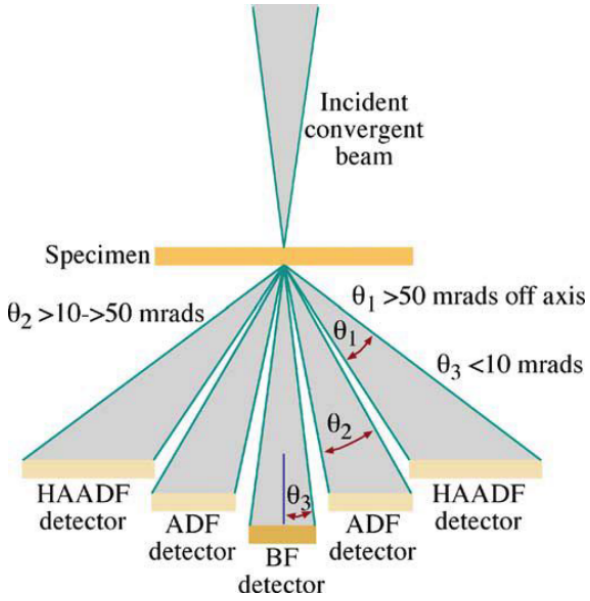

Figure 5: A schematic of the setup of ABF, ADF, and HAADF detectors. All the detectors gather electrons with different scattering angles simultaneously. Taken from (25) with permission.

Figure 6 is a diagram of elastic scattering with an isolated atom. When an incident electron is far away from the nucleus, the incident electron mainly interacts with the electron cloud around the nucleus due to the Coulomb interaction. This interaction is weak and scatters the electron slightly with a small angle. When the incident electron is close to the nucleus, the strong electron-nucleus Coulomb interaction scatters this electron with a large angle. In

some situations (the electron is too close to the nucleus), the electron may be completely backscattered. This strong scattering is called Rutherford scattering.

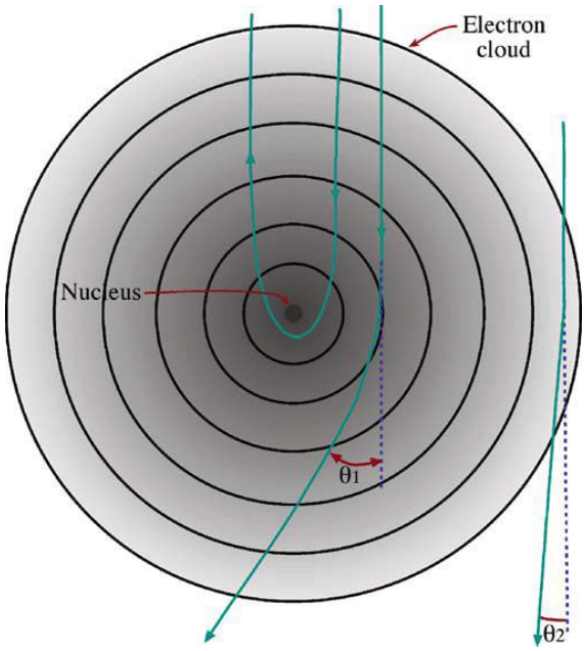

Figure 6: A diagram of two elastic scattering mechanisms: low-angle scattering due to electron-electron Coulomb interactions and high-angle scattering due to electron-nucleus Coulomb interactions (some may completely backscattered). Taken from (25) with permission.

If the relativistic effects are ignored and there is no energy transfer during the scattering (elastic scattering), the differential cross section for the Rutherford scattering can be expressed as:

$$\sigma_{\mathrm{R}}(\theta) = \frac{e^4 Z^2}{16(4\pi\varepsilon_0 E_0)^2} \frac{d\Omega}{\sin^4 \frac{\theta}{2}} \tag{2.3}$$

where E_0 is the energy of the electrons, Z is the atomic number of the isolated atom. From this simple model, I can find that the differential cross section, i.e. the possibility of the elastic scattering at a certain angle, is proportional to Z^2. The HAADF detector collects these high

angle elastically scattered electrons and integrates the intensities of electrons to produce the HAADF image. The intensity of electrons in each pixel presents the possibility of electrons scattering in that area, which is proportional to Z^n ($n = 1.6 - 2$ for different experimental conditions (18; 26; 27)). The advantages of HAADF imaging are that it excludes the thickness effects on the contrast and it is not sensitive to changes in objective lens defocus. Due to the incoherent properties of high angle elastic scattering, the HAADF images are not affected by the diffraction contrast which gives a better spatial resolution. Due to these advantages, the HAADF images are widely used for the initial elemental recognition and high-resolution structural analysis in bulk, defects, and interfaces.

2.5 Electron Energy-Loss Spectroscopy

There are two types of spectroscopy commonly used in a STEM: energy-dispersive X-ray spectroscopy (EDS) and electron energy-loss spectroscopy (EELS). The positions of EDS and EELS detectors within the TEM column are shown in Figure 7. The EDS detector above the sample collects the characteristic X-rays emitted from the sample, while the EELS detector below the sample gathers the inelastically scattered electrons which are separated based on the energies by a magnetic prism. I will briefly discuss the mechanisms of both techniques: inelastic scattering.

Figure 8 presents the mechanisms behind EELS. When a high energy electron interacts with an atom, it can transfer energy to electrons around the atom which may cause the excitation of a plasmon or the excitation of the electron from the inner shell orbitals to the unoccupied outer shell orbitals. The latter excitation leaves a hole in the inner shell orbital. In these processes,

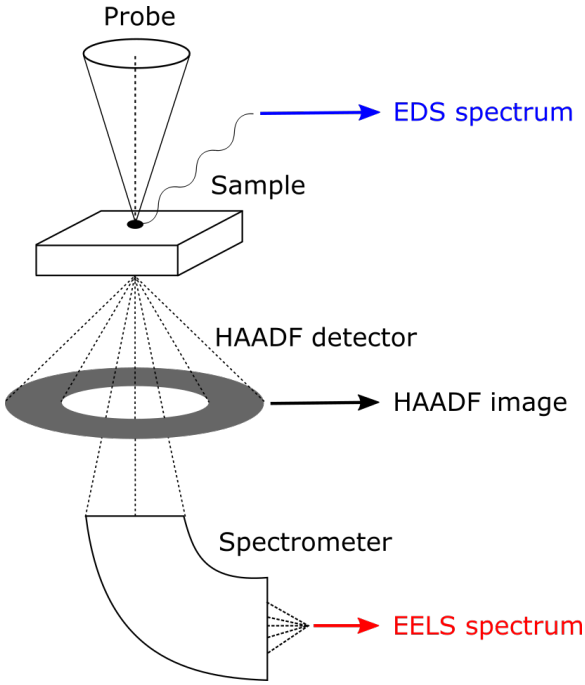

Figure 7: A schematic of the layout of EDS, HAADF, EELS detectors.

the original electron loses the certain energy for the excitation. These energy-loss electrons are used for EELS techniques. An outer shell electron can then jump back to this inner shell hole and release energy. This transition energy can be transferred to eject another outer shell electron from the atom (Auger electron), or can be released as the characteristic X-rays for EDS techniques.

For a small scattering angle ($\theta << 1$ rad), the double-differential cross section for inelastic scattering can be approximated as:

$$\frac{d^2\sigma}{d\Omega dE} \approx \frac{8a_0^2R^2}{Em_0v^2}\left(\frac{1}{\theta^2+\theta_E^2}\right)\frac{df}{dE} \tag{2.4}$$

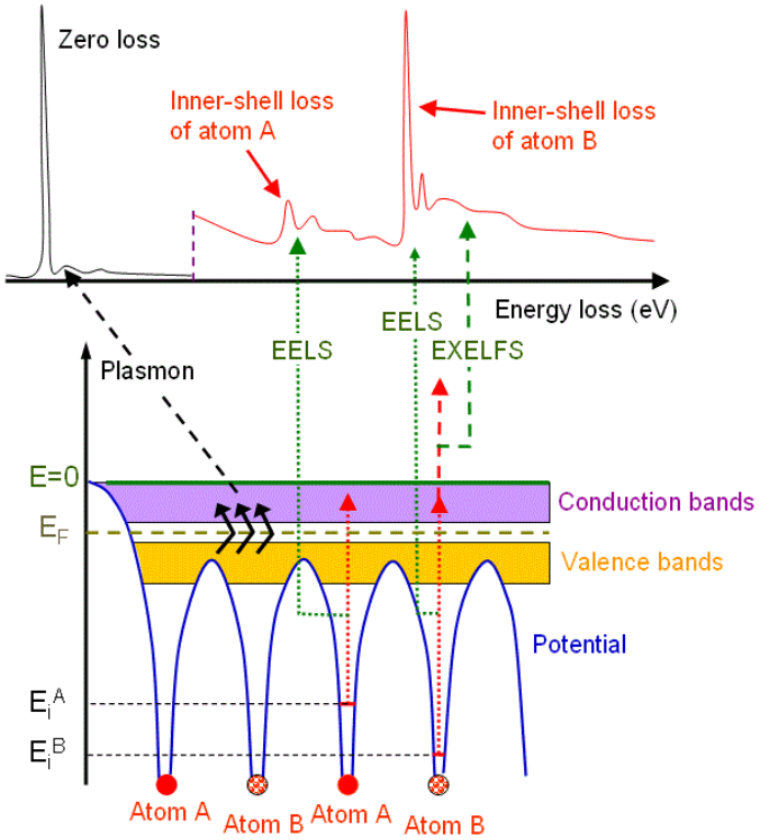

Figure 8: A schematic of electron excitations during the electrons interactions with matter (lower panel) and the corresponding spectrum in EELS (upper panel). Taken from (28).

where a_0 is the Bohr radius, R is the Rydberg energy, $\frac{df}{dE}$ is the generalized oscillator strength (GOS) per unit energy loss, and m_0, v are the static mass and velocity of incident electrons. θ_E is the characteristic angle. If the relativistic effect is ignored, it can be approximated as $\theta_E = E/(2E_0)$, where E_0 is the energy of the incident electron. The angular dependence of the inelastic scattering mainly stems from the Lorentzian factor $\left(\frac{1}{\theta^2+\theta_E^2}\right)$, in which the θ_E describes the half-width at half maximum (HWHM).

Equation 2.4 is applied for single atoms situation which is particularly useful for the inner shell scattering. However, the outer shell scattering is complicated due to the collective behavior of the valence electrons. Alternatively, I can consider the interaction of the incident electron with the solid by the dielectric response function, $\varepsilon(q, E)$. Then Equation 2.4 can be expressed as:

$$\frac{d^2\sigma}{d\Omega dE} \approx \frac{\mathrm{lm}[-1/\varepsilon(q,E)]}{\pi^2 a_0 m_0 v^2 n_a} \left(\frac{1}{\theta^2+\theta_E^2}\right) \tag{2.5}$$

where n_a is the number of atoms per unit volume, θ_E is the same characteristic angle. For a typical STEM at 200 kV acceleration voltage, θ_E is approximately 1 mrad for a 400 eV energy loss and 0.05 mrad for a 20 eV energy loss. For the plasmon excitation in the low-loss region ($0 - 50$ eV), the energy dependence of the inelastic scattering mainly comes from the factor $\mathrm{lm}[-1/\varepsilon(q,E)]$, which is called energy-loss function. The low-loss EELS can be simulated based on this factor with the calculations of dielectric response function. More details will be discussed in Chapter 5.

2.5.1 Zero-loss Peak

A typical EEL spectrum (the number of electrons as a function of different energy-loss) is shown in Figure 8. Based on the energy range, the EEL spectrum can be roughly divided into three regions: the zero-loss peak (0 eV), the low-loss EELS ($0 - 50$ eV) and the core-loss EELS (> 50 eV). Each region has its unique functions for further spectroscopic analysis.

The first (at 0 eV) and most intensive peak in the low-loss EEL spectrum is the zero-loss peak (ZLP). It comes from the transmitted electrons, low-angle elastically scattered electrons and inelastic scattering with a tiny energy loss (such as the phonon excitation). Since most electrons are found from the direct beam, the ZLP can be used to focus the spectrometer. Due to its sharpness and special position, the ZLP can be always set as the zero point for the energy calibration. The full-width at half maximum (FWHM) of ZLP is the energy resolution of the EEL spectrum, which mainly stems from the energy distribution of the electron source ΔE_0, the energy broadening from the spectrometer ΔE_{so}, and the spatial resolution of the EELS detector s. Since these factors are independent with each other, the total energy resolution can be written as:

$$\Delta E^2 = \Delta E_0^2 + \Delta E_{so}^2 + (s/D)^2 \tag{2.6}$$

where D is the energy dispersion of the spectrometer. Due to the energy dependency of spectrometer focusing, the ΔE_{so} term increases as the energy loss increases. As a result, the overall energy resolution in the core-loss region is slightly worse than the one in the low-loss region. However, the main contribution is the energy spread of electron source ΔE_0, which depends on

the type of electron source. For a 100 keV situation, the energy resolution from the cold FEG ($\sim$ 0.3 eV) is much better than those from the W source ($\sim$ 3 eV) and LaB_6 source ($\sim$ 1.5 eV) (25). This is another advantage of FEG than the traditional thermionic emitter.

The ZLP also contains the signal from phonon excitation. Since the energy loss during phonon excitation (50 $-$ 300 meV) is too small compared with the energy resolution of the traditional EEL spectrum (0.2 $-$ 1 eV), this weak signal is covered by the tail of ZLP and is hard to be detected. However, a monochromated FEG can further narrow the energy spread, and an energy resolution of 5 - 50 meV can be achieved, which is sufficient to explore the fine details in the ultra low-loss region of EELS ($<$ 1 eV).

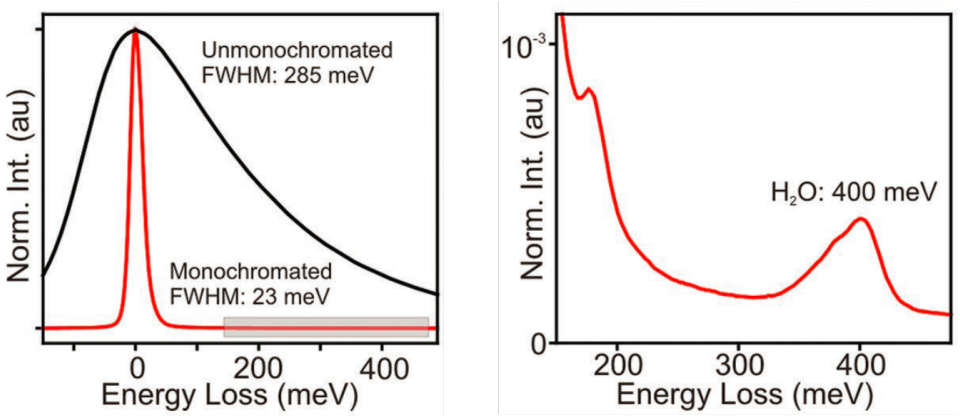

Figure 9: The comparison of ZLP energy resolutions before and after the electron probe is monochromated (left panel) and the monochromated ultra low-loss EEL spectrum of water cell sandwiched by *h*-BN monolayer films, showing the phonon from *h*-BN ($\sim$ 180 meV) and the phonon of O-H stretching from water ($\sim$ 400 meV) (right panel). Taken from (29) with permission.

A direct comparison of ZLP from unmonochromated and monochromated electron source is shown in Figure 9. After monochromating the probe, the energy resolution from the FWHM of ZLP is reduced from 285 meV to 23 meV, which enables the detection of the phonon modes

of h-BN (∼180 meV) and H_2O (∼ 400 meV). With the high energy resolution, an aloof mode EELS (the beam passes near the edge of the sample, not directly transmits the sample) is possible. the beam damage from EELS can be largely reduced. Another application of ZLP is the detection of fine details in the electron energy-gain spectrum (EEGS) (12). It comes from the energy transfer from the photos to the electrons and is symmetric with the energy-loss tail of ZLP. Since it is the reverse excitation of energy-loss, the intensity ratio between the same peaks from the energy gain and loss spectrum is a Boltzmann factor ($e^{-\frac{\Delta E}{k_B T}}$). This means that as energy difference ΔE increases the intensity of EEGS exponentially decreases. Only the fine details of the ultra low-gain region can be observed with a monochromator. Since the Boltzmann factor is temperature dependent, it can be used to predict temperature based on the intensity ratio (12).

2.5.2 Low-loss EELS

The low-loss EELS presents the excitations of the valence electron in the outer shell including the interband transition and the plasmon excitation. The interband transition presents the single excitation from the outer shell orbitals (conduction band) to the unoccupied orbitals (valence band). For a semiconductor, the initial onset of the background-subtracted low-loss EELS is the band gap of materials (the energy of the transition from the highest occupied orbital to the lowest unoccupied orbital). The plasmon is a collective behavior of electron oscillation. The analysis of plasmon can be used to reveal the thickness of the sample, the valence electron density, and the temperature (2).

A typical plasmon wake is shown in Figure 10. When a fast electron moves into the solid, the nearby electrons are pushed away due to the Coulombs interactions, leaving a correlation hole with a positive effective charge in the space. After the incident electron moves away, the nearby electrons are attracted back and fill the hole with a negative charge in the space. When the speed of the incident electron is fast enough (larger than the Fermi velocity), it forms an oscillation of alternately positive and negative charge in the space behind the incident electron. This effect is called the plasmon wake. In this process, the attracting force from the positively charged correlation hole causes the energy loss. This transition can be regarded as the creation of pseudoparticles, plasmon, with a quantum of energy $E_p = \hbar\omega_p$, where ω_p is the plasmon frequency.

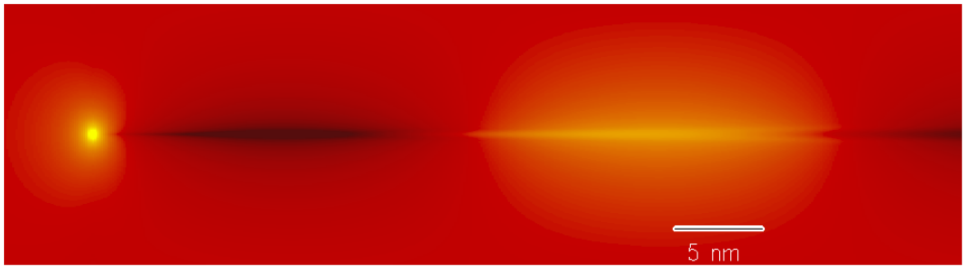

Figure 10: The plasmon wake from a 100 keV electron. Bright spot is the fast-moving electrons, while the bright and dark areas present the regions with negative and positive charges. Taken from (30) with permission.

In the free-electron approximation, the energy-loss function $\mathrm{lm}[-1/\varepsilon(E)]$ (from Equation 2.5) of a volume plasmon can be written as:

$$\mathrm{Im}\left[\frac{-1}{\varepsilon(E)}\right] = \frac{E_p^2(E\hbar/\tau)}{(E^2 - E_p^2)^2 + (E\hbar/\tau)^2} = \frac{E(\Delta E_p)E_p^2}{(E^2 - E_p^2)^2 + (E\Delta E_p)^2} \tag{2.7}$$

where τ is the relaxation time of the plasmon, E_p is the plasmon energy, ΔE_p is the full width at half-maximum (FWHM) of the energy-loss function and equals $\hbar/\tau$. This energy-loss function reaches the maximum at the energy loss:

$$E_{\max} = [E_p^2 - (\Delta E_p^2/2)]^{1/2} \tag{2.8}$$

For a sharp peak (ΔE_p is small), the maximum is approximately at the plasmon energy $E_p = \hbar\sqrt{\frac{ne^2}{m\epsilon_0}}$, where n is the valence electron density. This peak can be utilized for the analysis of the collective behavior of electrons and monitoring the change of the valence electron density, which thus enables the measurement of the lattice expansion of materials. More details will be discussed in Chapter 5.

Another important application of the low-loss EELS is the thickness measurement. If we consider the inelastic scattering as an independent event, the probability of an incident electron being inelastically scattered n times in a sample of thickness t should follow the Poisson statistics:

$$P_n = I_n/I_t = (1/n!)m^n exp(-m) = (1/n!)(t/\lambda)^n exp(-t/\lambda) \tag{2.9}$$

where I_n is intensity of n-fold scattering, I_t is the total intensity. m is the average number of collisions and can be approximated as $m = t/\lambda$, where λ is the mean free path of the inelastic scattering.

Considering the unscattered situation ($n = 0$, zero-loss peak), Equation 2.9 gives:

$$t/\lambda = \ln(I_t/I_0) \tag{2.10}$$

where I_0 is the intensity of the zero-loss peak, which can be calculated using the integrals of ZLP after the ZLP extraction. λ values are tabulated for most oxides, and Equation 2.10 can be used to measure the thickness t of the sample. However, both the analysis of plasmon and measurement of thickness require a careful ZLP extraction. Otherwise, it can easily introduce numerical errors to the analysis.

2.5.3 Core-loss EELS

The core-loss EELS comes from the electron excitations of core-shell electrons to the unoccupied orbitals. Based on the level of core shell (i.e. K, L, M, etc.), the corresponding core loss edge is named K-, L-, or M-edge, etc. This process requires enough energy to support the transition from the core-shell electrons of a specific atom to its unoccupied orbitals in the conduction band. The energy-loss for each transition during this process depends on the type of elements and also the specific core-shell orbitals. For a specific core-shell orbital, the core loss edge reflects the density of states of the unoccupied orbitals above Fermi level. After the edge onset of the core loss edge, the subsequent regions are the electron loss near edge structure (ELNES) (up to 50 eV) and the weaker extended electron energy loss fine structure (EXELFS). These fine structures present the energy distribution of the empty states in the conduction

band, which can be used to analyze the detail electronic structure of materials, such as the orbital hybridization, chemical bonding, and spin-orbital coupling.

Since the core electrons are strongly bonded with the nucleus, collective effects can be ignored. For inelastic scattering of the core electrons, the single atom model can be applied and Equation 2.4 can provide a good approximation of the characteristics of the core loss edges. In Equation 2.4, the main energy distribution comes from the general oscillation strength, $df(q, E)/dE$. This term is analytically solved for the hydrogen atom, which can be used for others atoms with certain scalings. In a $q \to 0$ limit, this term gives the core loss edges a sawtooth shape, i.e. a sudden increase after the ionization energy followed by an exponential decay.

A typical core loss EEL spectrum of $BaTiO_3$ thin film showing Ti L-edge and O K-edge is presented in Figure 11. In addition to the sawtooth shapes of both edges, up to 50 eV above the energy onset, the electron loss near edge structure (ELNES) can be analyzed for the information of the conduction band of the corresponding atom. For example, the ELNES of Ti L exhibits the characteristics of four splitting sharp peaks, which stem from the mixing effect of the spin-orbital coupling and the octahedral crystal field splitting. And the energy shift and intensity change of these four peaks can be used to analyze the change of valence state, spin state, and concentration of Ti atoms. More details will be discussed in Chapter 4.

Since the background follows approximately an inverse power law, the background for each element can be subtracted by an exponential fitting (Figure 11). With a background subtraction, the rest signal spectrum can be used for elemental quantification based on the integral

intensity under the core loss edge from each element. For a $BaTiO_3$ thin film, the quantification gives the atomic ratio of O over Ti element, 2.93, which is close enough to the ideal atomic ratio, 3, with a 2.3% error. Compared with the elemental quantification by EDS, EELS provides a more sensitive and more localized information of concentration distribution of different elements.

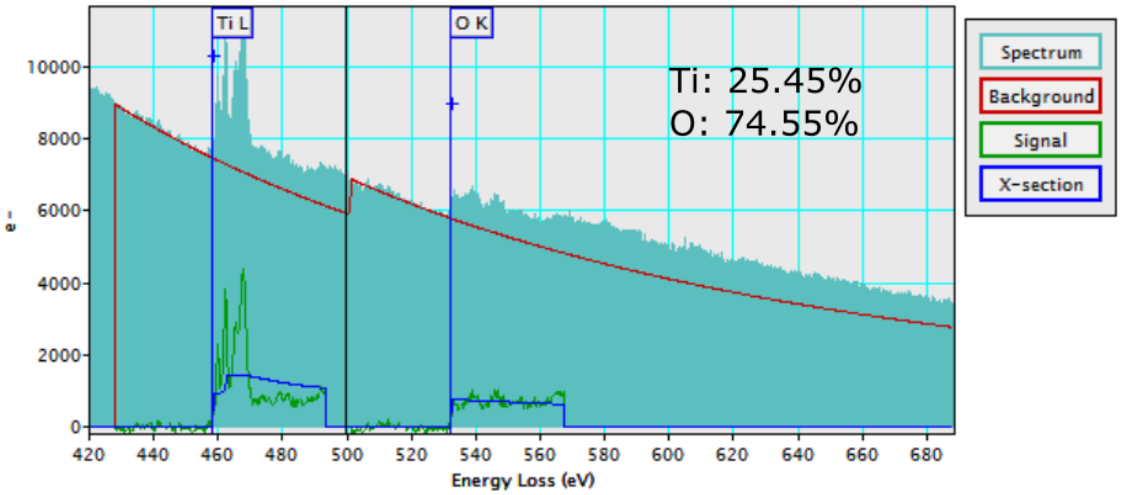

Figure 11: The core loss EEL spectrum of $BaTiO_3$ showing Ti *L*-edge and O *K*-edge with background subtractions for the elemental quantification. The atomic ratio of Ti over O atoms is 2.93 based on the quantification.

2.6 The UIC JEOL JEM-ARM200CF

Figure 12 shows the scanning electron transmission microscope (JEOL JEM-ARM200CF) I used for my Ph.D. research. This JEOL JEM-ARM200CF is located at University of Illinois at Chicago and equipped with a cold FEG and a probe spherical aberration corrector which provides an energy resolution of 0.35 eV and a spatial resolution of 0.78 Å at 200 kV, 1.36 Å at 80 kV for HAADF imaging.

The imaging system includes a BF/ABF detector, a LAADF detector, a HAADF detector, and a Gatan ADF/BF detector. Up to four detectors can be used for imaging simultaneously. For the spectroscopic analysis, this microscope is equipped with an Oxford X-Max 100TLE SDD X-ray detector for capturing EDS signal and a Gatan Quantum GIF for recording EELS signal. Both detectors are capable of the atomic column-resolved mapping. In addition, a Gatan double-tilt heating stage is used for the in-situ heating experiment in this thesis.

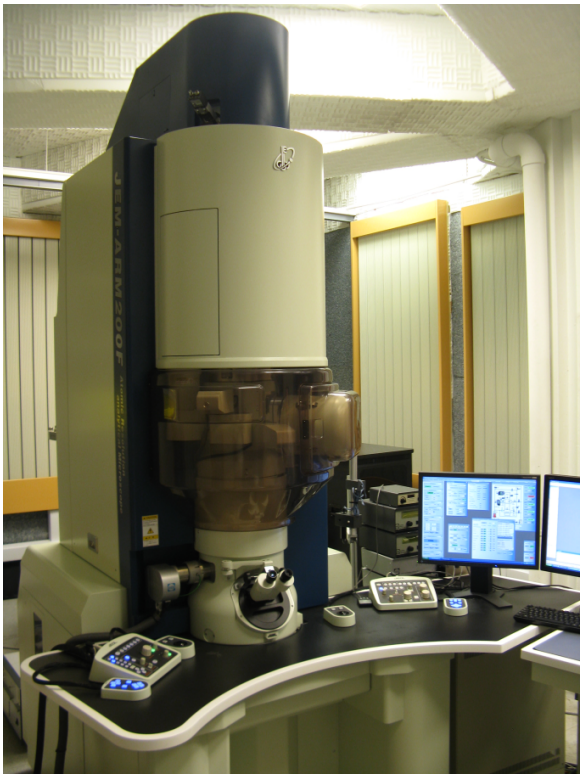

Figure 12: The scanning electron transmission microscope (JEOL JEM-ARM 200CF) used in this thesis at University of Illinois at Chicago.

CHAPTER 3

FIRST-PRINCIPLES SIMULATIONS

Computational physics, especially the first-principals calculations, contributes its crucial efforts to understanding the physics behind phenomena and predicting the behavior of materials for new technologies. In this chapter, I will briefly introduce the first-principles calculations in the framework of the density functional theory (DFT). Specifically, I will discuss the background of DFT (Born-Oppenheimer approximation, two Hohenberg-Kohn theorems, approximations for the exchange-correlation functional) and an application in DFT frame to calculate dielectric function and simulate EELS (random phase approximation).

3.1 Born-Oppenheimer Approximation

While quantum mechanics can, in principle, enable us to solve the relevant equations of motion, and thus, predict all properties of solid, finding the exact solution of the Schrödinger equation for a solid is impossible due to the numerous degrees of freedom and the complexity of interactions among them. To simplify the problem, several approximations have been applied in computational materials science.

The first step is the adiabatic approximation proposed by Max Born and J. Robert Oppenheimer in 1927 (31). Since electrons are three to four orders of magnitude lighter than the nuclei, they move much faster than the nuclei, responding to changes in nuclear degrees of freedom almost instantaneously. The time that the electrons need to reach a stable state

at a given ionic configuration is so little that the nuclei can practically be considered to be static. This assumption provides us a way to decouple the dynamics of nuclei and electrons: $\psi(\{\mathbf{R}_I\},\{\mathbf{r}_i\}) = \psi_{\text{ion}}(\{\mathbf{R}_I\}) \times \psi_e(\{\mathbf{r}_i\})$, where $\psi(\{\mathbf{R}_I\},\{\mathbf{r}_i\})$ is the wavefunction for a solid consisting of M ions (with configuration $\{\mathbf{R}_I, I = 1, ..., M\}$) and N electrons ($\{\mathbf{r}_i, i = 1, ..., N\}$). At each instant, the nuclei form an external potential in which the surrounding electrons will be redistributed to reach a most s state (the ground state of $\psi_e(\{\mathbf{r}_i\})$).

Specifically, with a fixed ionic distribution $\{\mathbf{R}_I, I = 1, ..., M\}$, the electronic ground state can be calculated by solving the many-body Schrödinger equation:

$$\hat{H}\psi_e(\{\mathbf{r}_i\}) = E\psi_e(\{\mathbf{r}_i\}) \tag{3.1}$$

where E is the total energy of the system. The Hamiltonian $\hat{H}$ can be written as:

$$\begin{aligned} \hat{H} &= -\frac{\hbar}{2m_e}\sum_i \vec{\nabla}_i^2 + \frac{1}{2}\sum_{i\neq j}\frac{e^2}{|\mathbf{r}_i - \mathbf{r}_j|} + \frac{1}{2}\sum_{i,I}\frac{Z_I e^2}{|\mathbf{r}_i - \mathbf{R}_I|} + \frac{1}{2}\sum_{I\neq J}\frac{Z_I Z_J e^2}{|\mathbf{R}_I - \mathbf{R}_J|} \\ &= \hat{T} + \hat{U} + \hat{V}_1 + \hat{V}_2 \end{aligned} \tag{3.2}$$

These terms represent the kinetic energy of the electrons, the Coulomb interaction between electrons, the interaction between ions and electrons, and the interactions between ions, respectively. The last two terms contribute to the external potential for electrons ($\hat{V}_{\text{ext}} = \hat{V}_1 + \hat{V}_2$) and depend on the ionic configuration. By changing this configuration and solving the Schrödinger equation, the corresponding total energy surface can be depicted. Based on the configuration

of electrons and nuclei, the forces on the ions can be calculated and the ions move accordingly to reach the most stable atomic configuration.

The calculations of the many-body problem in solid are largely simplified by the Born-Oppenheimer approximation with an excellent accuracy, but still need more approximations for the complex electron-electron and electron-ion interactions. To approximate these interactions, I will introduce density functional theory (DFT) and approximations for the exchange-correlation functional, respectively.

3.2 Density Functional Theory

Finding the solutions of electronic Schrödinger equation is still complicated, since the ground state wavefunction $\psi(\mathbf{r}_1, \mathbf{r}_2, ..., \mathbf{r}_N)$ has $3N$ degrees of freedom, where N is the number of electrons. In the 1960s, Walter Kohn and Pierre Hohenberg proposed a new approach, in the form of the two Hohenberg-Kohn theorems, to address the complexity of the problem (32).

The first theorem states that the properties of ground state $\psi(\mathbf{r}_1, \mathbf{r}_2, ..., \mathbf{r}_N)$ can be uniquely described by the electron density $n(\mathbf{r})$ which is a function of only three degrees of freedom. This idea largely simplifies the calculations of electronic Schrödinger equation and triggers the development of density functional theory.

The second theorem describes the variational principle to find the ground state using the electron density. In particular, there exists a functional $E[n]$ of the electron density $n(\mathbf{r})$, which can be written as,

$$E[n] = T[n] + U[n] + \int V_{\text{ext}}(\mathbf{r}) n(\mathbf{r}) \mathrm{d}^3\mathbf{r} \tag{3.3}$$

that assumes its minimum for the correct ground state density $n(\mathbf{r})$. Here, $T[n]$ and $U[n]$ are the expectation values of the kinetic and Coulomb interaction energy operators in the ground state. Only the external potential term will depend on the system we choose. The minimization of this energy functional with respect to $n(\mathbf{r})$ at a given number of electrons will provide us the ground state energy E_0 and ground state electron density n_0.

In 1965, this theory was further developed by Walter Kohn and Lu Jeu Sham (33). They proposed a framework to simplify the complex many-body problem by mapping it into a single body problem. In this framework, each non-interacting electron moves in an effective external potential which produces the same electron density $n_s(\mathbf{r})$ as the one for the system of interacting electrons ($n(\mathbf{r})$). This effective potential (V_{eff}) consists of the external potential from electron-nuclei interaction and the electron-electron interaction. The single electron Schrödinger equations in this framework are called Kohn-Sham equations:

$$\left(-\frac{\hbar}{2m_e}\vec{\nabla}_i^2 + V_{\text{eff}}(\mathbf{r})\right)\varphi_i(\mathbf{r}) = \varepsilon_i\varphi_i(\mathbf{r}) \tag{3.4}$$

where φ_i is the single electron wavefunction and ε_i is the energy. The electron density can be calculated as:

$$n(\mathbf{r}) \overset{\text{def}}{=} n_s(\mathbf{r}) = 2\sum \varphi_i^*(\mathbf{r})\varphi_i(\mathbf{r}) \tag{3.5}$$

In this framework, the energy functional can be expressed as:

$$E[n] = T_s[n] + \int V_{\text{ext}}(\mathbf{r})n(\mathbf{r})\mathrm{d}^3\mathbf{r} + E_H[n] + E_{xc}[n], \tag{3.6}$$

where $T_s[n]$ is the kinetic energy of non-interacting electrons, $E_H[n]$ is the Hartree term which presents the classical Coulomb repulsive interactions between electrons:

$$E_H[n] = \frac{e^2}{2} \int \frac{n(\mathbf{r})n(\mathbf{r}')}{|\mathbf{r} - \mathbf{r}'|} \mathrm{d}\mathbf{r}\mathrm{d}\mathbf{r}', \tag{3.7}$$

and $E_{xc}[n]$ is the exchange-correlation energy functional, which includes all the effects of the many-body character of the real interacting system.

At a given electron density $n(\mathbf{r})$, the effective potential can be then written as:

$$V_{\text{eff}}(\mathbf{r}) = V_{\text{ext}}(\mathbf{r}) + e^2 \int \frac{n(\mathbf{r}')}{|\mathbf{r} - \mathbf{r}'|} \mathrm{d}\mathbf{r}' + \frac{\delta E_{xc}[n(\mathbf{r})]}{\delta n(\mathbf{r})} \tag{3.8}$$

Iteratively, at the given effective potential, the wavefunctions of the Kohn-Sham equations can be calculated by Equation 3.4 and thus determine the electron density of the system by Equation 3.5. The iterations continue until typically the total energy converges within a certain tolerance level. In these calculations, the exchange-correlation functional $E_{xc}[n]$ is the only unknown term in the Kohn-Sham framework but can be approximated well, which is discussed in the next subsection 3.3.

3.3 Approximations for the Exchange-Correlation Functional

The calculation of the exchange-correlation term needs further approximations. The most commonly used class of approximations is based on the local-density approximation (LDA) (33), which assumes that the exchange-correlation functional only depends on the electron density

at each spatial position, but not on its derivatives. The exchange-correlation functional then can be written as,

$$E_{xc}^{\mathrm{LDA}}[n(\mathbf{r})] = \int n(\mathbf{r})\epsilon_{xc}(n(\mathbf{r}))\mathrm{d}\mathbf{r}. \tag{3.9}$$

Here, $\epsilon_{xc}[n]$ is the exchange-correlation term of a homogeneous electron gas (HEG) at density n.

We can linearly separate the exchange-correlation functional into exchange part and correlation part:

$$E_{xc} = E_x + E_c \tag{3.10}$$

Within the HEG model (constant electron density), the exchange term E_x can be analytically determined. The correlation term E_c can be approximated using several methods in which the numerical results obtained on the HEG are fitted to various functional forms (34; 35; 36; 37). Due to its simple assumption, LDA gives good results in systems where the electron density changes slowly but makes a poor description in systems where the density variation is large, e.g. in atoms. In general, the LDA tends to underestimate the exchange term E_x and overestimate the correlation term E_c.

To correct these shortcomings of LDA, a better class within the so-called generalized gradient approximation (GGA) was proposed. Within GGA the exchange-correlation functional depends

on the electron density of the system as well as the gradient of local electron density. The exchange-correlation functional for GGA can be presented as:

$$E_{xc}^{\mathrm{GGA}}[n(\mathbf{r})] = \int n(\mathbf{r})\epsilon_{xc}(n, \nabla n)\mathrm{d}\mathbf{r} \tag{3.11}$$

The GGA provides very good results for a wide range of materials, especially in the relaxation of crystal structures and prediction of ground state energies. The information of the local gradient can be built into the GGA functional using various approaches, in which the Perdew-Wang functional (PW91) (38) and the Perdew-Burke-Ernzerhof functional (PBE) (39) are most common for solids. In this thesis, I will use GGA-PBE functional for all the first-principles calculations.

3.4 Random Phase Approximation

The treatments of LDA and GGA on the exchange-correlation functional enable the DFT calculations of different materials scaling up to a few hundred atoms and successfully predict the materials properties, such as the lattice parameters, formation energies, and band gaps, to assist the understanding of the materials. However, the shortcomings of both approximations are well known. The LDA tends to provide a bad estimation on the formation energies or binding energies of molecules and solids (40). LDA and GGA may underestimate and overestimate the lattice constants of solids, respectively (41). There are a variety of treatments focusing on improving the accuracy of predicting the exact electronic structure of materials in different dimensionality (from molecules, surfaces to bulk solids) (42). In these methods, the random

phase approximation (RPA) exhibits a promising improvement on the calculations of small band gap semiconductors or metals. More importantly, RPA can yield a frequency dependent dielectric functions of solids, which can accurately predict the response of the electron gas, such as plasmon.

The RPA can be considered in the DFT framework through the adiabatic connection fluctuation dissipation (ACFD) theorem (43). In this theorem, the exchange-correlation functional can be constructed by introducing the Coulomb interactions between electrons in an adiabatic connection path which fixes the charge density at its expected value. In the RPA, the exchange-correlation functional (E_{xc}^{RPA}) can be considered separately into, the exact exchange term (E_{x}^{EX}) and the RPA correlation term (E_{c}^{RPA}) (44),

$$E_{xc}^{\mathrm{RPA}} = E_{x}^{\mathrm{EX}} + E_{c}^{\mathrm{RPA}}, \tag{3.12}$$

where,

$$E_{x}^{\mathrm{EX}} = -\sum_{ij} f_i f_j \int\int \mathrm{d}\mathbf{r}\mathrm{d}\mathbf{r}^{'} \psi_i^*(\mathbf{r})\psi_j(\mathbf{r})\nu(\mathbf{r},\mathbf{r}^{'})\psi_j^*(\mathbf{r}^{'})\psi_i(\mathbf{r}^{'}), \tag{3.13}$$

and

$$E_{c}^{\mathrm{RPA}} = \frac{1}{2\pi}\int_0^\infty \mathrm{d}\omega \mathrm{Tr}\left[\ln(1-\chi_{i\omega}^0\nu) + \chi_{i\omega}^0\nu\right]. \tag{3.14}$$

Here, $\chi_{i\omega}^0$ is the non-interacting response function of the reference system featured by the single electron orbitals ψ_i and occupation factors f_i.

The RPA calculations in DFT framework are typically non-self-consistent calculations after a standard DFT calculation in LDA or GGA. The wavefunction from the standard DFT calculations will provide a reference energy and virtual unoccupied states for the RPA calculations. Here, I will use this standard method to calculate the frequency dielectric function of the materials for the EELS simulations.

CHAPTER 4

SEEBECK COEFFICIENT OF $Ca_3Co_4O_9$

Parts of this chapter were previously published as X. Hu, P. J. Phillips, D. Mazumdar, J. C. Idrobo, S. Kolesnik, A. Gupta, S. Öğüt, and R. F. Klie, "Atomic and electronic structure of Ti substitution in $Ca_3Co_4O_9$", J. Appl. Phys. 120, 205105 (2016).

4.1 Introduction

Over the last few decades, the quest for high-efficiency thermoelectric (TE) materials has attracted great attention, since the thermoelectric effect, i.e. direct conversion of heat into electrical energy, is an important method for power generation (45) and electronic refrigeration (46). As an eco-friendly energy source, the thermoelectric power has the potential to be an alternative to traditional fossil fuels. The thermoelectric efficiency can be presented by the figure of merit $ZT = \frac{S^2T}{\rho\kappa}$, where T, S, κ, ρ, are the temperature, Seebeck coefficient, thermal conductivity, and electrical resistivity, respectively. Large Seebeck coefficient, low electrical resistivity, and low thermal conductivity are required for good TE materials.

While many different material systems have been studied, the class of thermoelectric oxides holds particular promise for achieving high thermal and environmental stability. One class of thermoelectric oxides, the incommensurately layered $Ca_3Co_4O_9$ (CCO), also reported as $[Ca_2CoO_3][CoO_2]_{1.62}$, stands out as a material with a high in-plane Seebeck coefficient (47; 48; 49), high thermoelectric of merit ($ZT \sim 1$ at 1,000° C) (50), and high temperature stability. The

atomic, electronic and thermal properties of pristine CCO have been studied extensively both experimentally and theoretically (47; 48; 49; 50; 51; 52; 53; 54; 55; 56; 57; 58; 59; 60; 61; 62; 63; 64; 65; 66; 67; 68; 69; 70). CCO is made up of two monoclinic subsystems, alternatively stacked along the c-axis: the Ca_2CoO_3 subsystem (rock salt (RS) type), and the CoO_2 subsystem (CdI_2-type). Both subsystems have the same $a = 4.8339$ Å and $c = 10.8436$ Å lattice parameters, but they are incommensurately stacked along the b-axis, with lattice constants of $b = 4.5582$ Å and 2.8238 Å for the RS and CoO_2 subsystems, respectively (51). It was previously demonstrated that the RS subsystem plays the role of a charge-carrier reservoir, while the CoO_2 layers are p-type conducting (52).

In strongly correlated oxide materials, such as CCO, the Seebeck coefficient can be determined using the Heikes formula (58):

$$S = -\frac{k_B}{e} \ln\left(\frac{g_3}{g_4}\frac{1-x}{x}\right), \tag{4.1}$$

where g_3 (g_4) is the orbital degeneracies of Co^{3+} (Co^{4+}) in the CoO_2 layer, respectively, and x is the Co^{4+} concentration. Previous studies have found that the Co^{4+} concentration in the CoO_2 layers is $x = 0.5$, which results in a Co valence state of +3.5 (52; 53). Based on Equation 4.1, we can show that this mixed-valence state in the CoO_2 layer is responsible for the large Seebeck coefficient (assuming a low spin-state for both the Co^{3+} and Co^{4+} ions) and for the observed p-type conductivity in CCO. However, it can also be seen that at $x = 0.5$, S is limited to 155 $\mu V/K$, which has since been confirmed experimentally (59).

Several studies have suggested various methods to improve the thermoelectric performance of CCO, more specifically the figure of merit, ZT. First, based on Equation 4.1, one can increase the Seebeck coefficient by manipulating the orbital degeneracy via a Co-ion spin-state transition. There are several ways to achieve this spin-state transition, including exerting compressive strain on the CoO_2 layer, isovalent doping and defect engineering. For example, recent studies on CCO thin films have shown that the presence of CoO_2 stacking faults could give rise to a Co^{4+} spin-state transition, which stabilizes the Co^{4+} in an intermediate state and increases the Seebeck coefficient (59; 60). However, the application of bi-axial strain using a lattice mismatch between the substrate and the single crystal CCO films has proven to be less successful (60).

Secondly, one can increase the Seebeck coefficient by increasing the Co^{4+} concentration x, i.e. increasing the valence state of Co in the CoO_2 layer. Doping the Ca, or the Co sites in both subsystems, is a possible approach to influence the valence state of Co in CoO_2 layer and improve the TE properties of CCO (63; 64; 65; 66; 56; 57; 54; 55; 68). Since Co atoms play a key role in the electronic and thermal properties of CCO, doping on the Co sites is more likely to have a significant influence on the electronic and thermal properties (56; 57; 54; 55; 68). To minimize the structural changes while maintaining a high doping concentration, the ionic size of the dopants on the Co sites should be similar to that of Co, which limits the possible dopants to the transition metals from Ti to Zn in the periodic table. For instance, one study has reported that Fe dopants at the Co sites of CCO increase the Seebeck coefficient and decrease the electronic resistivity simultaneously (67). Similarly, another study has shown that the Fe

and Mn substitution of Co atoms in the CoO_2 layer enhance the electronic correlations in the system, while the Cu substitution of Co in the RS layer does not affect the electronic and magnetic properties (63).

In a recent study by Xu *et al.* (69), it was suggested that Ti dopants introduce a significant increase in the Seebeck coefficient. The authors proposed that when the concentration of Ti dopants is less than $x = 0.2$ for $Ca_3Co_{4-x}Ti_xO_9$, Ti atoms mainly replace Co atoms in the RS subsystem, while, as x approaches 0.3, Ti dopants start to substitute Co atoms in both subsystems. The authors found that when Ti replaces Co in the CoO_2 layer, the Seebeck coefficient increases from 130 μV/K to above 175 μV/K (71). However, a more recent study on Ti-doped CCO by Torres *et al.* showed that while Ti substitution results in a decrease of electrical resistivity, there is no appreciable change in the Seebeck coefficient (70). It should be noted that these doping studies have been conducted on poly-crystalline bulk samples without a comprehensive understanding of Ti dopant effects on the local atomic and electronic structures.

In this chapter, I use a combined experimental and theoretical approach to determine the effects of Ti doping on the structural and electronic properties of CCO. More specifically, I combine aberration-corrected STEM/EELS, DFT calculations and pulsed-laser deposition (PLD) thin-film synthesis to study the structure and transport properties of Ti-doped CCO. I find that for 100 nm thick films grown on $SrTiO_3$ [001], there is no difference in the Seebeck coefficients of Ti-doped and pristine CCO (60). I determine the structure of Ti-doped CCO both experimentally and theoretically, and find that Ti doping has very little effect on either the local atomic structure or the density of states of Co in the CoO_2 subsystem. The rest

of this chapter is organized as follows: In Sec. II, I provide the details of experimental and computational methods. The structure of Ti-doped CCO and the position of the Ti dopants are discussed in Sec. III. In Sec. IV, I present EELS and DFT studies for the electronic structure of Ti-doped CCO. Finally, in Sec. V, I discuss and summarize my findings in light of previously published results.

4.2 Methods

4.2.1 Experimental Methods

Ti-doped CCO thin films ($Ca_3Co_{3.8}Ti_{0.2}O_9$) were deposited by PLD with a Coherent Lambda Physik Excimer laser ($\lambda = 248$ nm, repetition rate is between 4 and 8 Hz). The films were 100 nm thick and grown on a (001)-oriented $SrTiO_3$ substrate. The optimal condition was found with laser fluence at 1.5 J/cm^2 and oxygen pressure at 300 mTorr. More details on the thin films synthesis of CCO can be found in Ref. (60). All atomic-resolution STEM images presented here were acquired on a Nion UltraSTEM at Oak Ridge National Laboratory, operated at 100 kV. The semi-convergence angle for high-angle annular dark field (HAADF) imaging was chosen to be 30 mrad, which results in an image intensity proportional to approximately Z^2 (18; 26; 27). To analyse the influence on the electronic structure, the EEL spectra were acquired with a dispersion of 0.5 eV per channel to record the O K-, Ti L- and Co L-edges simultaneously. The Seebeck coefficient was measured by using a physical property measurement system (Quantum Design) equipped with a thermal transport option (60).

4.2.2 Computational Methods

First-principles calculations within the framework of density functional theory (DFT) were performed using the Perdew-Burke-Ernzerhof (PBE) (35; 39) exchange-correlation functional in the Vienna Ab Initio Simulation Package (VASP) (72). Since $Ca_3Co_4O_9$ can be expressed as $[Ca_2CoO_3][CoO_2]_{1.62}$, Rebola *et al.* (61; 62) suggested that the incommensurately layered CCO can be modeled using rational approximants of composition $[Ca_2CoO_3]_{2F(n)}[CoO_2]_{2F(n+1)}$ where $F(n)$ are Fibonacci numbers $(1, 1, 2, 3, 5, 8, ...)$. Their study showed that the 5/3 approximant, which leads to a composition of $[Ca_2CoO_3]_6[CoO_2]_{10}$ with 66 atoms in the unit cell, does a good job in modeling the essential electronic properties of CCO. Here, I used the same 5/3 unit cell for all the calculations and tested some of my results using a smaller unit cell of composition $[Ca_2CoO_3]_4[CoO_2]_6$ (i.e. the 3/2 approximant with 42 atoms). After careful convergence tests, 550 eV plane wave cutoff energy and 6×3×3 Monkhorst-Pack k-point mesh were used for the 5/3 and 3/2 unit cells. For the convergence of the calculations, the energy threshold for the self-consistent field (SCF) is set to 10^{-6} eV. In the ionic relaxations, the conjugate-gradient algorithm (73) is used and the force threshold is set to 0.001 eV/Å. In the calculation of density of states (DOS), 12×6×6 Monkhorst-Pack k-point mesh (74) and the tetrahedron method with Blochl corrections were selected. In all calculations, spin-polarization was considered to analyse the spin state transition. To model moderate electronic correlations in CCO, my calculations were performed within the PBE+U framework. The on-site Coulomb interaction was considered with Hubbard U = 5 eV and Hund exchange J = 1 eV on Co atoms following Dudarevs approach (61). For Ti-doped CCO, I tested $U - J$ values ranging from 0 to

4 eV on the Ti atom. Different effective U values resulted in essentially the same characteristics in the density of states. Therefore, I chose an effective $U = 0$ eV on the Ti atom for simplicity.

Defect formation energies were computed as a function of the chemical potentials μ_i (i =Ti, Co, Ca, O) using well-established methods with grand canonical ensembles (75; 76; 77).

$$\mathrm{E_{form}} = \mathrm{E_{defect}} - \mathrm{n_{Ca}}\mu_{\mathrm{Ca}} - \mathrm{n_{Co}}\mu_{\mathrm{Co}} - \mathrm{n_{O}}\mu_{\mathrm{O}} - \mathrm{n_{Ti}}\mu_{\mathrm{Ti}} \tag{4.2}$$

where $\mathrm{E_{defect}}$ is the total energy of the CCO system with the corresponding defect, the n_i is the number of the atom i ($i = \mathrm{Ca, Co, O, Ti}$) in the CCO with the defect and μ_i is the chemical potential.

The boundaries of the individual chemical potentials were determined by using equilibrium with bulk CCO and by avoiding precipitation of secondary phases such as bulk Ca, CaO, Co, CoO, Co_3O_4, Ti, Ti_2O, TiO, Ti_2O_3, TiO_2, $CaTiO_3$ compounds and molecular oxygen.

4.3 Structural properties of Ti-doped CCO

To present the Ti dopant effects on the structure of CCO, the atomic resolution images are recorded for this comparison. Figure 13 shows the HAADF images of the pristine CCO and the nominally 100 nm thick Ti-doped CCO ($Ca_3Co_{3.8}Ti_{0.2}O_9$) single crystal film in the [110] projection. The layered structure of CCO includes the Ca_2CoO_3 subsystem with the RS structure and the CdI_2-type layers of the CoO_2 subsystem. The subsystems with three parallel layers of distinct atoms are in the RS structure, while the layers between the RS subsystems are the CoO_2 subsystems. These two sub-systems are stacked alternately along the c-axis.

Comparing the HAADF images for pristine and the Ti-doped CCO, the average Co-O bond length in the RS subsystem shrinks from 2.90 Å to 2.76 Å by 4.7% after doping, which still keeps the shape of structure. There is no apparent change in the crystal structure upon doping with Ti, suggesting that the Ti dopants do not influence the atomic structure significantly.

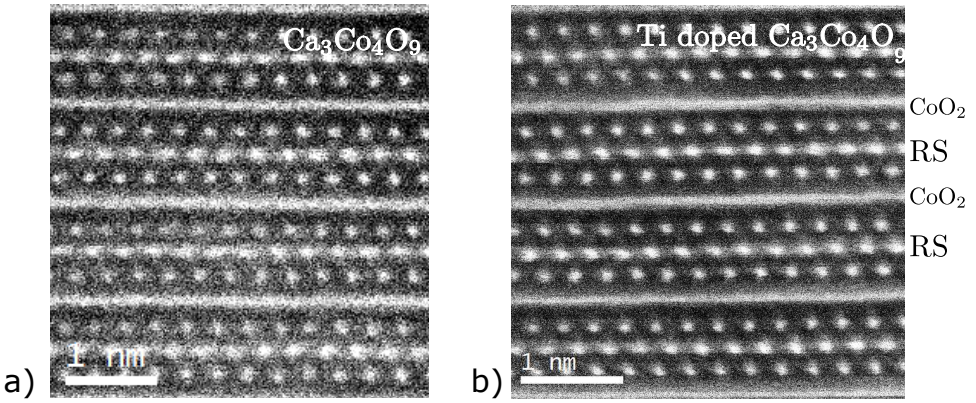

Figure 13: High-angle annular dark field (HAADF) images of a) the pristine CCO thin film and b) the Ti-doped CCO thin film both in the [110] projection.

In order to investigate this further, I performed first-principles calculations on the structure of the pristine and Ti-doped CCO. The optimized structure of pristine CCO with a 5/3 unit cell is shown in Figure 14. Figure 14a) shows the two alternatively stacked subsystems with each distinctive octahedral structure. The CoO_2 layer consists of CoO_6 octahedra with main axis tilted to [111] direction. In RS the CoO_6 octahedra are tetragonal distorted with compression along c axis.

After structural relaxation, I find a clustering with three units of Ca_2CoO_3 (denoted by X_3) along the *b* axis of the RS subsystem, which is a feature also observed by Rebola *et al.* (61). Due to this clustering, the CoO_6 octahedra on either side of X_3 are significantly distorted. This

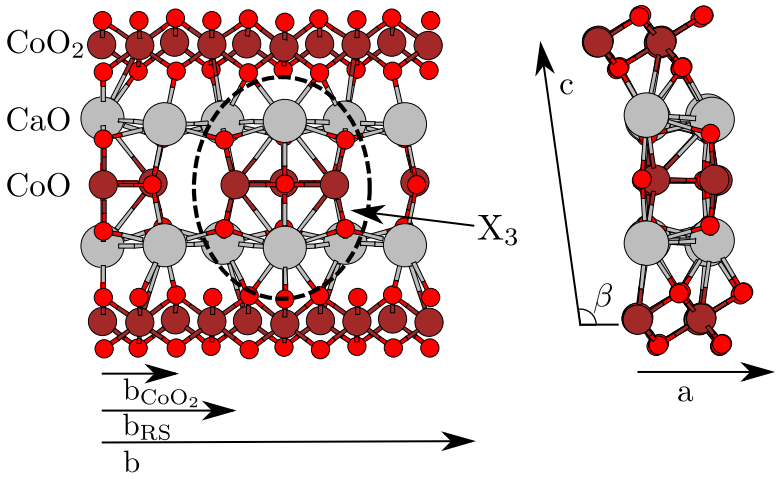

Figure 14: Relaxed structures of pristine CCO with a 5/3 approximant unit cell along the [100] (left) and [010] (right) directions. The grey, red, and dark red balls represent Ca, O, and Co atoms respectively. The clustering with three units of Ca_2CoO_3 (X_3) in the RS subsystem is highlighted with a dashed ellipse. The lattice constants along the b-axis for the RS and CoO_2 subsystems (b_{RS} and b_{CoO_2}) are also shown.

clustering is formed to release the shear stress between two subsystems, stemming from the mismatch of the unit ratio between the modeling and real situation.

The calculated lattice parameters (in Å) for the 5/3 approximant of bulk CCO are shown in Table I. The results are essentially the same as those obtained by Rebola *et al.* (61) and agree well with experimental data (51).

Next, I studied Ti dopants by substituting Ti for Co atoms (in RS or CoO_2 layer) or Ca atoms. All 16 Co sites and 12 Ca sites in the 5/3 unit cell have been considered. Figure 15 presents the optimized structures with Ti substitution at four inequivalent sites: the Co site in the middle of the X_3 cluster (Co1), the Co site on the side of the X_3 cluster (Co2), the Co site

TABLE I: Calculated lattice parameters (Å) for the 5/3 approximant of bulk CCO compared with previous calculations of Rébola *et al.* (61) and experimental data taken from Miyazaki *et al.* (51). b_{RS} and $b_{\mathrm{CoO_2}}$ are the lattice constants along the b-axis for the RS and CoO_2 subsystems, respectively.

System	a	b_{RS}	$b_{\mathrm{CoO_2}}$	c	β
5/3 (This work)	4.87	4.70	2.81	10.85	98.37°
5/3 (Rebola *et al.* (61))	4.88	4.71	2.82	10.85	98.34°
Experiments (Miyazaki *et al.* (51))	4.83	4.56	2.82	10.84	98.13°

in the CoO_2 layer, and the Ca site in RS. The changes of the average bond lengths are shown in Table II.

TABLE II: The average bond lengths (Å) in pristine CCO and corresponding bond lengths in defects. $\mathrm{Ti_{Ca}}$ is the defect when Ti substitutes the Ca atom in RS. $\mathrm{Ti_{Co1;RS}}$, $\mathrm{Ti_{Co2;RS}}$, $\mathrm{Ti_{Co;H}}$ are defects when Ti substitutes Co1 and Co2 in RS, Co in CoO_2 layer. $\mathrm{d_{RS}^{Co1}}$ is the average bond length of Co1-O bond in RS. $\mathrm{d_{RS}^{Co2;a}}$, $\mathrm{d_{RS}^{Co2;b}}$, $\mathrm{d_{RS}^{Co2;c}}$ are the average bond lengths of Co-O bond in RS along a, b, c axis respectively. $\mathrm{d_{RS}^{Ca}}$ is the average bond length of Ca-O bond in RS. $\mathrm{d_{CoO_2}^{Co}}$ is the average bond length of Co-O bond in CoO_2 layer.

Defect	Pristine	$\mathrm{Ti_{Ca}}$	$\mathrm{Ti_{Co1;RS}}$	$\mathrm{Ti_{Co2;RS}}$	$\mathrm{Ti_{Co;H}}$
$\mathrm{d_{RS}^{Co2;a}}$	1.97	-	-	1.86	-
$\mathrm{d_{RS}^{Co2;b}}$	2.01	-	-	1.91	-
$\mathrm{d_{RS}^{Co2;c}}$	1.80	-	-	1.83	-
$\mathrm{d_{RS}^{Co1}}$	1.90	-	1.93	-	-
$\mathrm{d_{RS}^{Ca}}$	2.42	1.99	-	-	-
$\mathrm{d_{CoO_2}^{Co}}$	1.91	-	-	1.91	1.97

When Ti substitutes Co1 in RS (Figure 15a)) or Co in CoO_2 layer (Figure 15c)), original CoO_6 octahedra become TiO_6 octahedra with a slight increase of average bond lengths and little

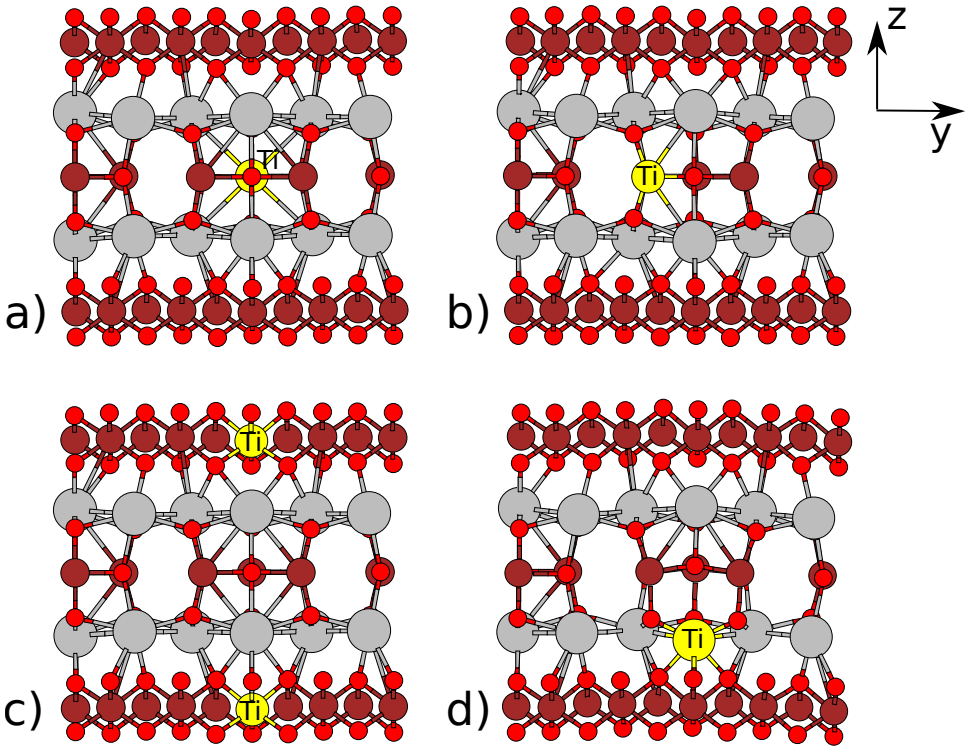

Figure 15: Optimized structures of Ti-doped CCO with Ti atom at a) the Co site in the middle of the X_3 cluster (Co1), b) the Co site on the side of the X_3 cluster (Co2), c) the Co site in the CoO_2 layer, d) the Ca site in RS. The yellow balls represent the Ti atoms.

change of the shape. When Ti substitutes Co2 in RS(Figure 15b)), Ti atom moves towards the center of the CoO_4 tetrahedron-like structure to get a tetrahedron TiO_4 with the decrease of the standard deviation of bond lengths ($d_{RS}^{Co2;a}$, $d_{RS}^{Co2;b}$, and $d_{RS}^{Co2;c}$) (from 0.11 Å to 0.04 Å). The calculations also show that Ti substitution will not result in any significant structural change. In summary, the average Ti-O bond lengths differ from the original Co-O bond lengths by only 1.6%, -3.1%, and 3.1%, when the Ti substitutes the Co atom (i) in the middle of X_3, (ii) on the side of X_3, and (iii) in the CoO_2 layer, respectively. This small changes of the bond-lengths are close to the result from previous experimental images.

When Ti substitutes a Ca atom (Figure 15d)), on the other hand, the percentage difference of the average Ti-O bond length from the original Ca-O bond length is found to be -17.8%. This shows that the structural changes induced by Ti substitution at Co sites are relatively small, while the Ti doping at a Ca site results in a significant reduction of bond length between the central ion and the ligands. This reduction of bond length is due to the more attractive potential caused by the additional positive charge of a Ti ion (4+) compared to a Ca ion (2+). These calculations along with the HAADF images (shown in Figure 13) suggest that Ti substitutes Co rather than Ca atoms, since the latter scenario would imply significant structural rearrangements not observed experimentally. However, this analysis does not provide sufficient insight to distinguish between Ti-doping at the RS or the CoO_2 subsystems, which I investigate next.

In order to determine the location of Ti dopants, I have performed atomic-resolution EELS measurements. Figure 16 (a-d) shows the Z-contrast and EEL spectrum images of CCO, includ-

ing the integrated Co, Ti, and Ca L-edge intensity distributions. Figure 16 (e) shows the profile of the Ti L-edge intensity integrated along the c axis. The integrated signal of Ti L-edge shows the relative concentration of the Ti dopants. I find that the Ti signal reaches its maximum at the CoO column of the RS subsystem. This implies that the Ti dopants mostly replace Co in the CoO column of the RS subsystem.

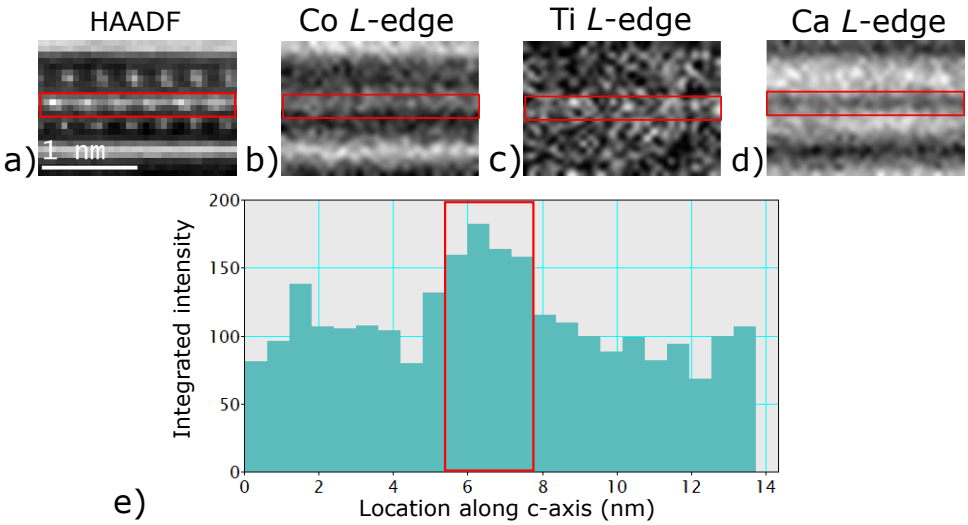

Figure 16: The Z-contrast (a) and EEL spectrum images (b-d) of CCO showing the integrated Co, Ti, and Ca L-edge distributions. The Ti L-edge intensity integrated along the c axis is shown in (e). The red rectangular region corresponds to the CoO layer of the RS subsystem.

To gain further insight about the location of Ti dopants, I used first-principles calculations to determine the formation energies of $\mathrm{Ti_{Co}}$ (Ti atom substituting a Co atom in either the RS or $\mathrm{CoO_2}$ layer) and $\mathrm{Ti_{Ca}}$ (Ti substituting a Ca atom) as a function of the individual chemical potentials μ_i ($i = \mathrm{Ti, Co, Ca}$). To compare different defects energetically, the formation energies $\mathrm{E_{form}}$ of defects in 5/3 unit cell are calculated by Equation 4.2.

In the meantime, the chemical potentials of different constituents are subject to the constraints

$$E^{bulk}_{CCO} = n_{Ca}\mu_{Ca} + n_{Co}\mu_{Co} + n_{O}\mu_{O}, \tag{4.3}$$

where E^{bulk}_{CCO} is the total energy of the CCO bulk.

When the defects are V_O, V_{Ca}, Ti_{Co}, Ti_{Ca}, the formulas of formation energy for different defects can be respectively reduced to:

$$\begin{aligned} E_{form} &= E_{V_O} - E^{bulk}_{CCO} + \mu_O \\ E_{form} &= E_{V_{Ca}} - E^{bulk}_{CCO} + \mu_{Ca} \\ E_{form} &= E_{Ti_{Co}} - E^{bulk}_{CCO} - \mu_{Ti} + \mu_{Co} \\ E_{form} &= E_{Ti_{Ca}} - E^{bulk}_{CCO} - \mu_{Ti} + \mu_{Ca} \end{aligned} \tag{4.4}$$

where E_X is the computed energy of CCO with defects X (V_O, V_{Ca}, Ti_{Co}, Ti_{Ca}).

In addition, to avoid the formation of other compounds, chemical potentials of different constituents are constrained in a growth region. Here I calculate energies of the following bulk compounds to introduce more constraints: Ca, CaO, $CaTiO_3$, Co, CoO, Co_3O_4, Ti, Ti_2O, TiO, Ti_2O_3, TiO_2. An isolated O_2 molecule has been calculated as well. Then the growth region can be determined by the following inequalities:

$$
\begin{aligned}
\mu_{Ca} &\leq \mu_{Ca}^{bulk} \\
\mu_{Ca} + \mu_O &\leq \mu_{CaO}^{bulk} \\
\mu_{Ca} + \mu_{Ti} + 3\mu_O &\leq \mu_{CaTiO_3}^{bulk} \\
\mu_{Co} &\leq \mu_{Co}^{bulk} \\
\mu_{Co} + \mu_O &\leq \mu_{CoO}^{bulk} \\
3\mu_{Co} + 4\mu_O &\leq \mu_{Co_3O_4}^{bulk} \\
\mu_{Ti} &\leq \mu_{Ti}^{bulk} \\
2\mu_{Ti} + \mu_O &\leq \mu_{Ti_2O}^{bulk} \\
\mu_{Ti} + \mu_O &\leq \mu_{TiO}^{bulk} \\
2\mu_{Ti} + 3\mu_O &\leq \mu_{Ti_2O_3}^{bulk} \\
\mu_{Ti} + 2\mu_O &\leq \mu_{TiO_2}^{bulk} \\
\mu_O &\leq \mu_O^{molecule}
\end{aligned}
\tag{4.5}
$$

where $\mu_{\mathrm{X}}^{\mathrm{bulk}}$ is the calculated energy of the bulk compound X, $\mu_{\mathrm{O}}^{\mathrm{molecule}}$ is half the energy of an isolated O_2 molecule.

To compare all the 4 defects, there are 4 variables to consider, μ_{Ca}, μ_{Co}, μ_O, μ_{Ti}. In order to find out the preferred defect for different Ti doping rates, we discuss the problem with different Ti concentrations, i.e. different μ_{Ti}. At a given Ti concentration, the inequalities (Equation 4.5) can be reduced to:

$$
\begin{aligned}
\mu_{Ca} &\leq \mu_{Ca}^{bulk} \\
\mu_{Ca} + \mu_O &\leq \mu_{CaO}^{bulk} \\
\mu_{Ca} + 3\mu_O &\leq \mu_{CaTiO_3}^{bulk} - \mu_{Ti} \\
\mu_{Co} &\leq \mu_{Co}^{bulk} \\
\mu_{Co} + \mu_O &\leq \mu_{CoO}^{bulk} \\
3\mu_{Co} + 4\mu_O &\leq \mu_{Co_3O_4}^{bulk} \\
\mu_O &\leq \mu_{Ti_xO}^{bulk} - x\mu_{Ti} \\
\mu_O &\leq \mu_O^{molecule}
\end{aligned}
\tag{4.6}
$$

For the other 3 variables, μ_{Ca}, μ_{Co}, μ_O, within the constraint (Equation 4.3), a ternary phase diagram has been calculated. The growth regions with different Ti concentrations are shown in Figure 17. Based on Equation 4.4, every point in this plot yields four formation energies for different defects. The defect with the least formation energy is presented by the corresponding color of that point. The color red, blue and green present the defect Ti_{Co}, V_O and V_{Ca}, respectively.

In Figure 17 a), due to the constraints of Equation 4.6, the growth region is just a point constrained by the compounds CoO, Co_3O_4, $CaTiO_3$, which reaches the maximum of μ_{Ti} as well. The change of the growth region as Ti concentration decreases is only reflected on the shift of the $CaTiO_3$ line towards Ca-poor area. As μ_{Ti} decreases, the growth region broadens and takes the shape of a triangle after μ_{Ti} is smaller than a certain value (Figure 17 c-e)). In

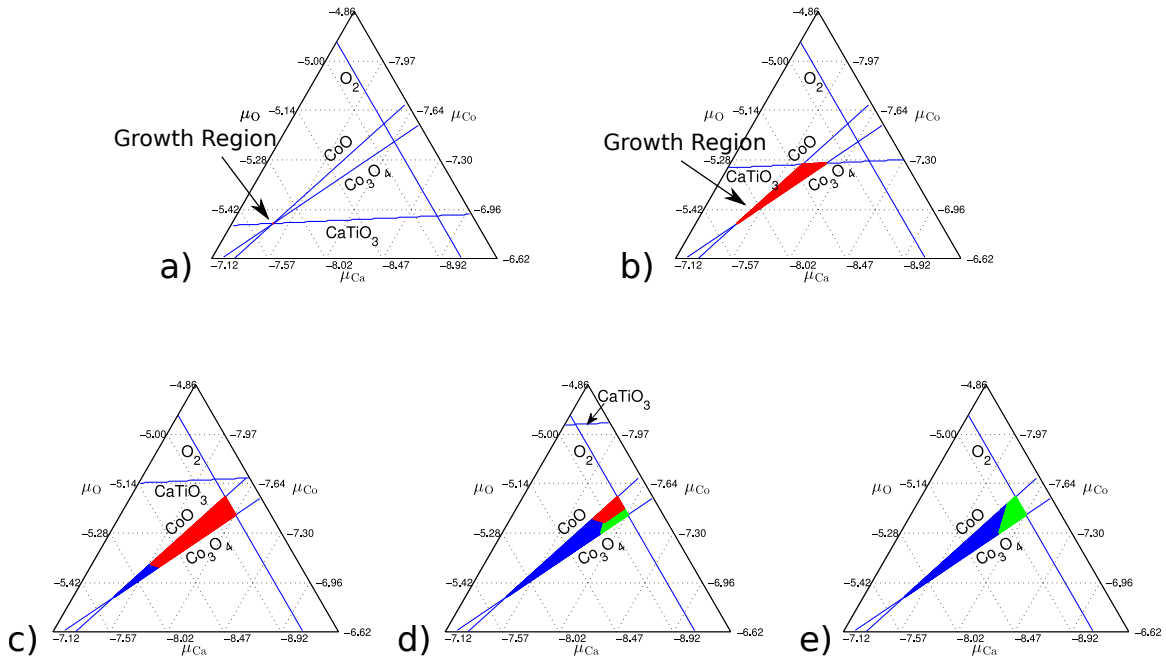

Figure 17: This is the phase diagram at a) $\mu_{\mathrm{Ti,max}}$, b) $\mu_{\mathrm{Ti,max}}$-0.5 eV, c) $\mu_{\mathrm{Ti,max}}$-1.0 eV, d) $\mu_{\mathrm{Ti,max}}$-1.5 eV, e) $\mu_{\mathrm{Ti,max}}$-2.0 eV. The red, blue and green zones are the area where $\mathrm{Ti_{Co}}$, $\mathrm{V_O}$, $\mathrm{V_{Ca}}$ are preferred respectively.

the meantime, as μ_{Ti} decreases, the preferred defect changes from $\mathrm{Ti_{Co}}$ to $\mathrm{V_O}$. But in some Ca-poor O-rich area $\mathrm{V_{Ca}}$ becomes favored.

To have a more specific comparison, the formation energies of different defects in a Ti-rich situation (intersection in Figure 17 a) and a Ti-poor situation (the points of the growth region in Figure 17 e) have been shown in Table III. For the Ti-poor situation, the data is calculated from the point with the least difference in energy between most preferred phase and least preferred phase in the $\mathrm{V_O}$ dominated area.

When Ti concentration is low, $\mathrm{V_O}$ in RS is the most favored one and dominates the major portion of the growth region, which implies that $\mathrm{V_O}$ is the intrinsic defect of CCO. In the

TABLE III: The formation energies (eV) of different defects in 5/3 Ti-doped CCO in the Ti-rich and Ti-poor situation.

Defects	E_{form} for Ti-rich	E_{form} for Ti-poor
Ti_{Co} in RS	0.09	1.54
Ti_{Co} in CoO_2 layer	0.22	1.67
V_O in RS	0.73	1.12
V_{Ca}	1.60	1.12
V_O in CoO_2 layer	2.05	2.43
Ti_{Ca}	2.07	3.58

Ti-rich region (with μ_{Ti} achieving its maximum value), the computed formation energies with a 5/3 unit cell (averaged over all possible locations) are 0.09, 0.22, and 2.07 eV for Ti_{Co} (RS layer), Ti_{Co} (CoO_2 layer) and Ti_{Ca}, respectively (78). This shows a strong preference of Ti atoms substituting for Co, rather than Ca atoms. This also shows a somewhat significant (by 0.13 eV) preference for Ti substituting Co atoms in the RS subsystem, rather than the CoO_2 subsystem, in agreement with my findings based on the EELS analysis.

I also computed the formation energies of Ti defects using a 3/2 unit cell of CCO. In this case, the averaged formation energies for Ti_{Co} (RS layer), Ti_{Co} (CoO_2 layer), and Ti_{Ca} are -0.06, 0.60, and 1.91 eV respectively, which indicates an even stronger preference (by 0.66 eV) for Ti to substitute a Co atom in the RS subsystem. In my calculations, Ti defects were simulated by substituting one atom (Co or Ca) at a time in the pristine unit cell. The compositions of Ti-doped (at a Co site) unit cells are, therefore, $Ca_{12}Co_{15}TiO_{38}$ and $Ca_8Co_9TiO_{24}$ for the 5/3 and 3/2 unit cells, respectively. The differences in the formation energies are most likely due to

the different doping rates and the different in-plane strain between the two misfit subsystems. Irrespective of the structural models, my results show that 1) Ti dopants tend to substitute Co atoms rather than Ca atoms, and 2) Ti dopants are more likely to replace Co atoms in the RS rather than the CoO_2 subsystem.

4.4 Electronic properties of Ti-doped CCO

The Seebeck coefficient of the Ti-doped thin-film CCO was measured to be $S = 135\ \mu V/K$ at room temperature. Therefore, I find no significant enhancement of S compared to pristine bulk CCO ($S \approx 130\ \mu V/K$) within the experimental uncertainty of the transport measurement (71). In order to explain this phenomenon and examine electronic properties of Ti-doped CCO, I compare the near-edge fine-structures of the Ti L-, Co L- and O K-edges with the corresponding density of states (DOS) from my DFT calculations.

To study the valence state of Ti, the fine-structure of the Ti L-edge was analysed. Figure 18 shows the near-edge fine-structure of the Ti L-edge in Ti-doped CCO, representing the excitation of $2p$ electrons into the unoccupied $3d$ orbitals. The spin-orbit interaction breaks the degeneracy of the energy levels in initial $2p$ states, which introduces an energy split as seen in the two distinct L_2 and L_3 white lines of the Ti L-edge. More specifically, the two white lines are the transition from the split 2p states ($2p_{3/2}$ (L_3) and $2p_{1/2}$ (L_2)) to 3d states. According to the crystal-field theory, the $3d$ states of Ti in the TiO_6 octahedra will be spit into t_{2g} and e_g state due to the local symmetry. This causes the further splitting of the Ti L_3 and L_2 peaks, which is highly sensitive to the local oxidation state of Ti (79; 80).

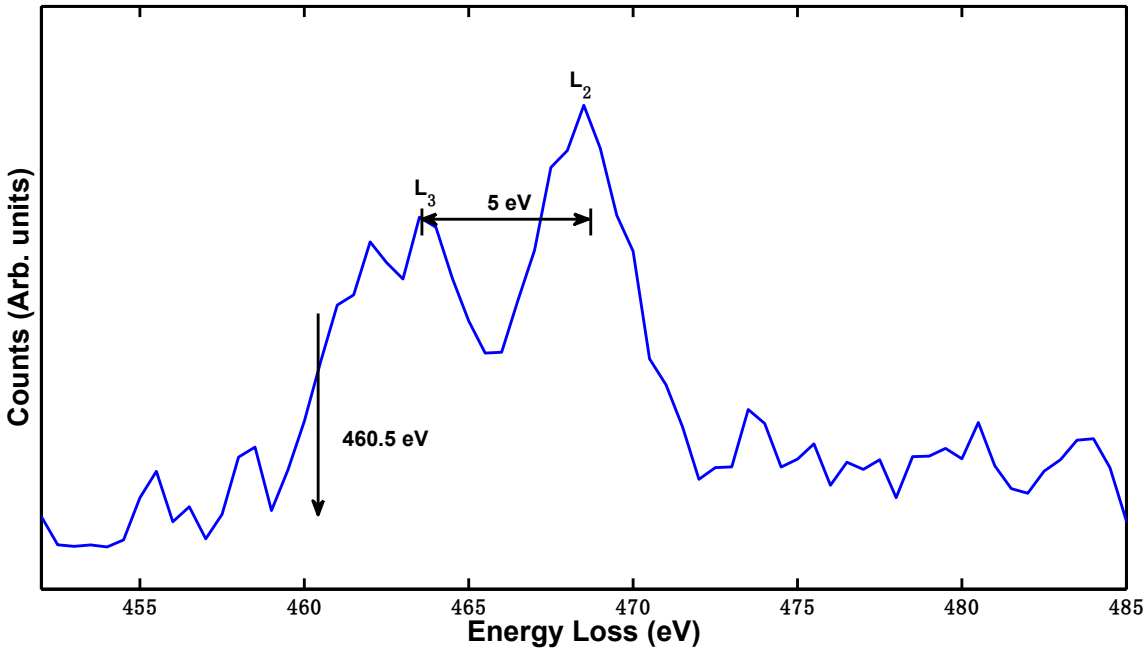

Figure 18: The EEL spectra of Ti L-edge in Ti-doped CCO. The spectra are calibrated with respect to O K-edge onset at 532 eV. The split and onset of $L_{2,3}$ edge are 5.0 eV and 460.5 eV, respectively.

In Figure 18, the Ti L-edge onset energy is found to be 460.5 eV, when the spectrum is calibrated with respect to the O K-edge onset at 532 eV. The splitting of the Ti L_3 and L_2 edges is measured as 5.0 eV. Using the previously published relationship between the Ti L-edge and the Ti valence state (81), I find that Ti is in a 4+ valence state in the doped CCO thin films. More specifically, the measured Ti L-edge onset and L_3-L_2 splitting are very close to the corresponding values of 459.5 eV and 4.8 eV, respectively, measured by Sankararaman *et al.* (80) for Ti^{4+}.

To further study the occupancy of Ti $3d$ orbitals, I have calculated and analyzed the projected density of states (DOS). Figure 19 (a) and Figure 19 (b) show the projected DOS of Ti d-orbitals when Ti substitutes Co in the CoO_2 and the RS subsystems, respectively. In both cases, I observe that the Ti t_{2g} (d_{xy}, d_{yz}, d_{xz}) and e_g (d_{z^2}, $d_{x^2-y^2}$) orbitals are unoccupied. I note that for the case of Ti in the CoO_2 layer, the coordination of Ti with oxygen is nearly perfectly octahedral. As a result, the orbitals within the t_{2g} and e_g manifolds remain degenerate in both spin channels. However, for Ti in the RS subsystem, the TiO_6 octahedra are compressed along the c-axis, which causes splittings in the two manifolds, which is particularly noticeable for e_g orbitals, as shown in Figure 19 (b). However, in both cases, the partial DOS below the Fermi-level, which results from the covalent bonding between the O $2p$ and the Ti $3d$ orbitals, is negligible. Therefore, I find the Ti atom to be in a 4+ charge state ($t_{2g}^0 e_g^0$) for Ti substituting Co either in the RS or the CoO_2 subsystems, which agrees with the experimental findings based on the Ti L-edge analysis.

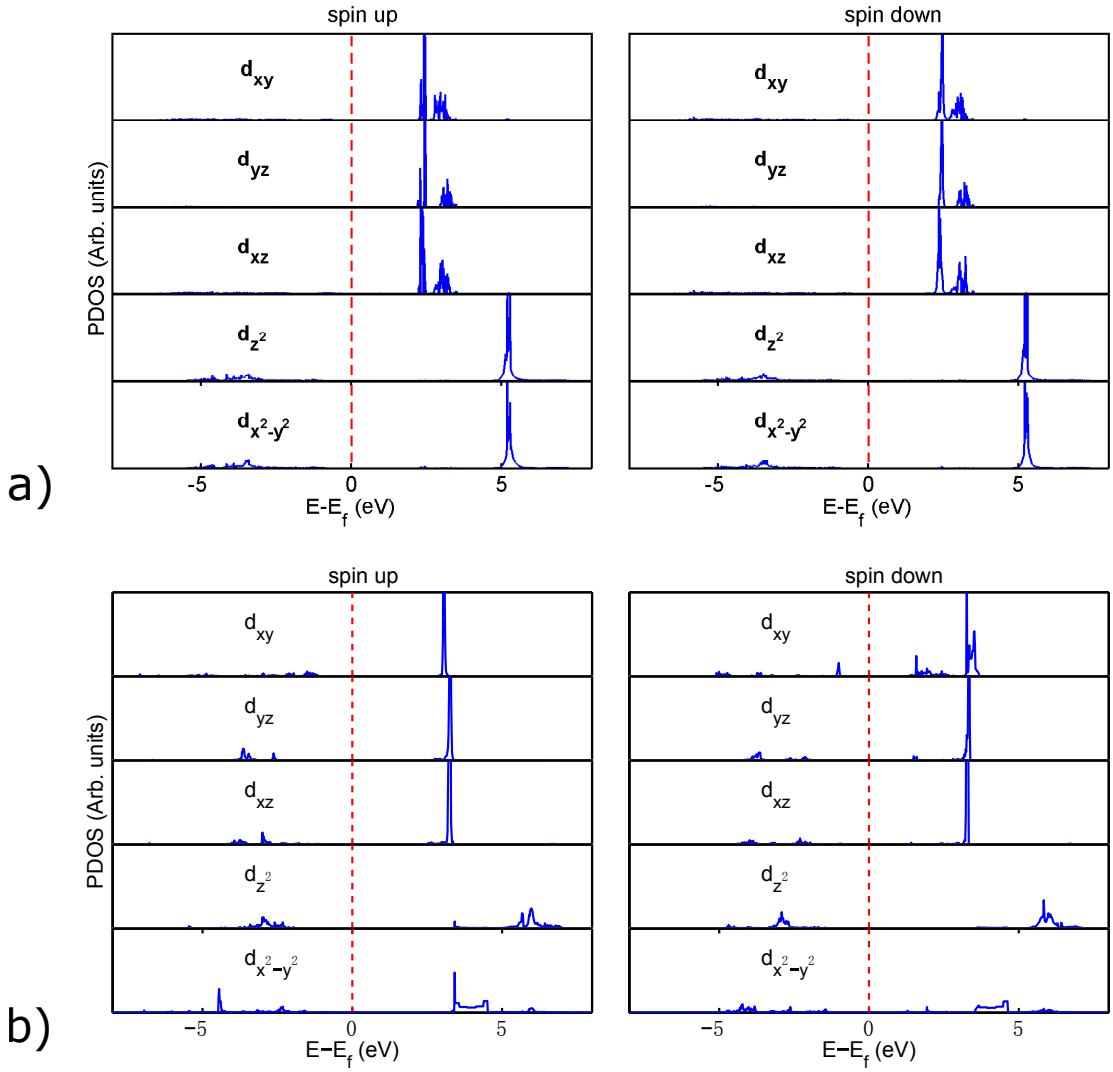

Figure 19: Partial DOS projected into angular momentum resolved d orbitals of Ti atoms when Ti substitutes a Co atom in (a) the CoO_2 layer, and (b) the RS subsystem.

Next, I study the valence state of Co upon Ti-doping. Since the Ti dopants prefer the Co site in the RS subsystem, the calculations are performed within this structure and the influences on the Co in the CoO_2 layer are explored. Figure 20 shows the projected DOS for the d-orbitals of Co in the CoO_2 layer before and after the Ti substitution of Co in the RS subsystem. The t_{2g}-e_g splitting due to the ligand field in the CoO_6 octahedra is clearly visible. While the e_g orbitals are all unoccupied, the t_{2g} orbitals are mostly occupied except for a small region of up to 0.2 eV above the Fermi level in the spin-up channel. That the t_{2g} orbitals are not fully occupied implies that Co is in a mixed valence state of Co^{3+} ($t_{2g}^6 e_g^0$) and Co^{4+} ($t_{2g}^5 e_g^0$). After Ti substitution, the ratio of unoccupied to occupied t_{2g} orbitals remains the same, which indicates that the Co valence state is not affected by the Ti substitution.

To further investigate the influence of Ti dopants on the electronic structure of Co, I analyze the change of the experimentally measured Co L-edges as a function of Ti concentration. Since Ti does not replace Ca atoms (as discussed in Sec. III), I use the Ti/Ca intensity-ratio as a measurement of the local Ti concentration. I find that even within the same sample, the Ti/Ca intensity ratio exhibits an inhomogeneity within the range of 0.067 to 0.130. Figure 21 (a) shows the EEL spectra of Co L-edges in the CoO_2 layer for two different Ti concentrations (corresponding to Ti/Ca intensity ratios of 0.067 and 0.130). The two signals are normalized with respect to a 50 eV window (830 eV to 880 eV) above the Co L_2 edge. I find that there is no difference between these two signals in terms of their edge onsets and the $L_{3,2}$ splitting, even though one spectrum is taken from a region with twice the Ti concentration. Figure 21 (b) shows the Co L_3/L_2 ratio as a function of the Ti concentration and I can clearly see that there

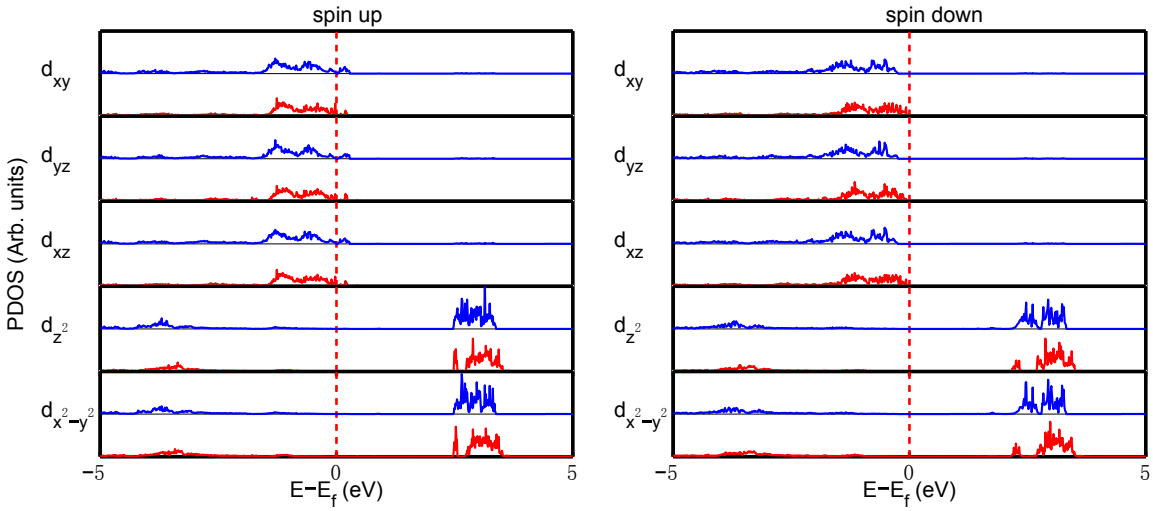

Figure 20: Partial DOS projected into angular momentum resolved d orbitals of Co (in the CoO_2 layer) before (blue curves, upper panel of each angular momentum component) and after (red curves, lower panel of each angular momentum component) the Ti substitution of a Co atom in the RS subsystem.

is no significant correlation between the Ti concentration and the Co $L_{2,3}$ ratio with almost all the measured values corresponding to a Co valence of 3.5+ (within the experimental error bars) as in pristine CCO. This is in agreement with the results from DOS analysis discussed above.

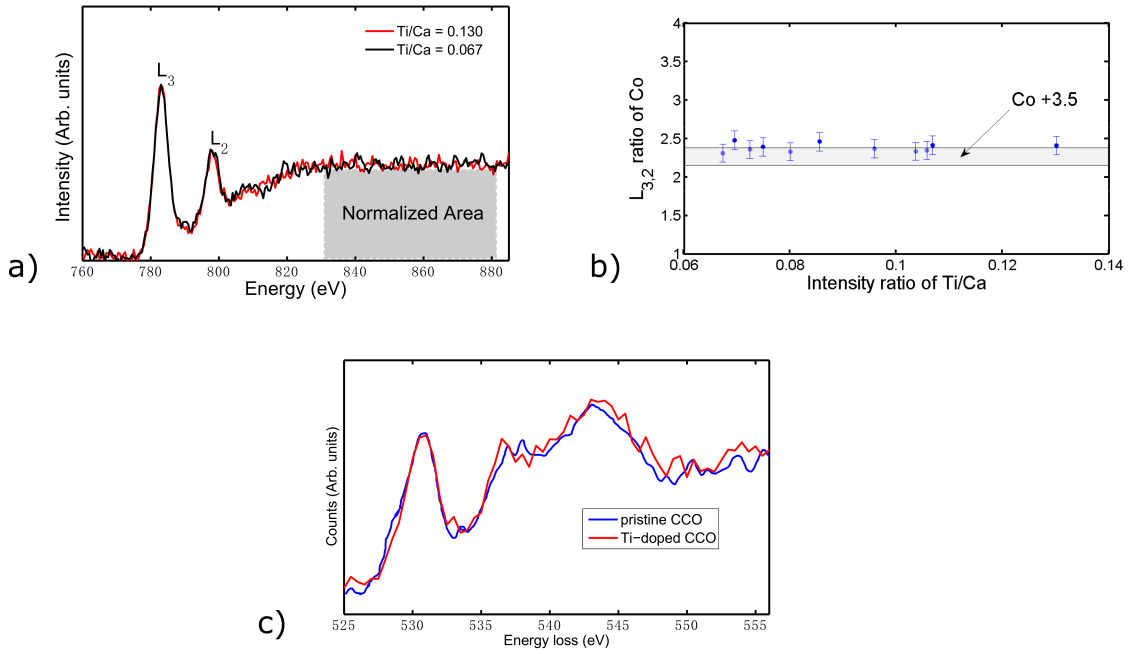

Figure 21: (a) EEL spectra of Co L-edges taken from regions with two different Ti concentrations corresponding to Ti/Ca intensity ratios of 0.067 and 0.13. (b) Co L_3/L_2 ratio as a function of the Ti concentration. The shaded grey area corresponds to a Co valence of 3.5+ with a 5% error bar. (c) EEL spectra of O K-edge of O column in the CoO_2 layer for the pristine and Ti-doped CCO.

Finally, I examine the O K-edge fine-structure. As previously shown, the O K-edge pre-peak is correlated to the hole concentration and the Co-ion spin state (82; 59). Figure 21 (c) shows the O K-edge taken from the CoO_2 layers for the pristine and Ti-doped CCO. Within the experimental error bars, I do not observe a systematic change in the O K-edge fine-structure,

either, which further confirms that the Co valence and spin-states remain unchanged after Ti-doping.

4.5 Discussion and Summary

In this chapter, I have examined the structural, electronic and transport properties of Ti-doped CCO thin films using a combination of first-principles modeling and atomic-resolution scanning transmission electron microscopy. From both Z-contrast imaging and structural optimization studies, I do not find any appreciable change in the crystal and local atomic structures upon Ti doping. The EEL spectra of Ti, Ca and Co L-edge distributions strongly suggest that Ti replaces Co in the RS sub-system. This experimental result is confirmed by my first-principles calculations, which find the lowest formation energy for Ti_{Co}-type defects when Ti substitutes the Co atoms in the RS layers. Furthermore, from an analysis of the site-projected partial density of states, as well as the EELS fine-structure studies, I find the Co and Ti valence states to be +3.5 and +4, respectively. This implies that there is no change in the Co valence state, the Co-ion spin state, or the overall charge carrier concentration in the p-type CoO_2-layers compared to pristine CCO. All of these results are consistent with the finding of no enhancement in the Seebeck coefficient for Ti-doped CCO samples in comparison to pristine CCO.

While the preferential location of Ti dopants (in the RS sub-system), as predicted by my first-principles calculations, agrees with the earlier experimental results by Xu *et al.* (71), the measured Seebeck coefficient of 135 $\mu V/K$ is significantly lower than the value of 175 $\mu V/K$ reported in that study. On the other hand, the measured Seebeck coefficient is consistent with the values measured by Torres *et al.* (70), who found no enhancement in the Seebeck coefficient

for Ti-doping concentrations of up to $x = 0.07$ in $Ca_3Co_{4-x}Ti_xO_9$. In my studies, the Ti doping concentrations was fixed at $x = 0.2$ (experiments) and $x = 0.25$ (calculations). It is perhaps possible that relatively higher doping concentrations (i.e. $x \geq 0.3$) may influence the Seebeck coefficient as suggested by Xu *et al.*, and this study cannot rule out this effect. Therefore, higher doping concentration studies in thin films are needed to develop a more comprehensive understanding of the Ti doping effects on the transport properties of CCO.

In this work, I have systematically examined the atomic scale structural and electronic properties of Ti-doped CCO to explain the unchanged macroscale Seebeck coefficient upon Ti doping. However, the direct observation of the dopant effects on the Seebeck coefficients is missing. The in-situ measurements of thermal properties are needed to explore the local defect effects. In the next chapter, I will present one possible approach for in-situ nanoscale thermal characterization.

CHAPTER 5

THERMAL EXPANSION OF 2D MATERIALS

Parts of this chapter were previously published as X. Hu, P. Yasaei, J. Jokisaari, S. Öğüt, A. Salehi-Khojin, and R. F. Klie, "Mapping thermal expansion coefficients in free-standing 2D materials at the nanometer scale", Phys. Rev. Lett. 120, 055902 (2018).

5.1 Introduction

Transition metal dichalcogenides (TMDs), graphene and other two-dimensional (2D) materials, present a great potential for different innovative applications, such as photovoltaics, transistors, and spintronics (83; 84; 85; 86). The combination of graphene with semiconducting 2D TMDs has the potential to revolutionize the field of high power/high frequency electronics, leading to novel nanometer-scale devices (83; 85; 87; 84; 88; 89; 86; 90; 91). However, thermal management in such devices will be crucial, due to the reduced dimensionality and high density of the devices in tightly packed structures (92; 93; 94; 95; 96). While the miniaturization offers remarkable improvements in electrical performance, heat dissipation and thermal expansion mismatch can be a problem in designing electronic devices based on two-dimensional materials. It was previously suggested that the presence of grain boundaries and heterointerfaces has a significant impact on the overall thermal transport properties and thermal expansion of devices based on 2D materials (97). Therefore, a better understanding of the limits set by heat dissipation and thermal expansion through grain boundaries and interfaces must be developed. One

fundamental obstacle to be overcome is the lack of spatial resolution in common temperature measurements.

As I mentioned in Chapter 1, the nanoscale thermometry employs in three types of approaches: 1, contact-based scanning probe methods; 2, non-contact optical techniques; and 3, non-contact electron microscopy methods. Among these, electron microscopy methods have the potential for thermal characterization with extremely high spatial resolution. In this chapter, I utilize non-contact thermometry beyond the optical diffraction limit using a combination of scanning transmission electron microscopy and electron energy-loss spectroscopy (STEM/EELS) and first-principles modeling to map the local temperature and thermal expansion coefficient of 2D materials. More specifically, I develop an approach, based on the temperature-dependent plasmon energy shift in 2D materials, which is related to the thermal lattice expansion (98; 99; 100; 101).

In 2D materials, such as graphene or TMDs, quantum confinement and surface plasmon effects dominate the energy shift of the plasmon peaks (102; 103; 104), making this approach more universal for atomically thin structures, including metallic (105) and semiconductor materials. I will demonstrate that the spatial resolution of my approach is approximately 2 nm and mostly limited by the localization of phonon scattering and stability of the sample under electron exposure. My method provides the potential of in-situ nanoscale characterization for other thermal properties and sets the framework of the direct nanoscale thermal characterization technology.

5.2 Methods

5.2.1 Experimental Methods

Liquid exfoliation technique was employed to prepare the nanoflake dispersions. For the TMDs (MoS_2, WS_2, $MoSe_2$, and WSe_2), 5 mg of commercial powder (Alfa Aesar) were dispersed in 20 ml of isopropyl alcohol (IPA) and sonicated for 30 hours with a sonication probe. Following sonication, the solutions were centrifuged at 2,000 rpm for 60 minutes and the supernatants were collected. For graphene, I used a similar approach as in the paper by Hernandez *et al.* (106) in which N-Methyl-2-Pyrrolidone (NMP) is used as the exfoliation solvent. In these samples, 2 mg of graphite flakes (Sigma Aldrich) was dispersed in 20 ml of NMP and bath sonicated for 30 minutes. The resulting solution was centrifuged for 90 minutes at 500 rpm and the supernatant was collected. To avoid solvent residue in the subsequent graphene TEM samples, the solution was vacuum filtered on a PTFE membrane of 0.1 μm pore size and thoroughly rinsed with ethanol, water, and IPA. The filter membrane was then immediately washed in 20 ml of fresh IPA and sonicated to re-disperse the flakes.

Following solution preparation, the dispersed nanoflakes were dropped cast on holey carbon films supported by 200 mesh copper grids (Electron Microscopy Sciences) and dried for 5 minutes under an infrared lamp. The grids were then annealed in vacuum under argon at 350 °C for 4 hours to remove any solvent residues. For graphene samples, 5% hydrogen in argon was also introduced during the annealing step. The samples were then kept in a vacuum desiccator until loaded into the microscope.

The TEM samples were characterized using an aberration-corrected JEOL JEM-ARM200CF equipped with a cold FEG and a Gatan Enfina EEL spectrometer. The accelerating voltage and emission current were set to 80 kV and 5 μA for both imaging and EELS to reduce beam induced damage and contamination. A 28 mrad convergence semi-angle was used for STEM and EELS. The HAADF images were recorded with detector angles ranging from 68 to 280 mrad. The EEL spectra were acquired with a dispersion of 0.05 eV per channel in the low-loss area. All the low-loss EELS have been performed on nanoflakes suspended over vacuum to exclude the effect of carbon films.

Before loading the sample into the microscope, the heating holder (Gatan Model 652 Double Tilt Heating Stage) was annealed at 373 K in vacuum for 2 hours to remove any contamination. For each in-situ heating experiment, I initially heated the sample to 723 K and then lowered the temperature by 50 K each time to record the data until 373 K was reached. At each sampled temperature, I waited for half an hour (one hour for 723 K) or until no obvious drift was observed before the data acquisition.

5.2.2 Computational Methods

Based on Equation 2.5, the energy dependence of the inelastic scattering is proportional to the energy-loss function, $\mathrm{lm}[-1/\varepsilon(q,E)]$. To simulate the low-loss EELS signals, the frequency dependent dielectric functions were calculated using the Vienna Ab-initio Simulation Package, including local field effects in the random-phase approximation (RPA). For a sufficiently accurate simulation, I chose large plane wave cutoff energies: 750 eV for graphene and graphite and 600 eV for TMDs. For the smearing method, the tetrahedron method with Blochl corrections

were selected. Monkhorst-Pack k-point meshes were chosen as 21×21×1 for the 2D materials (one in-plane unit) and 21×21×7 for the bulk materials (one unit cell). The vacuum in the out-of-plane direction for 2D materials was set as 30 Å. In the RPA calculations, in order to have a sufficient description of the unoccupied states, the total number of bands was selected as double the number of occupied bands.

5.3 Nanoscale Temperature Measurements

Five different free-standing 2D materials including graphene, MoS_2, $MoSe_2$, WS_2, and WSe_2 were prepared for transmission electron microscopy analysis using liquid phase exfoliation and drop casting on a holey-carbon film coated Cu mesh. Low-loss EEL spectra were collected for each material at 8 different sample temperatures, between T=373 K and 723 K in 50 K increments using a Gatan in-situ heating holder. All spectra were calibrated using the zero-loss peak, and the low-loss intensity was normalized with respect to a 40-60 eV energy-loss window, so that the normalization is not affected by the plasmon peak. The shift in plasmon energy as a function of the temperature was then measured for each material, thus providing a direct means of calibrating the temperature for each of the different materials and allowing the temperature to be mapped.

To demonstrate the temperature dependency of plasmon peak shift, the typical low-loss EEL spectra from a monolayer of WSe_2 are shown in Figure 22A for several temperatures. Since the peak is relatively broad, simply reading the peak maximum from the shown plots is not sufficiently accurate. Using a fitting function for the plasmon peaks, however, improves the accuracy by nearly an order of magnitude. A two-Lorentzian fit is necessary for these

thin 2D materials, as the signal associated with two different plasmons appears to overlap given the energy-resolution of the cold-field emission microscope. For WSe_2, the energy shift is determined to be dE/dT=-2.7 meV/K: a shift towards lower energy occurs as the temperature increases from 373 K to 723 K. This shift follows an approximately linear relationship between the plasmon energy and temperature (Figure 22B). Similar measurements were also carried out for several other TMDs and graphene.

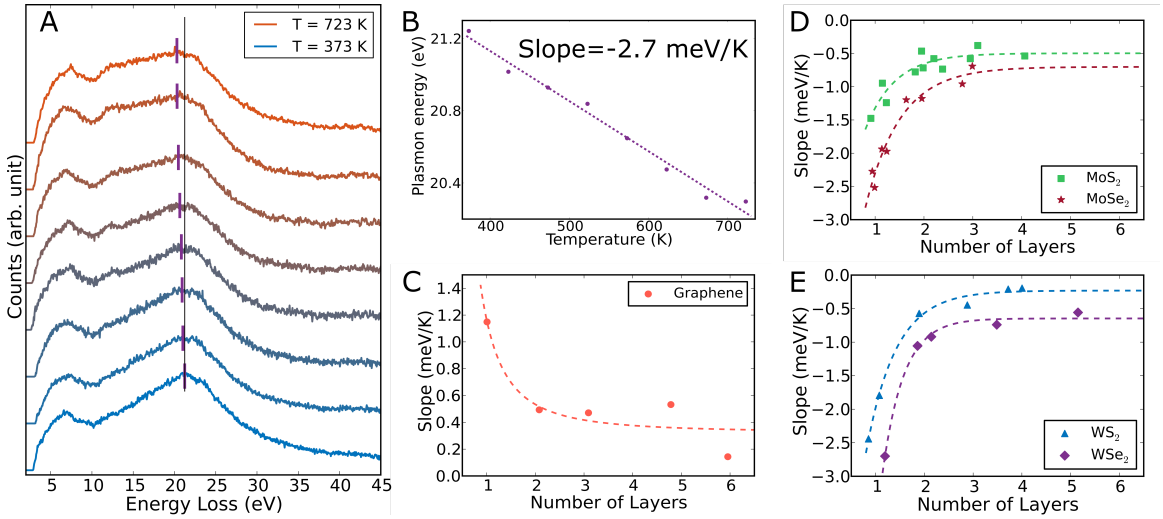

Figure 22: A) Low-loss EELS spectra from a monolayer of WSe_2 for temperatures between 373 K and 723 K. The purple lines indicate the plasmon peak centers for each temperature, determined by fitting two Lorentzian curves to the peak. The black line shows the plasmon peak center at a temperature of 373 K for comparison. B) The plasmon energy for each spectrum from (A) as a function of the temperature. C-E) The energy shifts (dE/dT) as a function of the number of layers of graphene, MoS_2, $MoSe_2$, WS_2, and WSe_2, respectively.

For each material, the effects of layer thickness were also considered ranging from monolayer to a few layers thick. It is interesting to note that the thickness, more specifically the number of layers, was found to also influence the plasmon peak shift, and this effect needs to be accounted for in order to extract the temperature signal. The rate of plasmon energy change as a function

of temperature (dE/dT) for free standing graphene and TMDs as a function of thickness is presented in Figure 22C-E. Results indicate that graphene exhibits a positive energy shift compared to TMDs. Moreover, in TMDs containing Se, the plasmon energy shifts appear to be higher for all thicknesses compared to the corresponding TMD containing S. In all cases, the energy shift decreases as the number of layers increases, following an inverse square dependence. This thickness dependence seems to disappear for more than 3-4 layers. The inverse square dependence of the energy shift on thickness can be attributed to quantum confinement effects that become more pronounced as the thickness decreases (102; 103). Therefore, for materials that are 1-3 layers thick, we need to distinguish the energy shift of the plasmon peak due to changes in temperature from effects due to different sample thickness. This is achieved by measuring the temperature dependence of the plasmon energy shift separately for various 2D material thicknesses and applying the appropriate calibration measurement to map the temperature in area of known thickness.

In order to accurately measure the thickness of the nanoflakes in units of number of layers, the ratio of the inelastically scattered over the transmitted electrons was determined using the low-loss EELS log-ratio method. Figure 23A shows a sample of the WS_2 nanoflake. It consists of several regions of different thickness, with several broad flat areas of a particular number of layers (I-V), suspended over vacuum. The relative thicknesses of the different regions are calculated by applying the log-ratio method and the calculated thickness values are presented as a scatter plot with multiple Gaussian fits in Figure 23B. Five distinct peaks could be fit, with an almost equal separation between peaks. The relative intensity ratios for the peak centers

(nearly 2:3:4:5:6) are used to determine the thickness of each area (i.e. number of layers). A linear relationship, Figure 23C, between the relative ratios and the peak centers with a y-intercept near zero, shows that for each of the five areas (I-V) the thicknesses are 2-6 layers. This compares well with the more common method of determining the number of layers in a 2D material based on the step-wise increase in the HAADF intensity (104). In this work, layer thicknesses in units of numbers of layers were all calculated through the procedure outlined above. With the thickness known, it is then possible to use the plasmon peak shift to map the temperature within each region of the sample.

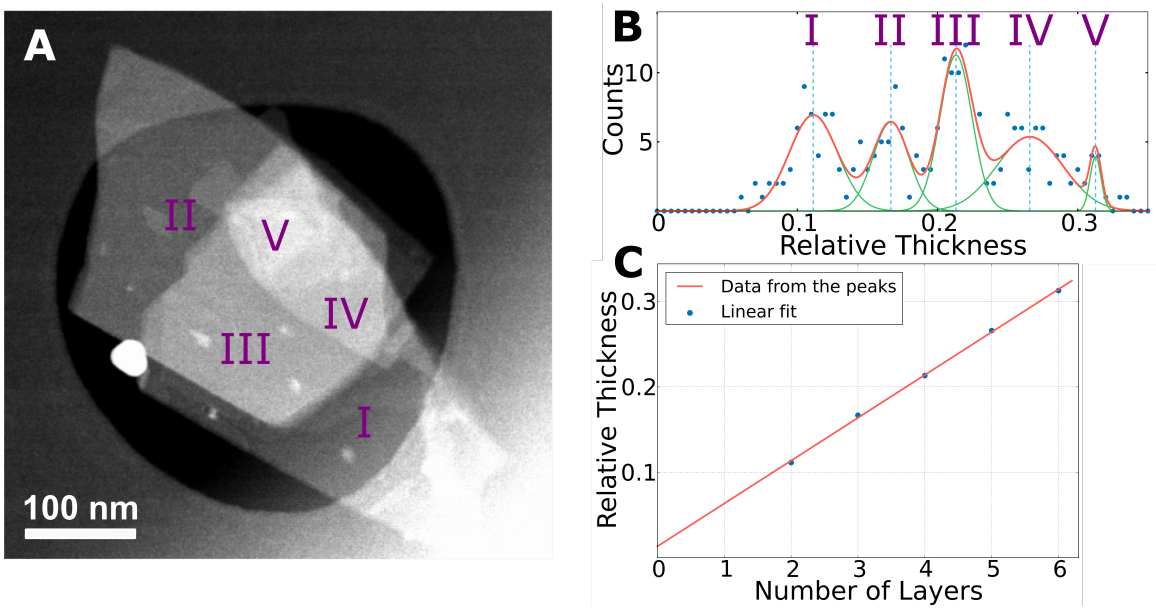

Figure 23: A) Z-contrast image of several freestanding WS_2 nanoflakes. The thickness varies from two layers up to six layers thick. B) A plot of the thickness from the flakes in the hole showing the fit curves for each location. C) A linear fit of the peak centers to number of layers.

Using the thickness dependent plasmon energy shifts, I determined the temperature distribution with nanometer-scale resolution in a $MoSe_2$ nanoflake, shown in the high-angle annular

dark field (HAADF) image in Figure 24A, and the correlated plasmon-energy shift with the corresponding temperature map (shown in Figure 24B). This temperature map was created using the low-loss EELS signals acquired over the entire $MoSe_2$ flake, consisting of areas with different sample thickness labeled as I, II, III that are 1,2, and 3 layers thick, respectively. Using the calibrations shown in Figure 22D-F to account for the variation in thickness, a temperature map was produced for a $MoSe_2$ nanoflake at a setpoint temperature of 573 K. The overlay of the HAADF image and the temperature map (Figure 24C) shows that, for the regions (I, II, III) corresponding to a uniform sample thickness, I measured a temperature of approximately 586K using the plasmon energy shift. Histograms showing the variation in temperature measured in each flat area are shown in Figure 24D. The temperature distributions are almost Gaussian and by fitting a Gaussian function to the distribution, a mean temperature was calculated for each region. The error is expressed as the percentage difference from the holder temperature set point (573 K). The measurements for area (I, II, III) are 592K (3.3%), 591K (3.1%), and 576K (0.5%), respectively. One source of error in my measurements is related to finding the center of the plasmon peak, which accounts for an uncertainty of $\pm$22 meV. The 22 meV peak position uncertainty is small compared to peak shift of 270 meV per 100 K temperature difference in WSe_2, and corresponds to a temperature uncertainty of 8 K. For mapping the edges of the 2D layers, there is an additional error source due to changes in the plasmon peak shape due to edge effects (107). This effect is clearly visible in the temperature map, where the edges of the 2D layers appear cooler than the rest of the layer. However, the overall consistency and accuracy demonstrated in the measured temperature is well within the error of the sample

holder temperature setpoint, clearly demonstrating that my technique is capable of mapping the temperature distribution at the nanoscale in 2D materials.

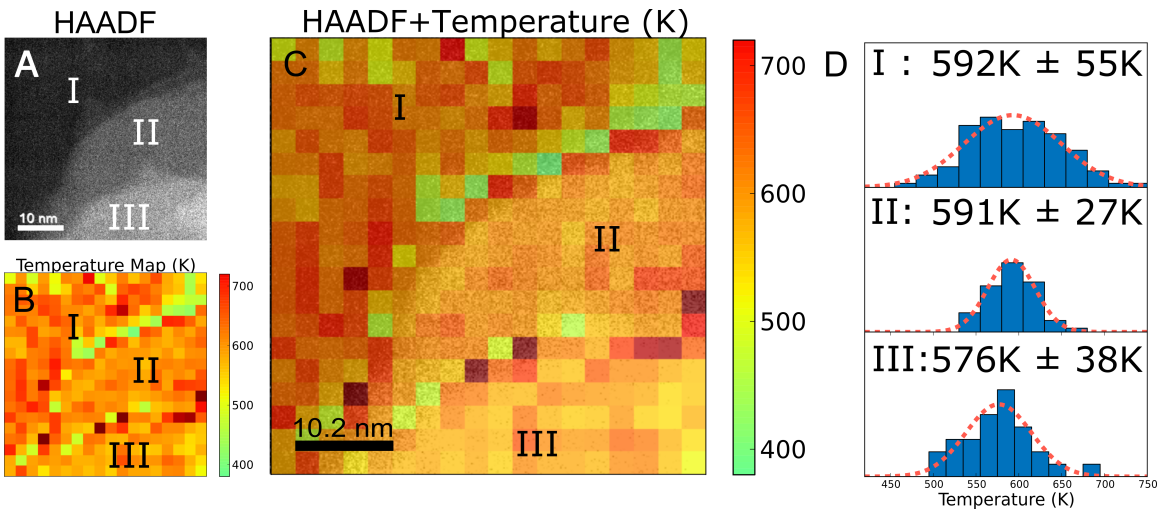

Figure 24: A) HAADF image of a $MoSe_2$ nanoflake. B) Corresponding temperature map of $MoSe_2$ at a nominal sample temperature of 573 K. C) The overlayed image of A) and B) showing three zones defined by the different thickness (I, II, III). D) The temperature distribution for each area.

5.4 Mechanisms

Thus far, the temperature measurements have been presented empirically, using a calibration curve of the plasmon energy shift as a function of temperature (dE/dT). Next, I will show that the rate of this change is related to the lattice strain and the thermal expansion coefficient (TEC) of the material. This relationship is thickness-dependent due to the quantum confinement effects and underpins the temperature measurements.

To explore the temperature dependence of plasmon energy, I start with the analysis of an observable experimental variable, the normalized energy shift:

$$
\begin{aligned}
R &= \frac{1}{E_0}\frac{dE_p}{dT} && (5.1)\\
&= \frac{1}{E_0}\frac{\partial E_p}{\partial a}\frac{\partial a}{\partial T} + \frac{1}{E_0}\frac{\partial E_p}{\partial c}\frac{\partial c}{\partial T} && (5.2)\\
&= \frac{a_0}{E_0}\frac{\partial E_p}{\partial a}\alpha_a + \frac{c_0}{E_0}\frac{\partial E_p}{\partial c}\alpha_c && (5.3)\\
&= -\gamma_a\alpha_a - \gamma_c\alpha_c && (5.4)
\end{aligned}
$$

where E_p is the plasmon energy (assigned as E_0 at temperature T_0), a_0, c_0 are the in-plane and out-of-plane lattice constants of the system at temperature T_0, and α_a, α_c are the in-plane and out-of-plane thermal expansion coefficients. In addition, I define new parameters to describe the energy change of the collective electron oscillations (plasmon) due to the lattice expansion, $\gamma_a = -\frac{a}{E_p}\frac{\partial E_p}{\partial a}$ and $\gamma_c = -\frac{c_0}{E_p}\frac{\partial E_p}{\partial c}$ (similar to Grüneisen parameters for the case of lattice vibrations). They present the decreasing (increasing) rate of plasmon energy with increasing (decreasing) lattice constant. Therefore, the plasmon energy shift from the thermal contribution can be divided into two steps: 1, the plasmon energy shift due to lattice expansion (γ) and 2, the lattice expansion due to temperature elevation (α).

To relate the plasmon energy with lattice volume (γ), let us first consider the free electron model, where the plasmon energy can be expressed as

$$E_p(T) = \hbar\sqrt{\frac{n(T)e^2}{\varepsilon_0 m}}. \quad (5.5)$$

Here m and e are the mass and charge of an electron. The temperature dependence of the electron density $n(T)$ is due to the temperature dependence of the unit cell volume $V(T)$ of the valence electron cloud $n(T) = \frac{n_0}{V(T)}$, where n_0 is the number of valence electrons in the unit cell. For a crystal of tetragonal or hexagonal symmetry, the number density of valence electrons can be expressed as

$$n(T) = \frac{n_0}{V(T)} = n_0(\frac{\sqrt{3}}{2}a(T)^2c(T))^{-1}, \tag{5.6}$$

where the unit cell volume $V(T) = \frac{\sqrt{3}}{2}a(T)^2c(T)$, and $a(T)$, $c(T)$ are the lattice constants of the system at temperature T.

Combining Equation 5.5 with Equation 5.6, the plasmon energy can be presented as:

$$E_p(T) = \hbar\sqrt{\frac{n_0e^2}{\frac{\sqrt{3}}{2}\varepsilon_0 m}}a(T)^{-1}c(T)^{-\frac{1}{2}} \tag{5.7}$$

Assuming the lattice expansions from in-plane and out-of-plane directions are independent to each other ($\partial c/\partial a = 0$), the derivative of the plasmon energy can be written as:

$$\frac{dE_p}{E_p} = -\frac{da}{a} - \frac{1}{2}\frac{dc}{c} \tag{5.8}$$

Equation 5.8 shows that the free-electron predictions for γ are, $\gamma_a = 1$ and $\gamma_c = 1/2$. While this model can explain the temperature dependence of plasmon energy for bulk materials, the confinement in the out-of-plane direction of the electrons in 2D materials presents problems, as will be shown with more accurate calculations next.

To explore the relation between the plasmon energy shift and the lattice expansion including confinement effects, in a more quantitative way, one can calculate the parameter γ from simulations of the low-loss EEL spectra as a function of the lattice parameters. I, therefore, applied the random phase approximation (RPA) (108), which is a well-known approach for the calculation of frequency-dependent dielectric function, $\varepsilon(\omega)$, to determine the plasmon loss curves and the subsequent energy shifts. Low-loss EELS of graphene and TMDs were calculated for 10 different in-plane lattice constants, $a/a_0 = 0.97 - 1.04$, which correspond to the in-plane lattice parameters at different sample temperatures. For bulk materials, I also performed calculations with different out-of-plane (c) lattice parameters, and their corresponding plasmon energy shifts were determined by extrapolating the measured energy shifts shown in Figure 22C-E to the limit of infinitely large sample thickness.

An example of the calculated low-loss EEL spectra for graphene is shown in Figure 25A. The plasmon energy shift as a function of the lattice expansion is plotted in Figure 25B. A linear relationship between the plasmon energies and lattice constants is observed, which results in a constant $\gamma_a = -\frac{a}{E_p}\frac{\partial E_p}{\partial a}$. The γ_a for different 2D systems are then calculated and shown in Figure 25C. The γ_a tends to approach 1, which is the value predicted by the free electron model, as the thickness increases from monolayer to the bulk system. However, for monolayer or few-layer systems, γ deviates significantly from 1. For graphene, I find $\gamma_a > 1$, while for 2D TMDs, $\gamma_a < 1$. These observations can be explained by reconsidering the assumption for Equation 5.8 ($\partial c/\partial a = 0$).

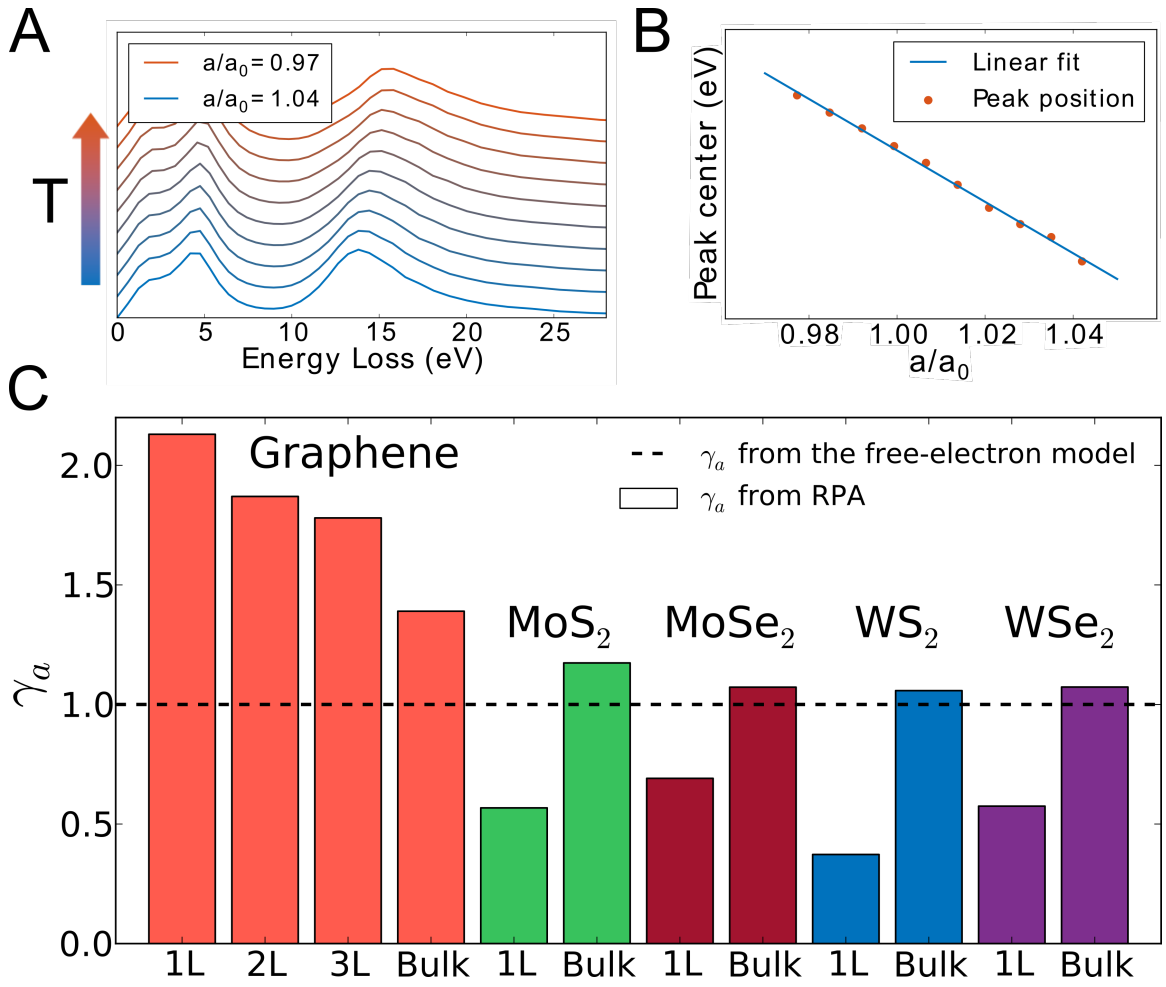

Figure 25: A) Calculated low-loss EEL spectra for single-layer graphene with different lattice constants. B) The plasmon energy for each spectrum from (A) as a function of lattice constant a. C) Calculated γ_a in thin films and bulk of graphene and TMDs. The dashed line presents the theoretical value of $\gamma_a = 1$ from the free electron model.

Next, I explore the reasons for the findings of $\gamma_a > 1$ and $\gamma_a < 1$ for graphene and 2D TMDs, respectively, by simulating the response of lattice expansion dc as a function of the lattice expansion da. For graphene, I define the effective c from the spatial extent of the charge density profile along the out-of-plane (c) direction. In particular, I choose the effective c as the distance which contains 95% of the total charge density profile along c. For MoS_2, I define c as the distance between two S layers. These two definitions are depicted in Figure 26A.

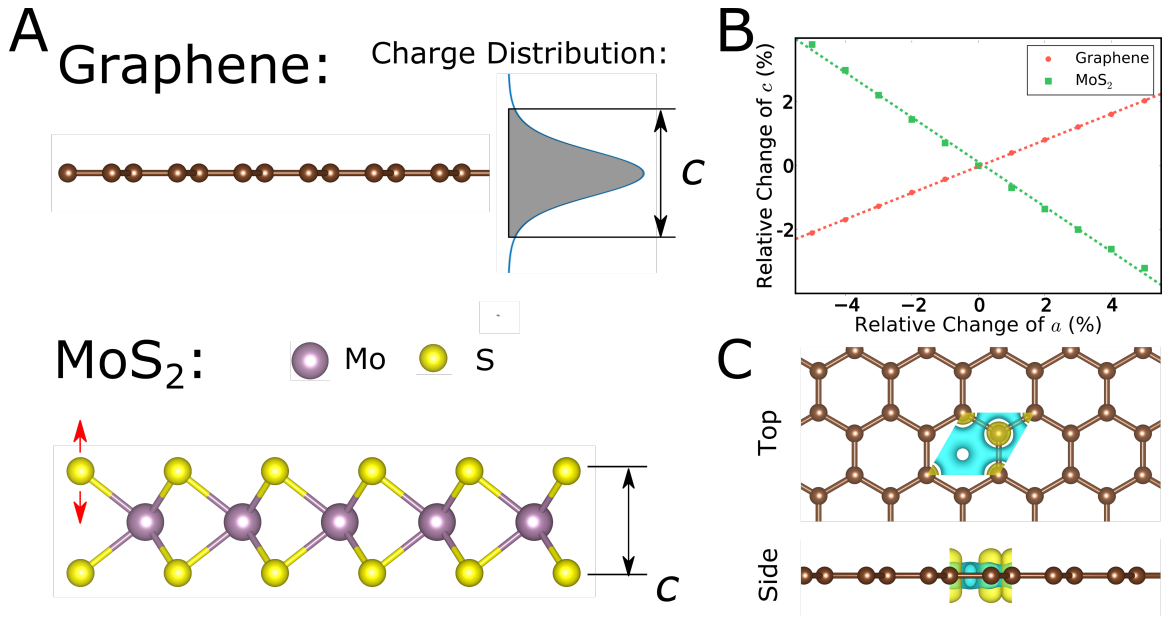

Figure 26: A) Schematic diagram of the simulations for lattice expansion and determinations of effective out-of-plane lattice constant c for graphene and MoS_2. The C, Mo, S atoms are in brown, purple, and yellow spheres, respectively. B) Relative change of the out-of-plane lattice constant c (%) in terms of relative change of the in-plane lattice constant a (%) for graphene and monolayer MoS_2. C) Charge density difference for graphene expanded from $a/a_0 = 1$ to $a/a_0 = 1.05$. Blue areas present charge loss, and yellow areas present charge accumulation

The variation of c as a function of a is simulated by the structural out-of-plane relaxation (the in-plane relaxation is frozen) for different in-plane lattice expansions (the Poisson effect).

The out-of-plane response with different in-plane lattice parameters ($a/a_0 = 0.95 - 1.05$) for graphene and monolayer MoS_2 are presented in Figure 26B. The results show that $\frac{dc}{da}$ is positive for graphene, while it is negative for monolayer MoS_2. Combining these observations with Equation 5.8 shows why $\gamma_a > 1$ for graphene (dc and da having the same sign, hence increasing γ) and $\gamma_a < 1$ for monolayer TMDs.

For graphene, the interesting finding of out-of-plane expansion when the lattice expands in the in-plane direction can be observed from the charge density contour plots. A charge difference distribution for graphene expanded from $a/a_0 = 1$ to $a/a_0 = 1.05$ is plotted from top and side views in Figure 26C. During the in-plane lattice expansion, a charge transfer from in-plane σ bonding to out-of-plane orbital is observed. The in-plane stretching weakens the in-plane bonding, but the charge transfers to the out-of-plane orbital to strengthen the π orbitals. For MoS_2, the observed Poisson effect is due to the anisotropic atomic structures (Figure 26A). The in-plane stretching lengthens the Mo-S bonding, which brings a restoring force along the Mo-S bonding. The out-of-plane component of this force pulls nearby S atoms towards Mo atoms, which induces the MoS_2 shrinking in out-of-plane direction during the in-plane lattice expansion.

5.5 Nanoscale Thermal Expansion Coefficient Measurements

With this computed relationship (γ_a, γ_c) and the experimentally measured plasmon energy shift (R), the in-plane TECs can be obtained for both thin films and bulk materials. Based on Equation 5.1, for 2D materials, neglecting thermal expansion effects in the out-of-plane direction, one can write $R = -\gamma_a \alpha_a$, which allows me to calculate the in-plane thermal expansion

coefficients from the measured R values and the computationally determined γ_a values. For bulk materials, the contribution from the out-of-plane direction cannot be neglected. Though I can still compute γ_a and γ_c from RPA calculations of the low-loss EEL spectra and use the R values extrapolated to an infinite thickness from Figure 22C-E, my procedure only gives a linear relationship between α_a and α_c. To determine α_a, I then use the experimentally measured ratio of the thermal expansion coefficients $\alpha_c/\alpha_a = \beta$ to write $\alpha_a = -\frac{R}{\gamma_a + \beta\gamma_c}$.

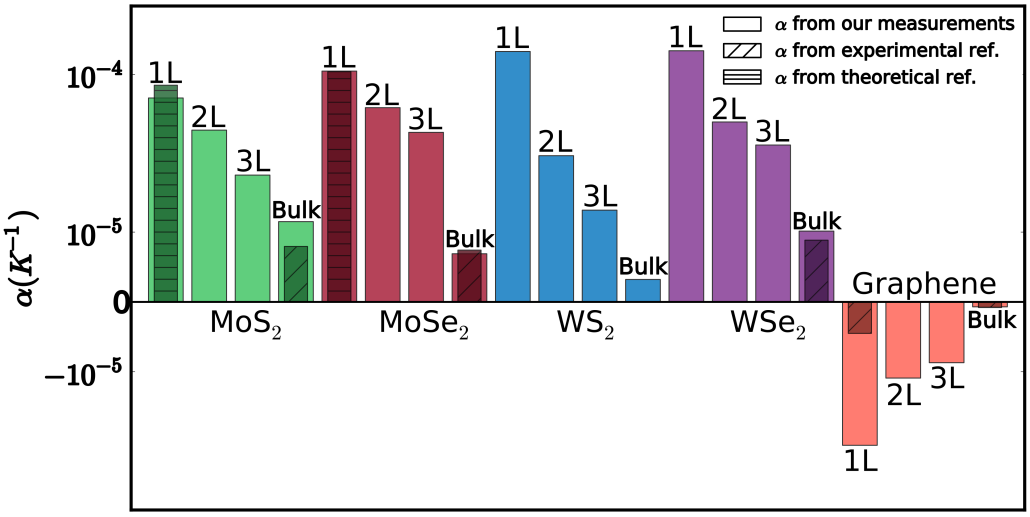

Figure 27: Measured in-plane TECs in thin films and bulk of graphene and TMDs, compared with reference data

The results for the TECs determined in this fashion are shown graphically in Figure 27. Table IV provides a complete list of TECs derived from my measurements for single-, double-, tri-layer as well as bulk materials. The error-bars in Table Table IV are computed using the

TABLE IV: Comparison of in-plane TECs (10^{-5} K^{-1}) obtained from the plasmon energy shift measurements and corresponding RPA calculations with reference (theoretical† and experimental‡) data (109; 110; 111; 112; 113; 114; 115; 116).

System	Monolayer	Bilayer	Trilayer	Bulk
MoS_2	6.49±0.75 (8.24^{a†})	3.60±0.47	1.82±0.25	1.15±0.23 (0.66^{b†}, 0.49^{c‡}-0.79^{d‡})
$MoSe_2$	10.62±0.64 (10.54^{a†})	5.44±0.35	3.46±0.28	0.69±0.10 (0.64^{b†}, 0.74^{d‡})
WS_2	15.21±1.38	2.26±0.20	1.31±0.10	0.32±0.04 (-0.15^{b†}, 0.64^{f‡})
WSe_2	15.42±0.69	4.18±0.25	2.74±0.29	1.01±0.06 (0.55^{b†}, 0.68^{e‡}-1.41^{f‡})
Graphene	-2.14±0.37 (-0.31^{g†})	-1.09±0.25	-0.87±0.17	-0.07±0.01 (-0.04^{g†}, -0.08^{h‡})

^{a} Ref. (109), ^{b} Ref. (110), ^{c} Ref. (111), ^{d} Ref. (112),
^{e} Ref. (113), ^{f} Ref. (114), ^{g} Ref. (115), ^{h} Ref. (116).

scatter in the experimental data shown in Figures Figure 22C-E. Our predicted TEC values are compared with values available in the literature (109; 110; 111; 112; 113; 114; 115; 116).

As can be seen from Table IV, my predictions for bulk materials are a close match with previously reported experimental data, especially for graphite, $MoSe_2$ and WSe_2. The consistency between the data reported here and the previously published data for bulk materials shows that the temperature dependence of the plasmon energy can be directly correlated to the thermal expansion. One important result of this study is that I was able to experimentally measure the in-plane TECs for free-standing monolayer, bilayer and trilayer TMDs. For monolayer TMDs, I found that the in-plane TECs agree well with the theoretical results (109) showing increased TEC values that are more than one order of magnitude larger compared to their bulk values. I attribute this effect to the fact that a monolayer film is unconstrained by the inter-layer interactions.

While my reported TECs for TMDs agree very well with published values, the calculated TEC value for graphene differs substantially from the reference data while still exhibiting the correct overall trend. This likely arises from the very high thermal and electrical conductivity in graphene compared to the semiconducting TMDs. In particular, the temperature in nanoflakes of graphene is correlated to the mean free path of phonons, which is orders of magnitude larger in graphene compared to TMD materials. This means that the thermal transfer between the graphene and the carbon support is much more efficient than for the TMDs, and the temperature measurement is much less local. The difference between my measurements and the reference may also come from the defects effects. A recent study reports that the TEC of graphene shows a significant dependence on the defect density. The TEC of the pure graphene in this study ($\sim -0.9 \times 10^{-5}\mathrm{K}^{-1}$) is close to my prediction of $-2.14 \pm 0.37 \times 10^{-5}\mathrm{K}^{-1}$. My high spatial resolution measurement reflects local TEC of pure and suspended graphene, while the other techniques reflect the overall average of the properties. Another factor that may influence the difference between my measurements and the reference data is substrate clamping. As the reference data are measured for graphene grown on a substrate, the TEC for free-standing graphene should be significantly larger. Therefore, my technique shows great promise for measuring local temperature using graphene layers, and at TMD/graphene interfaces in devices.

To further demonstrate the ability to map the thermal expansion coefficient of free-standing 2D materials, I acquired maps of the plasmon peak in $MoSe_2$ nano-flakes at 473 K and 623 K. The relative plasmon-peak shift as a function of position was measured and used to determine

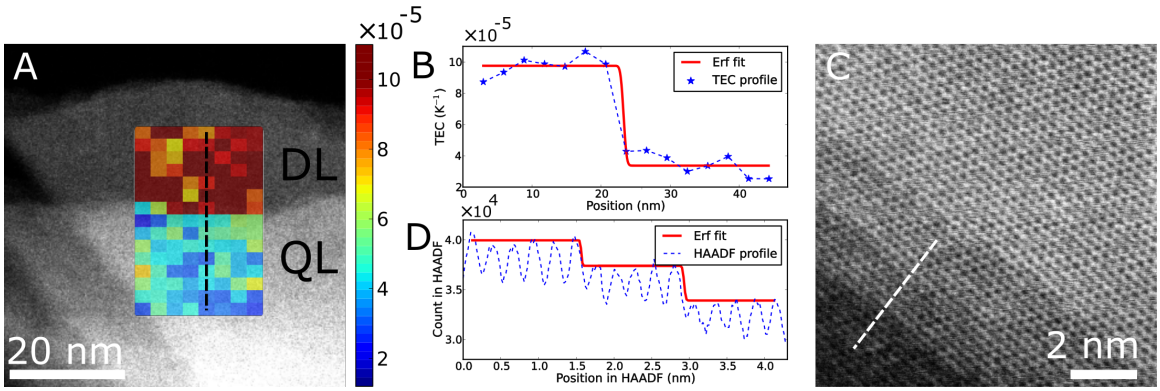

Figure 28: A) HAADF image of $MoSe_2$ at 623 K and the spatially resolved map of the local thermal expansion coefficient in the edge between double layer (DL) and 4-layer (QL) areas. B) Line profile of thermal expansion coefficient of the interface indicated by the black line in A. C) Representative atomic-resolution HAADF image of MoS_2 taken at 573 K. D) Line profile of image contrast across several layers of MoS_2 at 573 K.

the TEC using the first-principles modeling results described above. Figure 28A shows a free-standing $MoSe_2$ flake at 623 K, as well as the measured thermal expansion coefficient. The region of the $MoSe_2$ shown in Figure 28A consists of two different layers, each exhibiting a different thermal expansion coefficient ranging between 0.25 and 1.06×10^{-4} K^{-1}. It is interesting to note here that the double layer area appears to exhibit the highest thermal expansion coefficient, and appears to be confined by the edges of the individual layers. Figure 28B shows a line profile of the edge between the double and 4-layer regions in $MoSe_2$. The spatial resolution of the thermal expansion coefficient map is 2.95 nm, and is mostly limited by the pixel size of the spectrum image. Fitting a smoothed complementary error function reveals that the resolution can be as high as 2.1 nm, if smaller pixel sizes are used for mapping the plasmon peak shift.

Figure 28C shows an atomic-resolution HAADF image of a free-standing MoS_2 flake at elevated temperature (573 K) consisting of 4 distinctive layers and demonstrates that the spatial resolution for imaging (even at elevated temperatures) is better than 1 Å (Figure 28D). However, the spatial resolution limit for the thermal measurements using STEM-EELS is lower than this value, as the temperature measurements fundamentally depend on the mean free path of phonons and electrons (105). More specifically, the localization of the EELS signal for a plasmon peak at 20 eV can be determined using the equation introduced by Egerton (117):

$$d_{50} \approx \sqrt{\left(\frac{\lambda}{2\theta_E^{3/4}}\right)^2 + \left(\frac{0.6\lambda}{\beta}\right)^2} \approx 1.9nm, \tag{5.9}$$

where $\lambda = 2.51$ pm is the electron wavelength at 200 kV, $\theta_E = 0.06$ mrad is the characteristic scattering angle, and $\beta = 60$ mrad is the EELS collection angle. On the practical side, the current measurement resolution is also limited by spatial drift and the sensitivity of the 2D materials to extended electron beam exposure. Nevertheless, the spatial resolution shown in Figure 28B, is very close to the predicted theoretical limit at the given plasmon peak energy, and orders of magnitude better compared to the spatial resolution of 100 nm for optical techniques. Such a high resolution for temperature measurements is crucial for examining thermal transport in the latest sub-10 nm transistors (118), where a direct temperature measurement is only possible using the STEM-EELS method. Further improvements to the temperature resolution and accuracy can be achieved by increasing the energy resolution of the low-loss EEL spectra using, for example, a monochromated STEM instrument (112). More importantly, the

measurement rate of the technique is very high, providing the capability of capturing dynamic temperature changes. The exposure time for low-loss EELS can be as low as 10^{-3}s, with a sufficient signal/noise ratio for most thin materials. This provides a great potential for in-situ thermal experiments involving dynamic processes. Finally, it should be noted that a potential issue arises from electron beam-induced sample heating effects. However, using a thermal conductivity, κ, of around 1 $\mathrm{Wm^{-1}K^{-1}}$ for WSe_2 (119), I found a beam-induced temperature rise of only $\Delta T \approx 0.95$ mK for the electron probe conditions used. This value is significantly smaller than the temperature resolution of the EELS based measurement, and may safely be neglected.

5.6 Summary

In summary, I have presented a novel approach to nanoscale mapping of TECs in free-standing 2D materials using high-resolution STEM imaging coupled with EEL spectroscopy. The measurement utilizes the shift in the plasmon peak of the 2D material, which is related to the thermal expansion of the 2D lattice. The measured plasmon energy shift exhibits a dependence on the number of 2D layers, which is attributed to quantum confinement effects in 2D materials. Accounting for the sample thickness of the 2D material, in units of number of atomic layers, I showed that it is possible to map the local temperature with nanometer resolution. Theoretical calculations using DFT and RPA were also developed to compare the thermal expansion coefficients of 2D and bulk materials, and the results were found to be in very good agreement with existing reference data. By measurement of the TEC near surfaces, grain boundaries or heterointerfaces, I can predict and control the mismatch and thermal strain

resulting from various device operations, avoiding strain induced (thermomechanical) fracture or changes in the electronic properties. This is particularly important for 2D materials, where temperature changes can cause strains on both sides of the interface due to the thickness dependence of the TEC. Future studies examining temperature variations across hetero-interface or grain boundaries, or other low-dimensional structures such as nanowires, in-plane heterostructures, and hybrid nanostructures will be essential to further elucidate the understanding of the thermal transport properties in nano-scale devices. Controlling the thermal expansion of 2D materials is also crucial for the design of nano-scale devices. Alloying engineering is a potential approach to control the thermal expansion behavior via the tunable alloying concentration. I will discuss this possibility in the next chapter.

CHAPTER 6

THERMAL EXPANSION OF TMD ALLOYS

Monolayer TMDs exhibit extraordinary optoelectronic properties due to the change from an indirect band gap to a direct one when the thickness of materials is approaching monolayer thickness. The ability to tune the band gaps make the group of monolayer TMDs an ideal candidate for different optoelectronic applications, such as transparent flexible optoelectronics, solar cell, and interband tunnel field-effect transistors. The control of band gaps is critical to the research and applications of 2D TMDs and can be realized with a variety of methods, with alloy engineering being the most common one. Due to similar crystal structure of different TMDs, it is possible to mix two or more kinds of TMDs into an alloy system. Theoretical work confirms that certain alloyed structure is energetically stable and the alloying concentration can be continuously tuned for systems such as $Mo_{1-x}W_xSe_{1-y}S_y$. The control of band gaps through alloy engineering is widely studied in TMDs and achieved by alloying TMDs with different band gaps. TMD alloys exhibit a great potential in the optoelectronic applications.

Meanwhile, the thermal expansion mismatch problem becomes more important in such device design due to the large thermal expansion in the monolayer limit. However, the thermal expansion behavior of 2D TMD alloys is not fully understood but is needed for the electronic device design. It is of great interest to study the alloying effects on the thermal expansion behavior of TMDs, which can result in the control of the thermal expansion mismatch. Here, I utilized the nanoscale thermal expansion measurements on the TMD alloys, $Mo_{1-x}W_xS_2$.

Three different TMD alloys, $Mo_{1-x}W_xS_2$ ($x = 0.3, 0.5, 0.7$), were prepared for thermal expansion measurements using liquid phase exfoliation and drop casting on a holey-carbon film supported by a holey SiN film (Protochips thermal E-chips). Low-loss EEL spectra were collected for each material at 4 different sample temperatures, between T=423 K and 723 K in 100 K increments using a Protochips in-situ heating holder. All spectra were calibrated and normalized as the methods I mentioned in the last chapter.

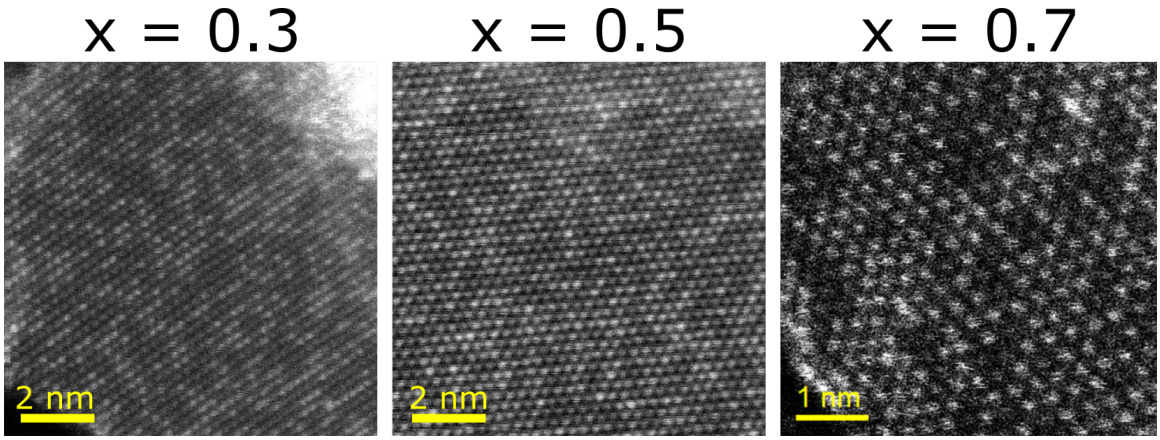

Figure 29: Atomic resolution HAADF image of TMD alloys ($Mo_{1-x}W_xS_2$) at 423 K with different alloying concentration ($x = 0.3, 0.5, 0.7$).

Figure 29 presents the atomic resolution HAADF images of TMD alloys ($Mo_{1-x}W_xS_2$) with different alloying concentration ($x = 0.3, 0.5, 0.7$). The dark atoms are the Mo atoms, while the bright atoms are the W atoms. Based on this contrast, I can find that the two atoms are randomly distributed in the few-layer areas without obvious clustering or vacancy observed. Based on the comparison among different figures, the density of bright atoms increases as the W concentration (x) rises as expected. The next step is to perform heating experiments on these samples of different alloying concentrations.

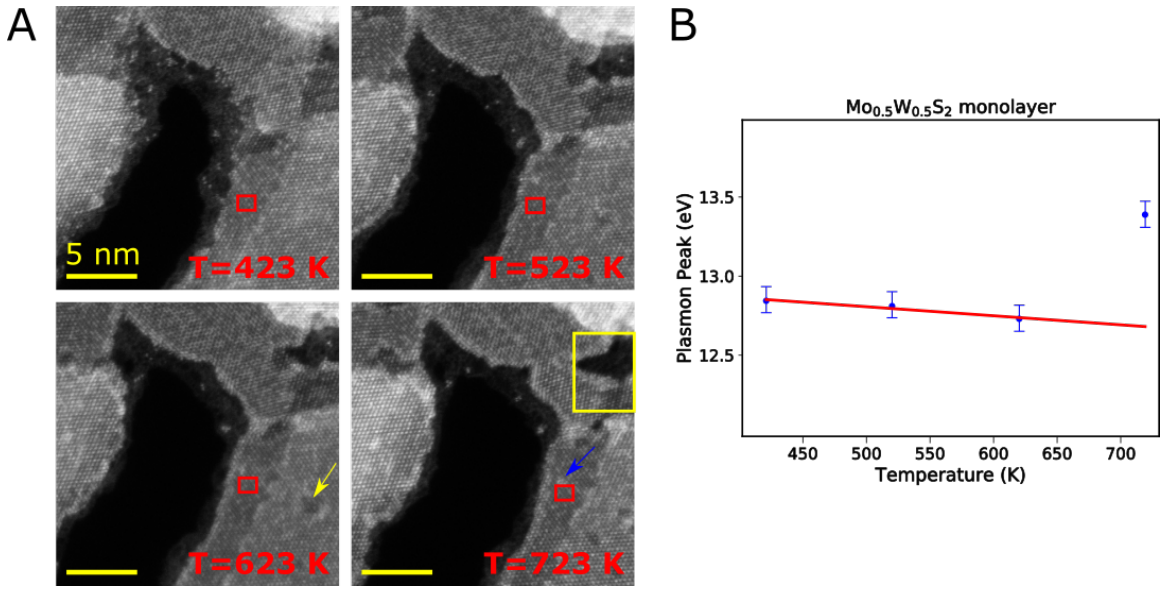

Figure 30: A) Atomic resolution HAADF image of TMD alloys ($Mo_{0.5}W_{0.5}S_2$) at different temperature and B) the corresponding plasmon energy as a function of temperature. The plasmon energy is determined from the low-loss EELS recorded in the red rectangle area. The yellow rectangle, the yellow arrow and the blue arrow indicate the defects forming in the heating process.

For the first step of the experiments, I will explore the heating effects on the lattice structure. As an example, Figure 30A) shows the atomic resolution HAADF images of TMD alloy $Mo_{0.5}W_{0.5}S_2$ at different temperatures (423 K - 723 K). During the heating process, the monolayer area (the yellow rectangle area) is gradually destroyed which may stem from the large thermal expansion of the monolayer area. At the same time, the atoms diffuse and accumulate on the edge of two-layers-thick area, and triangle shaped vacancies form and grow in the two-layer-thick area (the yellow arrow). Despite the destructive effects in the monolayer, in two-layer and thicker areas the heating results in the formation of atom clusterings and the

triangle shaped vacancies which can easily diffuse in the few-layer areas at high temperature. This redistribution of lattice defects can influence the measurements of the plasmon energy.

Figure 30B) presents the corresponding measured plasmon energy as a function of temperature acquired using the low-loss EELS recorded in the red rectangle areas. I find that the plasmon energy exhibit a linear relationship with the temperature at the regime (T = 423 K - 623 K), while it suddenly increases at T = 723 K. This increase can be due to two effects, I observed in the atomic resolution images: 1), The atoms accumulate at the edge: due to the delocalization of plasmon signals, the EEL spectra recorded in the red rectangle may be influenced by the change of edges structures. The higher density of atoms brings a higher concentration of free electrons and hence increases the plasmon energy. 2), There is a cluster of W atoms near the area where the EELS was acquired. This cluster appears to move at elevated temperature (see blue arrow). The change of plasmon energy occurs simultaneously as the W cluster diffuses across the area. I attribute this change in plasmon energy to the diffusion of the W cluster into the EELS area.

In the following heating experiments, all the EELS recording areas are selected to be at least 2 nm away from the edges without any visible defect even at high temperature. The atomic resolution images are recorded before and after each EELS acquisition.

As an example, Figure 31 shows a typical sample area for $Mo_{0.3}W_{0.7}S_2$ at T = 723 K and corresponding plasmon energy shift on this sample compared with the pure materials MoS_2 and WS_2. Figure 31A) shows that in this monolayer sample there is no defect in the recording area. The plasmon energy shift from this sample is smaller than both pure materials

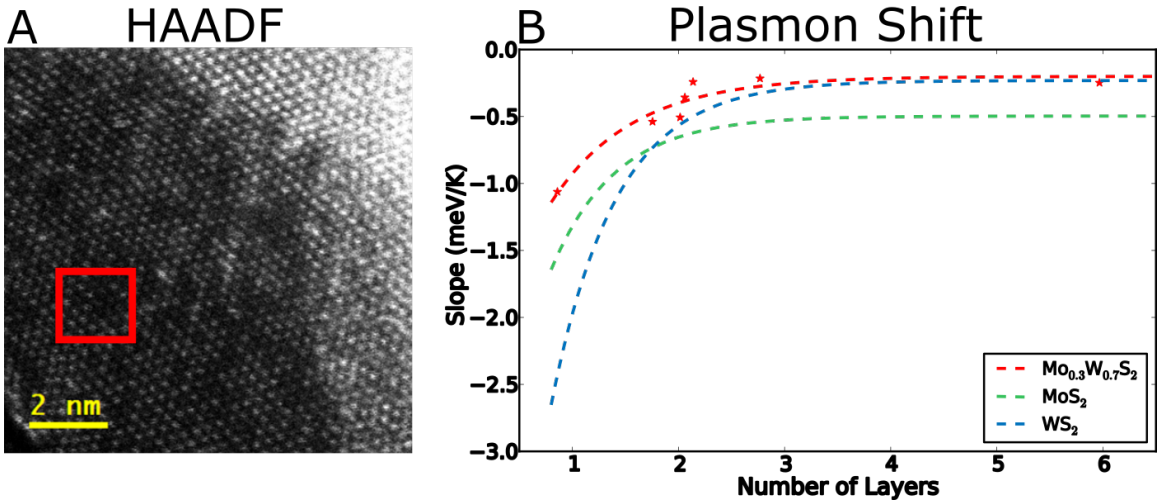

Figure 31: A) Atomic resolution HAADF image of $Mo_{0.3}W_{0.7}S_2$ at T = 723 K and B) corresponding plasmon energy shift on this sample in different thickness compared with the pure materials MoS_2 and WS_2.

in the 1L - 3L thickness and approaches the value from WS_2 when the thickness is above three layers (as seen in Figure 31B). This trend shows the potential of alloy engineering on the thermal expansion coefficients. For a complete analysis of the thermal expansion behavior of TMD alloys, simulations of the plasmon energy shift in terms of the lattice expansion will be performed next.

Due to the difficulties in simulating a randomly distributed structure with a periodic approximation, I use the Special Quasirandom Structure (SQS) (120). The special quasirandom structure is a structure which considers the correlation of the nearby sites and makes this correlation close enough to the one from the truly disordered structure. I generate the SQS using a Monte-Carlo algorithm implemented in the Alloy Theoretic Automated Toolkit (ATAT) (120). Figure 32A) presents a typical SQS of $Mo_{0.3}W_{0.7}S_2$ in the top and side view. For different al-

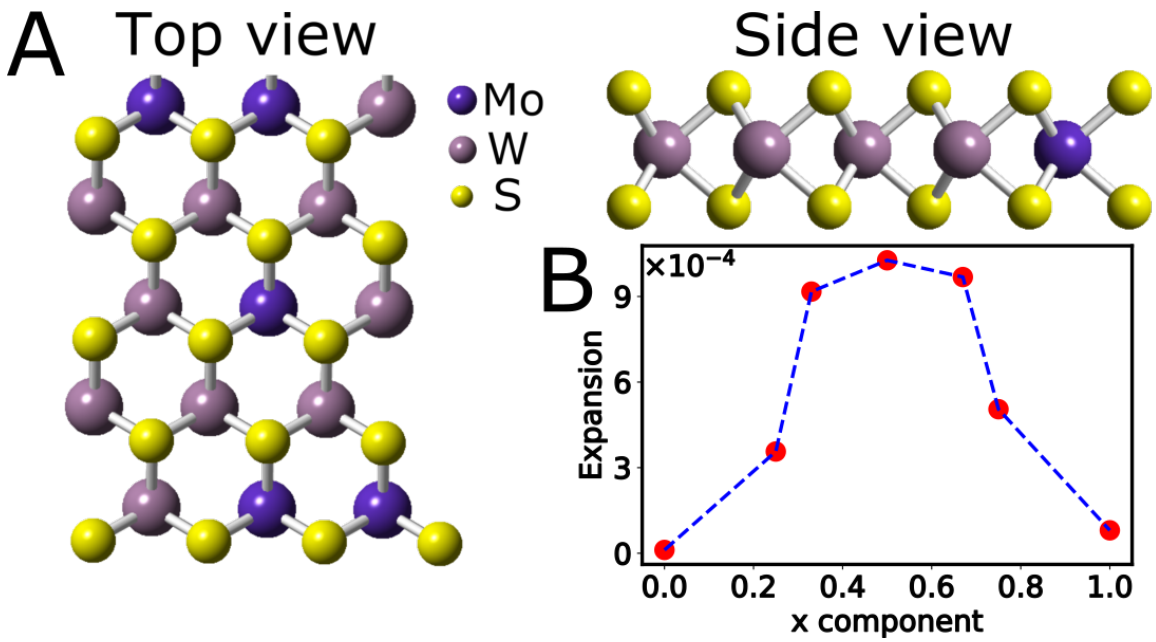

Figure 32: A) The special quasirandom structure (SQS) of $Mo_{0.3}W_{0.7}S_2$ in the top and side view and B) corresponding relaxed lattice constant as a function of alloying concentration (x) compared with the one from MoS_2.

loying concentration, the corresponding SQS is generated and relaxed to an energetically stable structure. Compared with the lattice constant of MoS_2, the relaxed lattice constant is plotted in Figure 32B) as a function of alloying concentration. It turns out that the lattice sightly expands during the alloying process and reaches the maximum when Mo and W atoms have the same concentration.

Based on the SQS I generate, the frequency dependent dielectric functions ($\varepsilon(\omega)$) for different TMD alloys ($x = 0.33, 0.5, 0.67$) are calculated by RPA. The corresponding EELS signals, $Im(-1/\varepsilon$, are simulated to determine the plasmon energy shift as a function of lattice expansion.

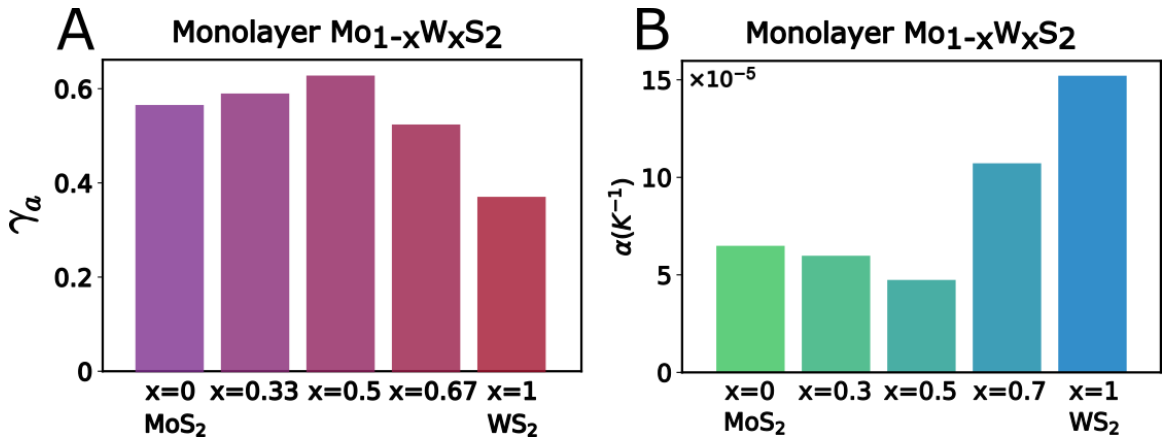

Figure 33: A) Calculated γ_a and B) the thermal expansion coefficients (α) of monolayer $Mo_{1-x}W_xS_2$ at different alloying concentrations ($x = 0, 0.3, 0.5, 0.7, 1$).

The parameter γ_a is then calculated and plotted in Figure 33A). The γ_a reaches a maximum value for an equally alloying ($x = 0.5$).

Based on the parameter γ_a and the experimental plasmon shift of the materials, the thermal expansion coefficients for different monolayer TMD alloys are predicted (Figure 33B)). From this figure, I find that alloy engineering can tune the thermal expansion behavior of materials. But it is interesting to note that the thermal expansion is not linear with the alloying concentration. The thermal expansion coefficients of all TMD alloys are reduced by the alloy engineering and reach a minimum value for $Mo_{0.5}W_{0.5}S_2$.

Due to the random distribution of Mo and W atoms in the alloys, the nearest neighbor surroundings for Mo or W atom are not symmetrical as in pure materials, resulting in a local stress σ. The direction and value of this stress depend on the configuration and it will be released via a small redistribution or buckling to form a stable configuration. The random

displacements from the original sites may interfere with the propagation of phonons and thus constrain the thermal expansion during heating. The interference stems from the randomness of the configuration, which will reach a maximum (i.e. highest entropy) at the equally alloyed sample ($Mo_{0.5}W_{0.5}S_2$).

The reduction in the thermal expansion coefficients shows a great potential to control the thermal expansion mismatch at hetero-interface as formed in the design of electronic device. The gradual change from one material to another may occur in the interface of two materials. The non-linear reduction of thermal expansion coefficients at the interface may be of critical interest in the device design. This hypothesis needs further confirmation from experiments.

CHAPTER 7

CONCLUSION AND OUTLOOK

The thermal properties of electronic devices are of great importance in materials research. However, as the current electronic devices are scaled down to the nanometer size, the nanoscale thermal characterization techniques are not well developed, but needed for future studies. In this thesis, I have demonstrated a systematic nanoscale thermal characterization study using the combination of STEM/EELS and first-principles calculations, which includes an indirect and a direct characterization method.

The indirect characterization method is to explore the nanoscale electronic properties of materials by STEM/EELS and first-principles calculations, and then study the relation between thermal properties and electronic properties to explain the thermal phenomenon. Here, I utilized the indirect characterization method to explore the Ti dopant effects on the crystal structure and electronic structure of CCO and explain the unchanged Seebeck coefficient after Ti doping. Specifically, I used the STEM/EELS techniques to locate the Ti dopants which were mainly located in the RS sub-system. However, in CCO, the Seebeck coefficients are mainly determined by the concentration and spin state of Co^{4+} which are located in CoO_2 layer. The influence of Ti dopants in RS layer was limited on the electronic structure of Co^{4+} in the CoO_2 layer, which was confirmed by the Co L- and O K-edge EELS and the density of states calculations of Ti-doped CCO. For a higher doping concentration, the Ti atoms may start to replace the Co atoms in the CoO_2 layer and influence the electronic structures of Co^{4+} to tune

the thermoelectric property of CCO. The researches in both experiments and calculations for a high concentration Ti-doped CCO are needed to provide a complete study of Ti dopant effects. Furthermore, if the direct thermal characterization method can be developed, the in-situ local defect effects can be observed.

The direct characterization method measures the local temperature and thermal properties using STEM/EELS and first-principles mechanics, and studies local defect effects on the nanoscale thermal properties. Here, I demonstrated a direct characterization method to predict the nanoscale temperature and thermal expansion properties of 2D materials (graphene and TMDs). Specifically, based on the temperature dependent plasmon energy shift recorded from EELS, I can measure the temperature from a sub-10 nm area with the combination of atomic resolution imaging (STEM). Combining this temperature dependent shift with the lattice expansion dependent shift simulated by DFT and RPA, I predicted the thermal expansion coefficients of different 2D materials from monolayer to bulk with a high spatial resolution ($\approx$ 2.1 nm). The thermal expansion coefficient from each monolayer 2D material was almost one order of magnitude larger than the one from bulk, which suggested a severe thermal expansion mismatch problem in the design of electronic devices. Predicting and controlling the thermal expansion behavior of 2D materials to avoid strain induced fracture will be critical for the future application and researches.

Then, I utilized the nanoscale thermal expansion measurement technique on the TMD alloys ($Mo_{1-x}W_xS_2$). In the in-situ heating experiments, I observed the temperature induced a structural change in the few-layer areas using the atomic resolution STEM images. During

heating, the relative distribution of Mo and W atoms did not significantly change, but the atom clusters and vacancies formed, grew and diffused easily due to the internal energy at high temperature. Since the defects will largely influence the plasmon energy in that area, atomic resolution EELS is needed and performed for the thermal expansion measurement of TMD alloys. With the EELS simulation based on the special quasirandom structures (SQS) of alloyed samples, I predicted the thermal expansion coefficients of monolayer TMD alloys. The thermal expansion coefficients are reduced upon additional substitutional doping (Mo or W atoms). The strains upon doping were confirmed by the SQS simulations and are predicted to interfere with the lattice expansion of materials. Control of thermal expansion behavior by alloy engineering suggests a potential to avoid the thermal expansion mismatch or strain-induced fracture in the design of 2D-material-based devices. It also suggests that the thermal expansion between two different materials may be not a linear transition from one to another one which is of great importance in the fundamental research and future applications. In the future, it will be interesting to explore the thermal expansion behavior across the TMD in-plane hetero-structures.

More importantly, the high spatial resolution of this technique enables future studies of thermal properties at the hetero-interface, hybrid nanostructures, or other low-dimensional structures such as quantum dots and nanowires, which will be crucial to further understand the thermal transport properties of materials in nano-scale devices. Here, I proposed two possible approaches for the research on thermal transport properties of the in-plane hetero-interface: 1), examine the temperature variance on the sample with a spatial thermal gradient

across the interface. The spatial thermal gradient can be achieved by applying a metal wire between electrodes of electric chips to support a heating flow on the sample. 2), examine the in-situ temporal temperature variance on the sample and background simultaneously. Since the temperature of the background (can be observed by applying reference materials on the carbon film) is designed to reach the desired temperature immediately, it can be used as a reference temperature for this temporal temperature changing process. This in-situ observation of the process of reaching thermal equilibrium can be then used to explore the thermal transport properties between the sample and background, and between the two materials around the interface.

The second approach can be achieved due to the high temporal resolution (acquisition time $< 10^{-3}$ s) of the low-loss EELS for plasmon energy. It suggests a potential of in-situ experiments of the dynamics of temperature change or the free electron density change, which could be used for the research of the thermal properties or chemical reactions of materials, or both (heat in exothermic reaction). The sensitivity of this technique is determined by the energy resolution of EELS (0.35 eV for our JEOL ARM) which is high enough for the current thermal property analysis. However, a possible ultra-high energy resolution of monochromated EELS ($<$ 10 meV) could extend the application of this technique to a variety of studies, such as temperature effects on the local phonon energy, the role of the phonon vibration on the thermal transport, defect effects on the phonon transport, and the couplings between phonon and plasmon. The ultra-high energy resolution can provide a much higher temperature resolution and potentially depict the temperature dependent thermal expansion behavior which is especially important

for graphene at low temperature (since TEC of graphene is not constant or simply linear at low temperature). This resolution can also detect new information for analyzing the mechanisms of the plasmon energy shift phenomenon. This direct nanoscale thermal characterization technique has presented a variety of possibilities on the thermal property studies so far and can be used to provide a comprehensive and fundamental understanding on the thermal properties of nanomaterials.

APPENDICES

AIP PUBLISHING LICENSE
TERMS AND CONDITIONS

Dec 13, 2018

This Agreement between Mr. Xuan Hu ("You") and AIP Publishing ("AIP Publishing") consists of your license details and the terms and conditions provided by AIP Publishing and Copyright Clearance Center.

License Number	4473251226789
License date	Nov 20, 2018
Licensed Content Publisher	AIP Publishing
Licensed Content Publication	Journal of Applied Physics
Licensed Content Title	Atomic and electronic structure of Ti substitution in Ca3Co4O9
Licensed Content Author	Xuan Hu, Patrick J Phillips, Dipanjan Mazumdar, et al
Licensed Content Date	Nov 28, 2016
Licensed Content Volume	120
Licensed Content Issue	20
Type of Use	Thesis/Dissertation
Requestor type	Author (original article)
Format	Electronic
Portion	Excerpt (> 800 words)
Will you be translating?	No
Title of your thesis / dissertation	Atomic Scale Study of Thermal Properties using STEM/EELS and First-Principles Calculations
Expected completion date	Dec 2018
Estimated size (number of pages)	110
Requestor Location	Mr. Xuan Hu 1710 W 33RD PL CHICAGO, IL 60608 United States Attn: Mr. Xuan Hu
Billing Type	Invoice
Billing Address	Mr. Xuan Hu 1710 W 33RD PL CHICAGO, IL 60608 United States Attn: Mr. Xuan Hu
Total	0.00 USD
Terms and Conditions	

American Physical Society Reuse and Permissions License

20-Nov-2018

This license agreement between the American Physical Society ("APS") and Xuan Hu ("You") consists of your license details and the terms and conditions provided by the American Physical Society and SciPris.

Licensed Content Information

License Number:	**RNP/18/NOV/009632**
License date:	20-Nov-2018
DOI:	10.1103/PhysRevLett.120.055902
Title:	Mapping Thermal Expansion Coefficients in Freestanding 2D Materials at the Nanometer Scale
Author:	Xuan Hu et al.
Publication:	Physical Review Letters
Publisher:	American Physical Society
Cost:	USD $ 0.00

Request Details

Does your reuse require significant modifications: No

Specify intended distribution locations:	United States
Reuse Category:	Reuse in a thesis/dissertation
Requestor Type:	Author of requested content
Items for Reuse:	Whole Article
Format for Reuse:	Electronic

Information about New Publication:

University/Publisher:	University of Illinois at Chicago
Title of dissertation/thesis:	Atomic Scale Study of Thermal Properties using STEM/EELS and First-Principles Calculations
Author(s):	Xuan Hu
Expected completion date:	Dec. 2018

License Requestor Information

Name:	Xuan Hu
Affiliation:	Individual
Email Id:	lakerhoo@gmail.com
Country:	United States

JOHN WILEY AND SONS LICENSE TERMS AND CONDITIONS

Dec 13, 2018

This Agreement between Mr. Xuan Hu ("You") and John Wiley and Sons ("John Wiley and Sons") consists of your license details and the terms and conditions provided by John Wiley and Sons and Copyright Clearance Center.

License Number	4477120468827
License date	Nov 27, 2018
Licensed Content Publisher	John Wiley and Sons
Licensed Content Publication	Advanced Materials
Licensed Content Title	Vibrational Spectroscopy of Water with High Spatial Resolution
Licensed Content Author	Jacob R. Jokisaari, Jordan A. Hachtel, Xuan Hu, et al
Licensed Content Date	Jul 30, 2018
Licensed Content Volume	30
Licensed Content Issue	36
Licensed Content Pages	6
Type of use	Dissertation/Thesis
Requestor type	Author of this Wiley article
Format	Electronic
Portion	Figure/table
Number of figures/tables	1
Original Wiley figure/table number(s)	Figure 1
Will you be translating?	No
Title of your thesis / dissertation	Atomic Scale Study of Thermal Properties using STEM/EELS and First-Principles Calculations
Expected completion date	Dec 2018
Expected size (number of pages)	110
Requestor Location	Mr. Xuan Hu 1710 W 33RD PL CHICAGO, IL 60608 United States Attn: Mr. Xuan Hu
Publisher Tax ID	EU826007151
Total	0.00 USD
Terms and Conditions	

TERMS AND CONDITIONS

This copyrighted material is owned by or exclusively licensed to John Wiley & Sons, Inc. or one of its group companies (each a"Wiley Company") or handled

SPRINGER NATURE LICENSE
TERMS AND CONDITIONS

Dec 13, 2018

This Agreement between Mr. Xuan Hu ("You") and Springer Nature ("Springer Nature") consists of your license details and the terms and conditions provided by Springer Nature and Copyright Clearance Center.

License Number	4477110933683
License date	Nov 27, 2018
Licensed Content Publisher	Springer Nature
Licensed Content Publication	Springer eBook
Licensed Content Title	Elastic Scattering
Licensed Content Author	David B. Williams, C. Barry Carter
Licensed Content Date	Jan 1, 2009
Type of Use	Thesis/Dissertation
Requestor type	academic/university or research institute
Format	electronic
Portion	figures/tables/illustrations
Number of figures/tables /illustrations	2
Will you be translating?	no
Circulation/distribution	<501
Author of this Springer Nature content	no
Title	Atomic Scale Study of Thermal Properties using STEM/EELS and First-Principles Calculations
Institution name	n/a
Expected presentation date	Dec 2018
Portions	Figure 3.1, Figure 22.3.
Requestor Location	Mr. Xuan Hu 1710 W 33RD PL CHICAGO, IL 60608 United States Attn: Mr. Xuan Hu
Billing Type	Invoice
Billing Address	Mr. Xuan Hu 1710 W 33RD PL CHICAGO, IL 60608 United States Attn: Mr. Xuan Hu
Total	0.00 USD

IOP Publishing LICENSE
TERMS AND CONDITIONS

Dec 13, 2018

This is a License Agreement between Mr. Xuan Hu ("You") and IOP Publishing ("IOP Publishing") provided by Copyright Clearance Center ("CCC"). The license consists of your order details, the terms and conditions provided by IOP Publishing, and the payment terms and conditions.

All payments must be made in full to CCC. For payment instructions, please see information listed at the bottom of this form.

License Number	4477121136728
License date	Nov 27, 2018
Licensed content publisher	IOP Publishing
Licensed content title	Reports on Progress in Physics
Licensed content date	Jan 1, 1934
Type of Use	Thesis/Dissertation
Requestor type	Academic institution
Format	Electronic
Portion	image/photo
Number of images/photos requested	1
The requesting person/organization is:	Xuan Hu
Title or numeric reference of the portion(s)	Figure 5
Title of the article or chapter the portion is from	N/A
Editor of portion(s)	N/A
Author of portion(s)	R F Egerton
Volume of serial or monograph.	N/A
Page range of the portion	6
Publication date of portion	N/A
Rights for	Main product
Duration of use	Life of current edition
Creation of copies for the disabled	no
With minor editing privileges	no
For distribution to	Worldwide
In the following language(s)	Original language of publication
With incidental promotional use	no

The lifetime unit quantity of new product	Up to 499
Title	Atomic Scale Study of Thermal Properties using STEM/EELS and First-Principles Calculations
Institution name	n/a
Expected presentation date	Dec 2018
Billing Type	Invoice
Billing Address	Mr. Xuan Hu 1710 W 33RD PL CHICAGO, IL 60608 United States Attn: Mr. Xuan Hu
Total (may include CCC user fee)	0.00 USD
Terms and Conditions	

TERMS AND CONDITIONS

The following terms are individual to this publisher:

These special terms and conditions are in addition to the standard terms and conditions for CCC's Republication Service and, together with those standard terms and conditions, govern the use of the Works.

As the "User" you will make all reasonable efforts to contact the author(s) of the article which the Work is to be reused from, to seek consent for your intended use. Contacting one author who is acting expressly as authorised agent for their co-author(s) is acceptable.

User will reproduce the following wording prominently alongside the Work:

- the source of the Work, including author, article title, title of journal, volume number, issue number (if relevant), page range (or first page if this is the only information available) and date of first publication. This information can be contained in a footnote or reference note; and
- a link back to the article (via DOI); and
- if practicable, and IN ALL CASES for new works published under any of the Creative Commons licences, the words "© IOP Publishing. Reproduced with permission. All rights reserved"

Without the express permission of the author(s) and the Rightsholder of the article from which the Work is to be reused, User shall not use it in any way which, in the opinion of the Rightsholder, could: (i) distort or alter the author(s)' original intention(s) and meaning; (ii) be prejudicial to the honour or reputation of the author(s); and/or (iii) imply endorsement by the author(s) and/or the Rightsholder.

This licence does not apply to any article which is credited to another source and which does not have the copyright line '© IOP Publishing Ltd'. User must check the copyright line of the article from which the Work is to be reused to check that IOP Publishing Ltd has all the necessary rights to be able to grant permission. User is solely responsible for identifying and obtaining

CITED LITERATURE

1. Hu, X. *et al.* Atomic and Electronic Structure of Ti Substitution in $Ca_3Co_4O_9$. *Journal of Applied Physics* **120**, 205105 (2016).

2. Hu, X. *et al.* Mapping thermal expansion coefficients in freestanding 2d materials at the nanometer scale. *Phys. Rev. Lett.* **120**, 055902 (2018).

3. Majumdar, A. *et al.* Thermal imaging by atomic force microscopy using thermocouple cantilever probes. *Review of Scientific Instruments* **66**, 3584–3592 (1995).

4. De Wilde, Y. *et al.* Thermal radiation scanning tunnelling microscopy. *Nature* **444**, 740–743 (2006).

5. Soudi, A., Dawson, R. D. & Gu, Y. Quantitative Heat Dissipation Characteristics in Current-Carrying GaN Nanowires Probed by Combining Scanning Thermal Microscopy and Spatially Resolved Raman Spectroscopy. *ACS Nano* **5**, 255–262 (2011).

6. Menges, F., Riel, H., Stemmer, A. & Gotsmann, B. Quantitative Thermometry of Nanoscale Hot Spots. *Nano Letters* **12**, 596–601 (2012).

7. Menges, F. *et al.* Temperature mapping of operating nanoscale devices by scanning probe thermometry. *Nature Communications* **7**, 10874 EP – (2016).

8. Calizo, I., Balandin, A. A., Bao, W., Miao, F. & Lau, C. N. Temperature Dependence of the Raman Spectra of Graphene and Graphene Multilayers. *Nano Letters* **7**, 2645–2649 (2007).

9. Okabe, K. *et al.* Intracellular temperature mapping with a fluorescent polymeric thermometer and fluorescence lifetime imaging microscopy. *Nature Communications* **3**, 705 EP – (2012).

10. Brites, C. D. S. *et al.* Thermometry at the nanoscale. *Nanoscale* **4**, 4799–4829 (2012).

11. Niekiel, F., Kraschewski, S. M., Mller, J., Butz, B. & Spiecker, E. Local temperature measurement in TEM by parallel beam electron diffraction. *Ultramicroscopy* **176**, 161 – 169 (2017).

12. Idrobo, J. C. *et al.* Temperature measurement by a nanoscale electron probe using energy gain and loss spectroscopy. *Phys. Rev. Lett.* **120**, 095901 (2018).

13. De Broglie, L. *Recherches sur la théorie des Quanta.* Theses, Migration - université en cours d'affectation (1924).

14. Davisson, C. J. & Germer, L. H. Reflection of Electrons by a Crystal of Nickel. *Proceedings of the National Academy of Science* **14**, 317–322 (1928).

15. Thomson, G. P. & Reid, A. Diffraction of Cathode Rays by a Thin Film. *Nature* **119**, 890 (1927).

16. Ruska, E. The development of the electron microscope and of electron microscopy. *Rev. Mod. Phys.* **59**, 627–638 (1987).

17. von Ardenne, M. Das Elektronen-Rastermikroskop. *Zeitschrift fur Physik* **109**, 553–572 (1938).

18. Crewe, A. V., Wall, J. & Langmore, J. Visibility of single atoms. *Science* **168**, 1338–1340 (1970).

19. NightLase Technologies. Chromatic and spherical aberration.

20. Pennycook, S. J. & Nellist, P. D. *ScanningTransmission Electron Microscopy —imaging and analysis* (2011).

21. Scherzer, O. The theoretical resolution limit of the electron microscope. *Journal of Applied Physics* **20**, 20–29 (1949).

22. Haider, M. *et al.* A spherical-aberration-corrected 200kv transmission electron microscope. *Ultramicroscopy* **75**, 53 – 60 (1998).

23. Krivanek, O., Dellby, N. & Lupini, A. Towards sub- electron beams. *Ultramicroscopy* **78**, 1 – 11 (1999).

24. Batson, P. E., Dellby, N. & Krivanek, O. L. Sub-angstrom resolution using aberration corrected electron optics. *Nature* **418**, 617 EP – (2002).

25. Williams, D. B. & Carter, C. B. (Springer US, Boston, MA, 2009).

26. Pennycook, S. & Jesson, D. High-resolution z-contrast imaging of crystals. *Ultramicroscopy* **37**, 14 – 38 (1991).

27. Krivanek, O. L. *et al.* Atom-by-atom Structural and Chemical Analysis by Annular Dark-field Electron Microscopy. *Nature* **464**, 571–574 (2010).

28. Yougui Liao. Practical electron microscopy and database (2006).

29. Jokisaari, J. R. *et al.* Vibrational spectroscopy of water with high spatial resolution. *Advanced Materials* **30**, 1802702 (2018).

30. Egerton, R. F. Electron energy-loss spectroscopy in the TEM. *Reports on Progress in Physics* **72**, 016502 (2008).

31. Born, M. & Oppenheimer, R. Zur Quantentheorie der Molekeln. *Annalen der Physik* **389**, 457–484 (1927).

32. Hohenberg, P. & Kohn, W. Inhomogeneous electron gas. *Phys. Rev.* **136**, B864 – B871 (1964).

33. Kohn, W. & Sham, L. J. Self-Consistent Equations Including Exchange and Correlation Effects. *Phys. Rev.* **140**, 1133–1138 (1965).

34. Vosko, S. H., Wilk, L. & Nusair, M. Accurate spin-dependent electron liquid correlation energies for local spin density calculations: a critical analysis. *Canadian Journal of Physics* **58**, 1200 (1980).

35. Perdew, J. P. & Zunger, A. Self-interaction correction to density-functional approximations for many-electron systems. *Phys. Rev. B* **23**, 5048–5079 (1981).

36. Cole, L. A. & Perdew, J. P. Calculated electron affinities of the elements. *Phys. Rev. A* **25**, 1265–1271 (1982).

37. Perdew, J. P. & Wang, Y. Accurate and simple analytic representation of the electron-gas correlation energy. *Phys. Rev. B* **45**, 13244–13249 (1992).

38. Perdew, J. P. *et al.* Atoms, molecules, solids, and surfaces: Applications of the generalized gradient approximation for exchange and correlation. *Phys. Rev. B* **46**, 6671–6687 (1992).

39. Perdew, J. P., Burke, K. & Ernzerhof, M. Generalized gradient approximation made simple. *Phys. Rev. Lett.* **77**, 3865–3868 (1996).

40. Grossman, J. C., Mitas, L. & Raghavachari, K. Structure and stability of molecular carbon: Importance of electron correlation. *Phys. Rev. Lett.* **75**, 3870–3873 (1995).

41. He, L. *et al.* Accuracy of generalized gradient approximation functionals for density-functional perturbation theory calculations. *Phys. Rev. B* **89**, 064305 (2014).

42. Perdew, J. P. & Schmidt, K. Jacobs ladder of density functional approximations for the exchange-correlation energy. *AIP Conference Proceedings* **577**, 1–20 (2001).

43. Langreth, D. C. & Perdew, J. P. Exchange-correlation energy of a metallic surface: Wave-vector analysis. *Phys. Rev. B* **15**, 2884–2901 (1977).

44. Bohm, D. & Pines, D. A collective description of electron interactions: Iii. coulomb interactions in a degenerate electron gas. *Phys. Rev.* **92**, 609–625 (1953).

45. Yang, J. & Caillat, T. Thermoelectric materials for space and automotive power generation. *MRS Bull.* **31**, 224–229 (2006).

46. Taylor, R. & Solbrekken, G. Comprehensive system-level optimization of thermoelectric devices for electronic cooling applications. *Components and Packaging Technologies, IEEE Transactions on* **31**, 23–31 (2008).

47. Masset, A. C. *et al.* Misfit-layered cobaltite with an anisotropic giant magnetoresistance: $Ca_3Co_4O_9$. *Phys. Rev. B* **62**, 166–175 (2000).

48. Limelette, P. *et al.* Strongly correlated properties of the thermoelectric cobalt oxide $Ca_3Co_4O_9$. *Phys. Rev. B* **71**, 233108 (2005).

49. Flahaut, D. *et al.* Thermoelectrical properties of a-site substituted ca1xrexmno3 system. *J. Appl. Phys.* **100**, – (2006).

50. Shikano, M. & Funahashi, R. Electrical and thermal properties of single-crystalline $(Ca_2CoO_3)_{0.7}CoO_2$ with a $Ca_3Co_4O_9$ structure. *Appl. Phys. Lett.* **82**, 1851–1853 (2003).

51. Miyazaki, Y. *et al.* Modulated Structure of the Thermoelectric Compound $[Ca_2CoO_3]_{0.62}CoO_2$. *J. Phys. Soc. Japan* **71**, 491–497 (2002).

52. Yang, G., Ramasse, Q. & Klie, R. F. Direct measurement of charge transfer in thermoelectric $Ca_3Co_4O_9$. *Phys. Rev. B* **78**, 153109 (2008).

53. Yang, G., Ramasse, Q. & Klie, R. F. Direct measurement of Co-ion spin state transitions in $Ca_3Co_4O_9$ using variable-temperature electron energy-loss spectroscopy. *Appl. Phys. Lett.* **94**, – (2009).

54. Zhao, B. C., Sun, Y. P., Lu, W. J., Zhu, X. B. & Song, W. H. Enhanced spin fluctuations in $Ca_3Co_{4-x}Ti_xO_9$ single crystals. *Phys. Rev. B* **74**, 144417 (2006).

55. Zhao, B. C., Sun, Y. P. & Song, W. H. Magnetic and transport properties in the Ti doped cobaltite $Ca_3Co_{4-x}Ti_xO_9$ ($0 < x < 0.8$) single crystals. *J. Appl. Phys.* **99**, – (2006).

56. Matsubara, I., Funahashi, R., Shikano, M., Sasaki, K. & Enomoto, H. Cation substituted $(Ca_2CoO_3)_xCoO_2$ films and their thermoelectric properties. *Appl. Phys. Lett.* **80**, 4729–4731 (2002).

57. Xu, G., Funahashi, R., Shikano, M., Matsubara, I. & Zhou, Y. Thermoelectric properties of the Bi- and Na-substituted $Ca_3Co_4O_9$ system. *Appl. Phys. Lett.* **80**, 3760–3762 (2002).

58. Koshibae, W., Tsutsui, K. & Maekawa, S. Thermopower in cobalt oxides. *Physical Review B - Condensed Matter and Materials Physics* **62**, 6869–6872 (2000).

59. Klie, R. F. *et al.* Observations of Co^{4+} in a higher spin state and the increase in the seebeck coefficient of thermoelectric $Ca_3Co_4O_9$. *Physical Review Letters* **108**, 1–5 (2012).

60. Qiao, Q. *et al.* Effect of substrate on the atomic structure and physical properties of thermoelectric $Ca_3Co_4O_9$ thin films. *J. Phys. Condens. Matter* **23**, 305005 (2011).

61. Rébola, A., Klie, R., Zapol, P. & Öğüt, S. First-principles study of the atomic and electronic structures of misfit-layered calcium cobaltite $(Ca_2CoO_3)(CoO_2)_{1.62}$ using rational approximants. *Phys. Rev. B* **85**, 155132 (2012).

62. Rbola, A., Klie, R. F., Zapol, P. & t, S. Phonon and thermal transport properties of the misfit-layered oxide thermoelectric $Ca_3Co_4O_9$ from first principles. *Appl. Phys. Lett.* **104**, – (2014).

63. Wang, Y. *et al.* Strongly Correlated Properties and Enhanced Thermoelectric Response in $Ca_3Co_{4-x}M_xO_9$ (M = Fe, Mn, and Cu). *Chem. Mater.* **22**, 1155–1163 (2010).

64. Altin, S., Bayri, A., Demirel, S. & Aksan, M. Thermal conductivity and magnetic properties of the B substituted $Ca_3Co_4O_9$. *Curr. Appl. Phys.* **14**, 590 – 595 (2014).

65. Fu, Y., Lin, S., Huang, Y., Shi, R. & Zhao, B. Cr^{6+} ion doping effects in layered $Ca_3Co_4O_9$ system. *J. Alloys Compd.* **613**, 87 – 92 (2014).

66. Yao, Q., Wang, D. L., Chen, L. D., Shi, X. & Zhou, M. Effects of partial substitution of transition metals for cobalt on the high-temperature thermoelectric properties of $Ca_3Co_4O_{9+\sigma}$. *J. Appl. Phys.* **97**, – (2005).

67. Liu, C. J., Huang, L. C. & Wang, J. S. Improvement of the thermoelectric characteristics of Fe-doped misfit-layered $Ca_3Co_{4-x}Fe_xO_{9+\sigma}$ (x = 0,0.05,0.1, and 0.2). *Appl. Phys. Lett.* **89** (2006).

68. Srepusharawoot, P., Pinitsoontorn, S. & Maensiri, S. Electronic structure of iron-doped misfit-layered calcium cobaltite. *Comput. Mater. Sci.* **114**, 64 – 71 (2016).

69. Xu, L., Li, F. & Wang, Y. High-temperature transport and thermoelectric properties of ca3co4xtixo9. *J. Alloys Compd.* **501**, 115 – 119 (2010).

70. Torres, M. *et al.* Decrease of electrical resistivity in $Ca_3Co_4O_9$ thermoelectric ceramics by Ti doping. *J. Mater. Sci. - Mater. Electron.* **26**, 815–820 (2015).

71. Hu, Y. F., Sutter, E., Si, W. D. & Li, Q. Thermoelectric properties and microstructure of c-axis-oriented $Ca_3Co_4O_9$ thin films on glass substrates. *Appl. Phys. Lett.* **87** (2005).

72. Kresse, G. & Hafner, J. Ab initio molecular dynamics for liquid metals. *Physical Review B* **47**, 558–561 (1993).

73. M. P. Teter, M. C. Payne and D. C. Allan. *Phys. Rev. B* **40**, 12255 (1989).

74. Monkhorst, H. J. & Pack, J. D. Special points for Brillouin-zone integrations. *Phys. Rev. B* **13**, 5188–5192 (1976).

75. Zhang, S. B. The microscopic origin of the doping limits in semiconductors and wide-gap materials and recent developments in overcoming these limits: a review. *J. Phys.: Condens. Matter* **14**, R881 (2002).

76. Van de Walle, C. G. & Neugebauer, J. First-principles calculations for defects and impurities: Applications to iii-nitrides. *J. Appl. Phys.* **95**, 3851–3879 (2004).

77. Hellberg, C. S., Andersen, K. E., Li, H., Ryan, P. J. & Woicik, J. C. Structure of srtio$_3$ films on si. *Phys. Rev. Lett.* **108**, 166101 (2012).

78. *In principle, the formation energy of a defect will depend on the individual chemical potentials. However, the constraint imposed by the condition of avoiding precipitation of bulk CoO,* Co_3O_4 *and* $CaTiO_3$ *forces the* μ_{Ti} *to attain its maximum value which also fixes the chemical potential* μ_{Ca}*,* μ_{Co} *and* μ_O*. The formation energies given in the text correspond to this particular point in the ternary phase diagram* .

79. Leapman, R. D., Grunes, L. A. & Fejes, P. L. Study of the L_{23} edges in the $3d$ transition metals and their oxides by electron-energy-loss spectroscopy with comparisons to theory. *Phys. Rev. B* **26**, 614–635 (1982).

80. Sankararaman, M. & Perry, D. Valence determination of titanium and iron using electron energy loss spectroscopy. *J. Mater. Sci.* **27**, 2731–2733 (1992).

81. A. Ohtomo, J. L. G. . H. Y. H., D. A. Muller. Artificial charge-modulationin atomic-scale perovskite titanate superlattices. *Nature* **419**, 378–380 (2002).

82. Klie, R. F. *et al.* Direct measurement of the low-temperature spin-state transition in LaCoO3. *Physical Review Letters* **99**, 1–4 (2007).

83. Geim, A. K. & Novoselov, K. S. The rise of graphene. *Nat Mater* **6**, 183–191 (2007).

84. Schwierz, F. Graphene transistors. *Nat Nano* **5**, 487–496 (2010).

85. Bolotin, K. I. *et al.* Ultrahigh electron mobility in suspended graphene. *Solid State Communications* **146**, 351–355 (2008).

86. Radisavljevic, B., Radenovic, A., Brivio, J., Giacometti, V. & Kis, A. Single-layer MoS_2 transistors. *Nature Nanotechnology* **6**, 147–150 (2011).

87. Balandin, A. A. *et al.* Superior Thermal Conductivity of Single-Layer Graphene. *Nano Letters* **8**, 902–907 (2008).

88. Yan, Z., Liu, G., Khan, J. M. & Balandin, A. A. Graphene quilts for thermal management of high-power GaN transistors. *Nature Communications* **3**, 827 (2012).

89. Han, W., Kawakami, R. K., Gmitra, M. & Fabian, J. Graphene spintronics. *Nat Nano* **9**, 794–807 (2014).

90. Yu, W. J. *et al.* Unusually efficient photocurrent extraction in monolayer van der Waals heterostructure by tunnelling through discretized barriers. *Nature Communications* **7**, 13278 (2016).

91. Koppens, F. H. L. *et al.* Photodetectors based on graphene, other two-dimensional materials and hybrid systems. *Nature Publishing Group* **9** (2014).

92. Li, Y. *et al.* An oxygen reduction electrocatalyst based on carbon nanotubegraphene complexes. *Nature Nanotechnology* **7**, 394–400 (2012).

93. Murali, R., Brenner, K., Yang, Y., Beck, T. & Meindl, J. D. Resistivity of Graphene Nanoribbon Interconnects. *IEEE Electron Device Letters* **30**, 611–613 (2009).

94. Britnell, L. *et al.* Field-Effect Tunneling Transistor Based on Vertical Graphene Heterostructures. *Science* **335**, 947–950 (2012).

95. Wang, Q. H., Kalantar-Zadeh, K., Kis, A., Coleman, J. N. & Strano, M. S. Electronics and optoelectronics of two-dimensional transition metal dichalcogenides. *Nature nanotechnology* **7**, 699–712 (2012).

96. Lembke, D., Bertolazzi, S. & Kis, A. Single-Layer MoS_2 Electronics. *Accounts of Chemical Research* **48**, 100–110 (2015).

97. Yasaei, P. *et al.* Bimodal Phonon Scattering in Graphene Grain Boundaries. *Nano Letters* **15**, 4532–4540 (2015).

98. Watanabe, H. Experimental Evidence for the Collective Nature of the Characteristic Energy Loss of Electrons in SolidsStudies on the Dispersion Relation of Plasma Frequency. *Journal of the Physical Society of Japan* **11**, 112–119 (1956).

99. Meyer, G. Über die Abhängigkeit der charakteristischen Energieverluste von Temperatur und Streuwinkel. *Zeitschrift für Physik* **148**, 61–71 (1957).

100. Abe, H., Terauchi, M. & Tanaka, M. Temperature Dependence of the Volume-plasmon Energy in Silver. *Journal of Electron Microscopy* **44**, 45–48 (1995).

101. Abe, H., Terauchi, M., Kuzuo, R. & Tanaka, M. Temperature Dependence of the Volume-Plasmon Energy in Aluminum. *Journal of Electron Microscopy* **41**, 465–468 (1992).

102. Mitome, M., Yamazaki, Y., Takagi, H. & Nakagiri, T. Size dependence of plasmon energy in Si clusters. *Journal of Applied Physics* **72**, 812–814 (1992).

103. Wang, Y. W., Kim, J. S., Kim, G. H. & Kim, K. S. Quantum size effects in the volume plasmon excitation of bismuth nanoparticles investigated by electron energy loss spectroscopy. *Applied Physics Letters* **88**, 8–11 (2006).

104. Eberlein, T. *et al.* Plasmon spectroscopy of free-standing graphene films. *Phys. Rev. B* **77**, 233406 (2008).

105. Mecklenburg, M. *et al.* Nanoscale temperature mapping in operating microelectronic devices. *Science* **347**, 629–633 (2015).

106. Hernandez, Y. *et al.* High-yield production of graphene by liquid-phase exfoliation of graphite. *Nature Nanotechnology* **3**, 563–568 (2008).

107. Zhou, W. *et al.* Atomically localized plasmon enhancement in monolayer graphene. *Nature Nanotechnology* **7**, 161–165 (2012).

108. Louie, S. G., Chelikowsky, J. R. & Cohen, M. L. Local-Field Effects in the Optical Spectrum of Silicon. *Physical Review Letters* **34**, 155–158 (1975).

109. Late, D. J., Shirodkar, S. N., Waghmare, U. V., Dravid, V. P. & Rao, C. N. R. Thermal expansion, anharmonicity and temperature-dependent Raman spectra of single- and few-layer $MoSe_2$ and WSe_2. *ChemPhysChem* **15**, 1592–1598 (2014).

110. Ding, Y. & Xiao, B. Thermal expansion tensors, Grüneisen parameters and phonon velocities of bulk MT_2 (M = W and Mo; T = S and Se) from first principles calculations. *RSC Adv.* **5**, 18391–18400 (2015).

111. Murray, R. & Evans, B. The thermal expansion of 2h-mos2 and 2h-wse2 between 10 and 320 k. *Journal of Applied Crystallography* **12**, 312–315 (1979).

112. El-Mahalawy, S. H. & Evans, B. L. The thermal expansion of 2H-MoS_2, 2H-$MoSe_2$ and 2H-WSe_2 between 20 and 800 degC. *Journal of Applied Crystallography* **9**, 403–406 (1976).

113. Brixner, L. H. X-ray Study and Thermoelectric Properties of the $W_xTa_{1-x}Se_2$ System. *Journal of The Electrochemical Society* **110**, 289 (1963).

114. Matthaus, A. *et al.* Highly textured films of layered metal disulfide 2h ws2 : Preparation and optoelectronic properties. *Journal of The Electrochemical Society* **144**, 1013–1019 (1997).

115. Mounet, N. & Marzari, N. First-principles determination of the structural, vibrational and thermodynamic properties of diamond, graphite, and derivatives. *Physical Review B - Condensed Matter and Materials Physics* **71**, 1–14 (2005).

116. Bailey, A. C. & Yates, B. Anisotropic Thermal Expansion of Pyrolytic Graphite at Low Temperatures. *Journal of Applied Physics* **41**, 5088–5091 (1970).

117. Egerton, R. *An Introduction to EELS*, 1–28 (Springer US, Boston, MA, 2011).

118. Franklin, A. D. *et al.* Sub-10 nm Carbon Nanotube Transistor. *Nano Letters* **12**, 758–762 (2012).

119. Mavrokefalos, A., Nguyen, N. T., Pettes, M. T., Johnson, D. C. & Shi, L. In-plane thermal conductivity of disordered layered WSe_2 and $(W)_x(WSe_2)_y$ superlattice films. *Applied Physics Letters* **91**, 3–5 (2007).

120. Van De Walle, A. *et al.* Efficient stochastic generation of special quasirandom structures. *Calphad: Computer Coupling of Phase Diagrams and Thermochemistry* **42**, 13–18 (2013).

Xuan Hu

Department of Physics
University of Illinois at Chicago
xhu26@uic.edu
(312) 961-8389

EDUCATION

University of Illinois at Chicago (UIC), Chicago, IL. *Sep 2012 – Dec 2018*

Ph.D. in Condense Matter Physics

Thesis: Atomic-resolution Thermal Properties Study using STEM/EELS and First-Principles Calculations

Advisor: Professor Robert F. Klie and Professor Serdar Öğüt.

Wuhan University, China. *Sep 2006 – Jun 2012*

M.S. in Computational Physics & B.S. in Physics

RESEARCH EXPERIENCE

Research Assistant, Nanoscale Physics Group, UIC Spring 2014 - present

Area of research: Materials Science/ Electron Microscopy/ Computational Physics

My PhD main project is a comprehensive study of the thermal properties of materials using transmission electron microscopy (TEM) techniques and first-principles calculations. Specifically, my study focuses on the indirect and direct nanoscale thermal characterizations to explain the origin of macroscale thermal phenomena and explore the thermal response of lattice from the view of atoms and electrons. The techniques include aberration-corrected scanning transmission electron microscopy (STEM) imaging, electron energy loss spectroscopy (EELS) and first-principles calculations. Based on these techniques, a new nanoscale thermometry has been developed to explore the thermal expansion of 2D materials.

Master Thesis Project, Wuhan University Sep. 2010- Jun. 2012

Area of research: Computational Physics

Master thesis project was about exploring the fundamental doping process of N dopants into TiO_2 anatase using materials modeling. The density functional theory (DFT) and nudged elastic band (NEB) method have been utilized to find the local structures of N dopants and find the minimum energy path of diffusion into different surfaces.

TEACHING EXPERIENCE

- Led several groups of 20-30 students for physical experiments and maintained laboratory safety. (Fall 2012 – Spring 2016)
- Taught complex physics topics to non-professionals and received a high praise of making physics easier for them.

TRAINING

- 2015 Winter School on High Resolution Electron Microscopy and Post School Course on Aberration corrected Electron Microscopy, Leroy Eyring Center for Solid State Sciences, Arizona State University, Tempe, AZ (2015).
- Operational and safety training on JEOL JEM-ARM 200CF and JEOL 3010, Research Resource Center at UIC, Chicago, IL (Jun – Sep 2014).

AWARDS AND HONOURS

- Recipient of **Best Student Presentation** award in Material Research Society Spring Meeting. (2018)
- Recipient of **Paul M. Raccah Award** by Physics Department of University of Illinois at Chicago for outstanding doctoral studies. (2012)
- Recipient of Graduate Student Scholarship by Physics Department of Wuhan University for outstanding performance in the Graduate Student Entry Exam. (2010)

SKILL

Transmission Electron Microscopy:

- Instruments: JEOL JEM-ARM 200CF, JEOL 3010.
- Imaging: high (low)-angle annular dark field (HAADF, LAADF), annular bright field (ABF).

- Spectroscopies: EELS low-loss and core-loss with Gatan Enfina 1000 and Gatan Quantum GIF, atomic column-resolved EDS with Oxford SDD X-Max 100TLE.
- TEM Sample preparation: Conventional cross-sectional preparation techniques, FEI nano-mill, ion-mill, liquid-exfoliation preparation, 2D materials transfer, 2D liquid cells techniques.

Simulations and Data Analysis:

- Simulations: Vienna Ab-initio Simulation Package (VASP) for structure relaxation, electronic property prediction, and EELS simulation; μSTEM for STEM imaging simulation.
- Programming: Python (hyperspy, pycroscopy, scikit-learn, pandas), DigitalMicrograph script, Matlab, R, Linux shell script, Microsoft Excel, LaTeX.
- Statistical Methods: Regression Models, Hypothesis Testing, Model Selection, Principal Component Analysis and Dimensionality Reduction.

PUBLICATION

1. X. Hu, P. Yasaei, J. Jokisaari, S. Öğüt, A. Salehi-Khojin, and R. F. Klie, "Mapping thermal expansion coefficients in free-standing 2D materials at the nanometer scale", *Phys. Rev. Lett.* 120, 055902 (2018).
2. J. R. Jokisaari, J. A. Hachtel, X. Hu, A. Mukherjee, C. Wang, A. Konecna, T. C. Lovejoy, N. Dellby, J. Aizpurua, O. L. Krivanek, J. C. Idrobo, and R. F. Klie, "Vibrational spectroscopy of water with high spatial resolution", *Adv. Mater.*, 1802702 (2018)..
3. M. Asadi, B. Sayahpour, P. Abbasi, A. T. Ngo, K. Karis, J. R. Jokisaari, C. Liu, B. Narayanan, M. Gerard, P. Yasaei, X. Hu, A. Mukherjee, K. C. Lau, R. S. Assary, F. Khalili, R. F. Klie, L. A. Curtiss & A. Salehi, "A lithium-oxygen battery with a long cycle life in an air-like atmosphere", *Nature* 555, 502-506 (2018).
4. A. R. Ribeiro, A. Mukherjee, X. Hu, S. Shafien, R. Ghodsi, K. He, S. Gemini-Piperni, C. Wang, R. F. Klie, T. Shokuhfar, R. Shahbazian, R. Borojevic, L. A. Rochabh and J. M. Granjeiroabi, "Bio-camouflage of anatase nanoparticles explored by in situ high-resolution electron microscopy", *Nanoscale* 9, 10684 (2017).
5. X. Hu, P. J. Phillips, D. Mazumdar, J. C. Idrobo, S. Kolesnik, A. Gupta, S. Ogut, and R. F. Klie, "Atomic and electronic structure of Ti substitution in $Ca_3Co_4O_9$", *J. Appl. Phys.* 120, 205105 (2016).

6. X. Hu, R. Tu, J. Wei, C. Pan, J. Guo, W. Xiao, "Nitrogen atom diffusion into TiO_2 anatase bulk via surfaces", *Comput. Mater. Sci.* 82, 107-113 (2014).

CONFERENCE PRESENTATIONS

1. X. Hu, B. Sayahpour, S. Öğüt, A. Salehi-Khojin, R. F. Klie, "Tailoring Thermal Expansion Coefficient of Transition Metal Dichalcogenides via Alloy Engineering", *Material Research Society Spring Meeting,* Phoenix, AZ, 2018. (Oral Presentation)
2. X. Hu, B. Sayahpour, S. Öğüt, A. Salehi-Khojin, R. F. Klie, "Tailoring Thermal Expansion Coefficient of Transition Metal Dichalcogenides via Alloy Engineering", *American Physical Society March Meeting*, Los Angeles, CA, 2017. (Oral Presentation)
3. X. Hu, P. Yasaei, J. R. Jokissari, S. Öğüt, A. Salehi-Khojin, R. F. Klie, "Nanoscale Thermometry for 2D Materials", *Microscopy and Microanalysis*, St. Louis, MO, 2017. (Oral Presentation)
4. X. Hu, P. Yasaei, J. R. Jokissari, S. Öğüt, A. Salehi-Khojin, R. F. Klie, "Nanoscale Thermometer for Different 2D Materials", *Material Research Society Spring Meeting,* Phoenix, AZ, 2017. (Poster)
5. X. Hu, P. Yasaei, J. R. Jokissari, S. Öğüt, A. Salehi-Khojin, R. F. Klie, "Nanoscale Thermal Mapping in Two-Dimensional Materials using Electron Energy Loss Spectroscopy (EELS)", *American Physical Society March Meeting*, New Orleans, LA, 2017. (Oral Presentation)
6. X. Hu, P. Phillips, R. F. Klie, "Atomic-resolution EELS Study of Polarization of $BaTiO_3$ in the Interface with Metallic Manganite", *Microscopy and Microanalysis*, Columbus, OH, 2016. (Poster)
7. X. Hu, P. Phillips, R. F. Klie, "Atomic-resolution EELS Study of Titanium Dopant Effects of $Ca_3Co_4O_9$ Thin Film", *Microscopy and Microanalysis*, Portland, OR, 2015. (Poster)